DISSIMILATORY IRON REDUCTION: INSIGHTS FROM THE INTERACTION BETWEEN *SHEWANELLA ONEIDENSIS* MR-1 AND FERRIC IRON (OXY)(HYDR)OXIDE MINERAL SURFACES

A Dissertation
Presented to
The Academic Faculty

by

Mengni Zhang

In Partial Fulfillment
of the Requirements for the Degree
Doctor of Philosophy

School of Earth and Atmospheric Sciences
Georgia Institute of Technology
December 2010

DISSIMILATORY IRON REDUCTION: INSIGHTS FROM THE INTERACTION BETWEEN *SHEWANELLA ONEIDENSIS* MR-1 AND FERRIC IRON (OXY)(HYDR)OXIDE MINERAL SURFACES

Approved by:

Dr. Andrew G. Stack, Advisor
Chemical Science Division
Oak Ridge National Laboratory

Dr. Alexander Shapiro
School of Industrial and Systems Engineering
Georgia Institute of Technology

Dr. Ellery D. Ingall
School of Earth and Atmospheric Sciences
Georgia Institute of Technology

Dr. Frank E. Loeffler
Biosciences Division
Oak Ridge National Laboratory
Department of Civil & Environmental Engineering
University of Tennessee

Dr. Thomas J. DiChristina
School of Biology
Georgia Institute of Technology

Date Approved: 11/03/2010

To all the people who support and contribute to Science

ACKNOWLEDGEMENTS

I wish to express my appreciation to the following people who supervise and support me on my research: my advisor Dr. Andrew G. Stack, Dr. Thomas J. DiChristina, Dr. Alexander Shapiro, Ms. Meg C. Grantham, Dr. Jason R. Dale, Dr. Brian R. Ginn, Dr. Justin L. Burns, Dr. Xuefeng Wang, and Dr. Angus Wilkinson. I also appreciate all my committee members - Dr. Andrew G. Stack, Dr. Ellery D. Ingall, Dr. Thomas J. DiChristina, Dr. Alexander Shapiro, and Dr. Frank E. Loeffler. I also thank the Institute for Bioengineering and Bioscience (IBB) at Georgia Institute of Technology which allowed me to use their confocal microscope with the help of Mr. Johnafel Crowe. Finally, I thank my parents, officemates, and friends who always encourage me and support me. This work was funded by grants to Stack and DiChristina by the U.S. National Science Foundation and Department of Energy.

TABLE OF CONTENTS

LIST OF TABLES

LIST OF FIGURES

LIST OF SYMBOLS AND ABBREVIATIONS

AAC	Acoustic alternating current
AFM	Atomic force microscopy
AH_2DS	9,10-anthrahydroquinone-2,6-disulfonate
AQDS	2,6-anthraquinone disulfonate
ATP	Adenosine triphosphate
CLSM	Confocal laser scanning microscopy
DIR	Dissimilatory iron reduction
DIRB	Dissimilatory iron reducing bacteria
DIRM	Dissimilatory iron reducing microorganisms
EPS	Extracellular polycarbonate substrates
Fe(II)	Ferrous iron
Fe(III)	Ferric iron
FeS	Iron-sulfur proteins
Fp	Flavoproteins
IM	Inner membrane
NTA	Nitrilotriacetic acid
OM	Outer membrane
PMF	Proton motive force

SUMMARY

Dissimilatory iron reduction (DIR) is significant to the biogeochemical cycling of iron, carbon and other elements, and may be applied to bioremediation of organic pollutants, toxic metals, and radionuclides; however, the mechanism(s) of DIR and factors controlling its kinetics are still unclear. To provide insights into these questions, the interaction between a common dissimilatory iron reducing bacterium (DIRB)was studied, *Shewanella oneidensis* MR-1, and ferric iron (Fe(III)) (oxy)(hydr)oxide mineral surfaces. Firstly, atomic force microscopy was used to study how *S. oneidensis* MR-1 dissolved Fe(III) (oxy)(hydr)oxides and compared it to two other cases where Fe(III) (oxy)(hydr)oxides were either dissolved by a chemical reductant or by a mutant with an electron shuttling compound. Without the electron shuttling compound, the mutant is unable to respire on Fe(III) (oxy)(hydr)oxides, but with the electron shuttling compound, it can. It was found that the cells of *S. oneidensis* MR-1 formed microcolonies on mineral surfaces and dissolved the minerals in a non-uniform way which was consistent with the shape of microcolonies, whereas Fe(III) (oxy)(hydr)oxides were uniformly dissolved in both of the other cases. Secondly, confocal microscopy was used to study the adhesion behavior of *S. oneidensis* MR-1 cells on Fe(III) (oxy)(hydr)oxide surfaces across a broad range of bulk cell densities. While the cells were evenly distributed under low bulk cell densities, microcolonies were observed at high bulk cell densities. This adhesion behavior was modeled by a new, two-step adhesion isotherm which fit better than a simple Langmuir or Freundlich isotherm. The results of these studies suggest that DIR is in-part transport limited and the surface cell density may control DIR.

CHAPTER 1

INTRODUCTION TO DISSIMILATORY IRON REDUCTION

This dissertation is composed of 5 chapters. Chapter 1 introduces dissimilatory iron reduction (DIR) and has 9 sections. Sections 1.1 to 1.4 consist of the following aspects: definition and origin of DIR, allocation of DIR in subsurface environments, iron minerals, and dissimilatory iron reducing microorganisms (DIRM). Sections 1.5 to 1.6 illustrate the geochemical role and environmental effects of DIR. In sections 1.7 and 1.8, studies on mechanism(s) and kinetics of DIR were summarized. Finally, section 1.9 describes what has been done in this research to elucidate the mechanism(s) and kinetics of DIR. Chapter 2 introduces the major techniques utilized in this research. Chapter 3 and 4 are based on our published articles addressing the interaction between *Shewanella oneidensis* MR-1 and Fe(III) (oxy)(hydr)oxides. Chapter 3 focuses on the dissolution morphology of Fe(III) (oxy)(hydr)oxides exposed to *S. oneidensis* MR-1, and chapter 4 focuses on the adhesion behavior of *S. oneidensis* MR-1 on Fe(III) (oxy)(hydr)oxides. Chapter 5 is a summary of the insights into DIR provided by this research.

1.1 Definition and Origin of Dissimilatory Iron Reduction

Dissimilatory iron reduction (DIR) is defined as the process that microorganisms use ferric iron (Fe(III)) as an external electron acceptor to oxidize organic matter or hydrogen for metabolic activities. Microorganisms which are capable of DIR are referred to as dissimilatory iron reducing microorganisms (DIRM). The isolation of DIRM dated back to the early 1980s, when Westlake and colleagues isolated *Pseudomonas*

ferrireductans from oilfield samples (Obuekwe et al. 1981); one of the strains, *Pseudomonas sp.* 200, was extensively studied (Arnold et al. 1988). *P. ferrireductans* was subsequently designated *Alteromonas putrfaciens*, and now *Shewanella putrefaciens* (Nealson and Saffarini 1994). In 1988, Myers and Nealson (1988) isolated *Alteromonas putrfaciens* MR-1 (subsequently designated *Shewanella oneidensis* MR-1) from the sediments of Lake Oneida, New York. In the same year, Lovley and Phillips (1988) isolated GS-15 (subsequently designated *Geobacter metallireducens*) from the sediments of the Potomac River, Maryland. These studies not only demonstrated the existence of DIRM, but also initiated a new research field on DIR. The amount of research on DIR has increased extensively since the 1980s.

1.2 Dissimilatory Iron Reduction in Subsurface Environments

Dissimilatory iron reduction is mainly located in the subsurface environments such as soils and sediments where a couple of electron acceptors are available for microorganisms besides iron. Previous research suggests that the free energy generated by reducing different electron acceptors may determine the sequence by which microorganisms prefer to select in the subsurface environment (Reeburgh 1983). Table 1 shows the theoretical calculation of energy yield from different electron acceptors, from high to low, assuming glucose is the electron donor (Nealson and Saffarini 1994). Based on the calculation, microorganisms select electron acceptors following a sequence of oxygen, nitrate, Mn(IV), Fe(III), sulfate and carbon dioxide. This trend has been observed in natural subsurface environments, such as the sediments of freshwater (Lake Michigan) and marine (Black Sea), the profile of which are shown in Figure 1.

Table 1: Comparison of different electron acceptors (Nealson and Saffarini 1994).

Electron acceptor Equation for generalized oxidation of organic carbon (glucose)	Free Energy (kJ/mol glucose)
Oxygen $C + 138\ O_2 \rightarrow 106\ CO_2 + 16\ HNO_3 + H_3PO_4 + 122\ H_2O$	-3190
Nitrate $C + 94.4\ HNO_3 \rightarrow 106\ CO_2 + 55.2\ N2 + H_3PO_4 + 177.2\ H_2O$	-3030
Manganese $C + 236\ MnO_2 + 472\ H^+ \rightarrow 236\ Mn^{2+} + 106\ CO_2 + 8\ N_2 + H_3PO_4 + 366\ H_2O$	-2920
Iron (hematite) $C + 212\ Fe_2O_3 + 848\ H^+ \rightarrow 424\ Fe^{2+} + 106\ CO_2 + 16\ NH_3 + H_3PO_4 + 530\ H_2O$	-1410
Iron (goethite) Sulfate $C + 424\ FeOOH + 848\ H^+ \rightarrow 424\ Fe^{2+} + 106\ CO_2 + 16\ NH_3 + H_3PO_4 + 742\ H_2O$	-1330
Sulfate $C + 53\ SO_4^{2-} \rightarrow 106\ CO_2 + 16\ NH_3 + 53\ S^{2-} + H_3PO_4 + 106\ H_2O$	-380
CO_2 $C \rightarrow 53\ CO_2 + 53\ CH_4 + 16\ NH_3 + H_3PO_4$	-350

Both marine and freshwater sediments start with oxygen dominating the top layer. Oxygen diffuses from the water above the sediments, but then is quickly depleted due to organic matter degradation. Below the oxygen depletion zone, nitrate concentrations usually increase, caused by nitrification of ammonia which diffuses upwards from below. Below the nitrate reduction zone are the metal reduction zones, where organic matter is degraded by manganese and iron (oxy)(hydr)oxides, which accumulate from oxidation of soluble Mn(II) and Fe(II) that diffuse upwards. Manganese oxides usually overlay iron oxides because Fe(II) is more rapidly oxidized in the presence of low levels of oxygen.

The difference between the marine and freshwater sediments lies in the layer(s) below the metal reduction zones. Marine sediments contain an abundance of sulfate; therefore sulfate reduction dominates beneath the zones of metal reduction. Freshwater sediments, on the other hand, do not contain much sulfate; therefore methanogenesis dominates beneath the metal reduction layer.

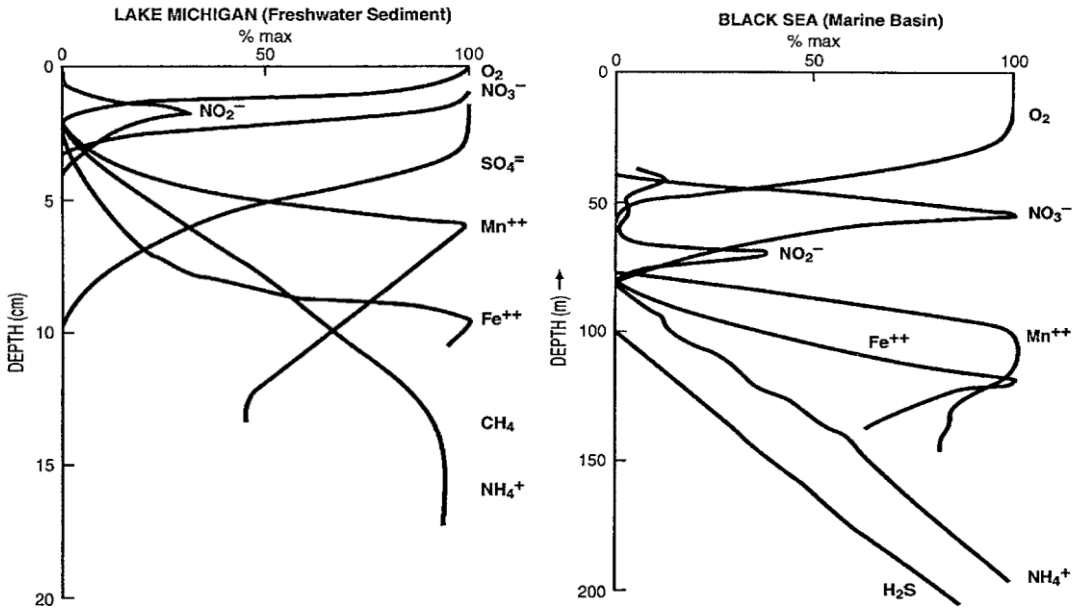

Figure 1: Vertical profiles in typical freshwater (Lake Michigan) and marine (Black Sea) sediments (Nealson and Berelson 2003).

1.3 Iron Minerals

1.3.1 Iron Element and Minerals

Dissimilatory iron reduction is ubiquitous in subsurface environments, partially because iron is the forth abundant element in the Earth's crust. Iron is commonly found in two oxidation states: ferrous iron (Fe(II)) and ferric iron (Fe(III)). The pE-pH diagram shown in Figure 2 suggests that changes in the oxidation state of iron are often coupled with Fe(III) precipitation, and the most commonly found Fe(III) precipitates in subsurface environments are Fe(III) (oxy)(hydr)oxides, such as hematite (α-Fe_2O_3), goethite (α-FeOOH) which are highly crystalline and ferrihydrite which is amorphous. The crystallinity of Fe(III) (oxy)(hydr)oxides can greatly influence the rate and extent of DIR; generally, DIRM reduce amorphous Fe(III) (oxy)(hydr)oxides more rapidly and thoroughly than well crystalline ones (Roden and Zachara 1996).

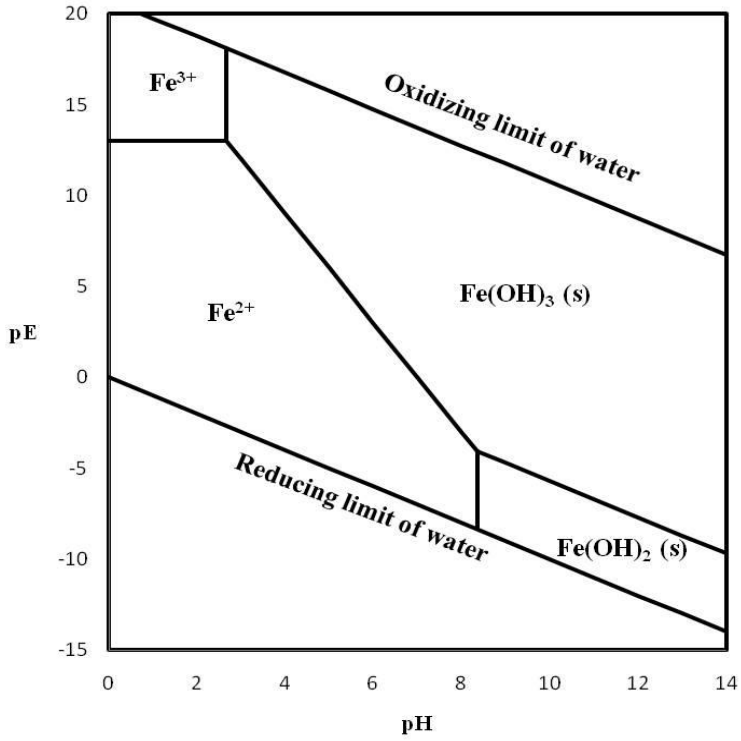

Figure 2: The pE-pH diagram for Fe-H_2O system. Concentration of soluble Fe species is 10^{-5} M (25^{o}C).

1.3.2 The Geochemical Cycling of Iron

The Earth's crust contains iron mainly in the form of Fe(II) silicates. In the presence of oxygen and water, these silicates are oxidized and hydrolyzed to Fe(III) (oxy)(hydr)oxides (Cornell and Schwertmann 1996). These minerals usually have very low solubility, and thus precipitate and settle in the suboxic zone. Fe(III) (oxy)(hydr)oxides are relatively stable in the suboxic zone; however, they may be mobilized by DIRM. Fe(II) released from DIR can diffuse to the oxic zone where oxidation and hydrolyzation of Fe(II) take place to form Fe(III) (oxy)(hydr)oxides. These solids may be transported to the suboxic zone and complete an iron cycle (Nealson and Saffarini 1994). Figure 3 shows the cycling of iron in freshwater and marine sediments.

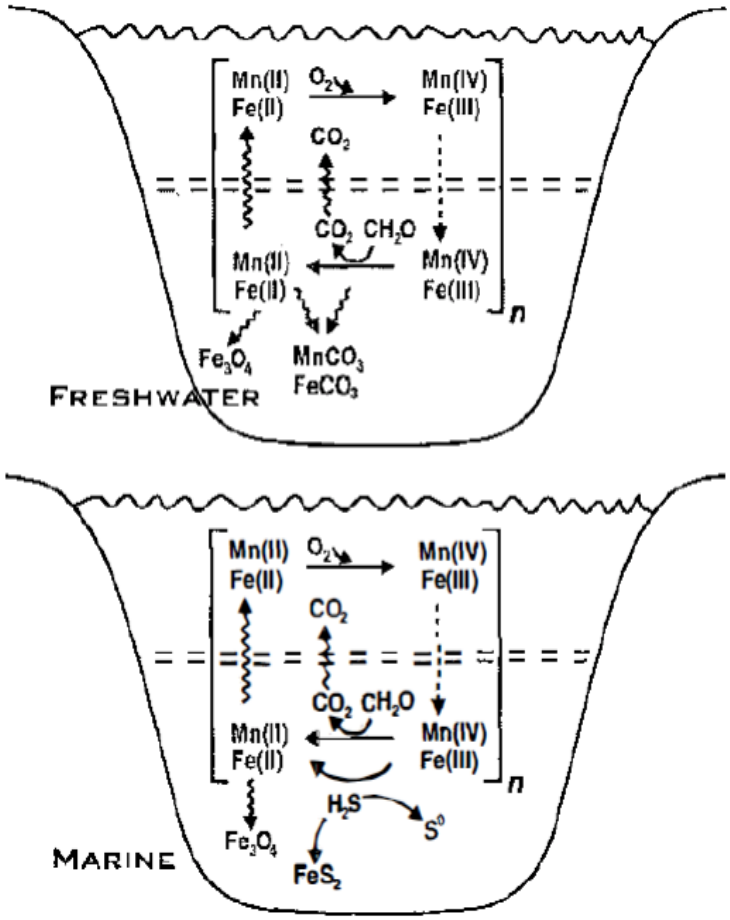

Figure 3: Iron cycle in freshwater and marine sediments (Nealson and Saffarini 1994).

In freshwater sediments, iron is mainly removed from the cycle by forming insoluble carbonates and magnetite; in marine sediments, iron is mainly removed by pyrite formation.

1.4 Dissimilatory Iron Reducing Microorganisms (DIRM)

DIRM were isolated from a variety of natural environments, including freshwater sediments (Lovley and Philips 1988), estuary sediments (Caccavo et al. 1992), marine sediments (Roden and Lovley 1993) and soils (Caccavo et al. 1994). Among DIRM, dissimilatory iron reducing bacteria (DIRB) have been the focus of intense studies.

1.4.1 Phylogenetic Diversity

DIRB are widely distributed phylogenetically, with the majority belonging to different subdivisions of the phylum *Proteobacteria* (see details on subdivisions of *Proteobacteria* in Appendix C) (Nealson and Saffarini 1994; Fredrickson and Gorby 1996; Lonergan et al. 1996). Figure 4 shows a phylogenetic tree of some DIRB (bold lines) inferred from 16S rRNA sequence. Most DIRB species in Figure 4 are located in the delta subdivision of *Proteobacteria*, such as genera *Geobacter*, *Desulfuromonas*, and *Anaeromyxobacter*. Example species include *Geobacter metallireducens* (Lovley and Philips 1988), *Desulfuromonas acetoxidens* (Roden and Lovley 1993), and *Anaeromyxobacter dehalogenans* (He and Sanford 2003). In addition, some DIRB species are located in the gamma subdivision of *Proteobacteria* such as the genus *Shewanella* (Lonergan et al. 1996). Furthermore, some DIRB species do not reside in *Proteobacteria*, such as the species *Geothrix fermentans* which belongs to the phylum *Acidobacterium* (Coates et al. 1999).

Figure 4 suggests that DIRB are diversely evolved, which significantly increases the difficulty to study dissimilatory iron reduction. For example, different species may prefer different pathways to respire on solid Fe(III) (oxy)(hydr)oxides, and when using the same pathway, different species has different genes to conduct the same function. All of these possibilities make the comparison of experimental results among different DIRB species less informative.

1.4.2 *Shewanella oneidensis* MR-1, Wild-type and Mutants

Shewanella oneidensis MR-1 was first isolated from the sediments of Lake Oneida, New York, in 1988 (Myers and Nealson 1988), when it was first identified as

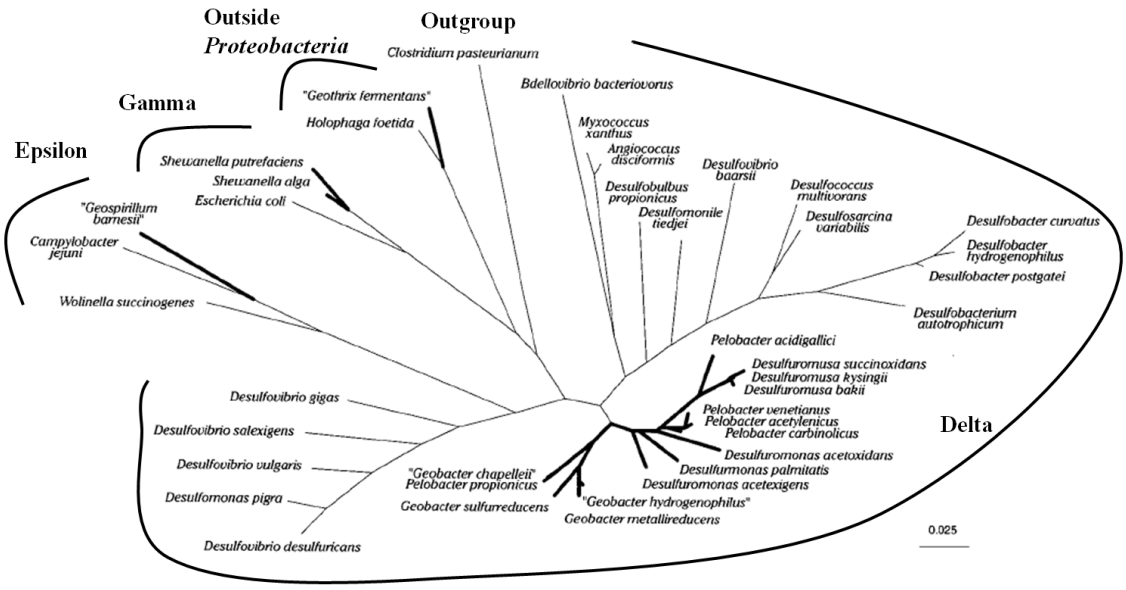

Figure 4: Phylogenetic distribution of DIRB species (bold lines) inferred from 16S rRNA sequence till 1996 (Lonergan et al. 1996). In this figure, Gamma, Delta, and Epsilon stand for the subdivisions of *Proteobacteria*. The sequence of *Clostridium pasteurianum* is used as the outgroup.

Alteromonas putrfaciens MR-1, and subsequently *Shewanella putrfaciens* MR-1 (Nealson and Saffarini 1994). Afterwards, Venkateswaran et al. (1999) suggested that this strain was distinct and deserved the status of species, naming it *Shewanella oneidensis* MR-1 after the lake where this bacterium was isolated. *S. oneidensis* MR-1 is gram-negative and facultative, capable of coupling the oxidation of H_2 or organic substrates (acetate, lactate, succinate, fumarate, etc.) to the reduction of a wide range of electron acceptors such as oxygen, nitrate, transition metal oxides (Fe, Mn, U) and elemental sulfur. The cells of *S. oneidensis* MR-1 are rod-shaped, 2-3 μm in length and 0.5-0.6 μm in diameter, with an optimal growth temperature of 30^{o}C (Venkateswaran et al. 1999).

Genetic mutation of *S. oneidensis* MR-1 can lead to several strains which have

impaired ability to reduce Fe(III) (oxy)(hydr)oxides compared to the wild-type. Examples are Δ*gspD* and Δ*gspE* mutants which have mutation on the genes *gspD* and *gspE,* respectively (DiChristina et al. 2002; Shi et al. 2008). The genes *gspD* and *gspE* encode the corresponding proteins GspD and GspE which are key components of a type II secretion system (T2SS). T2SS is involved in DIR by translocating proteins MtrC and OmcA from periplasm to the extracellular side of the outer membrane (OM). MtrC and OmcA have been hypothesized to function as the terminal reductases of Fe(III) (oxy)(hydr)oxides. Therefore, the mutation of genes *gspD* or *gspE* disables the cells in translocation of terminal Fe(III) reductases across OM, resulting in the Fe(III)-reduction deficient mutants.

1.5 Geochemical Role of Dissimilatory Iron Reduction

Dissimilatory iron reduction is important to a variety of globally significant natural processes, such as the biogeochemical cycling of carbon, iron, phosphate, and trace metals (Lovley 1991; Nealson and Saffarini 1994).

For carbon, the importance of DIR to organic matter degradation in subsurface environments had been underestimated until the 1980s when a series of DIRM were isolated. DIR was found to be significant to organic matter degradation in a variety of subsurface environments, including the sediments of estuary, marine, salt marsh, and littoral lake. DIR was found to dominate organic matter degradation in some areas of the inner shelf mud near the mouth of Amazon River, instead of microbial sulfate reduction as previously thought (Aller et al. 1986). Microbial sulfate reduction is the process that microorganisms use sulfate as an electron acceptor to oxidize organic carbon for growth. Similarly, at one site along the Danish coastal sediments, DIR was found to be more

significant than microbial sulfate reduction, accounting for 47–78% of organic matter degradation in the suboxic zone, with the remainder dominated by microbial sulfate reduction (Canfield et al. 1993). DIR may also play an important role in salt marsh sediments, as an active population of DIRM was found to inhabit the salt marsh sediments of Sapelo Island, Georgia (Lowe et al. 2000). Finally, DIR and microbial sulfate reduction were the dominant pathways of organic matter degradation in the upper 50 cm of littoral lake sediments (Koretsky et al. 2006).

For iron, it has been suggested that DIR accounts for the majority of iron transition from Fe(III) to Fe(II) in suboxic non-sulfidogenic environments (Lovley 1991; Fredrickson and Gorby 1996). For example, in lacustrine environments where the concentration of sulfate is low, iron reduction may be primarily biologically catalyzed (Lovley et al. 1991b). For phosphate which react with Fe(II) to form vivianite, DIR may cause phosphate to settle in the suboxic zone. For some trace metals (Cu, Cd, Co, Pb, etc.) which easily form complexes with Fe(III) (oxy)(hydr)oxides, DIR may cause these metals to be released to the surrounding environment.

1.6 Environmental Effects of Dissimilatory Iron Reduction

1.6.1 Positive Effects of Dissimilatory Iron Reduction

DIRB are potentially attractive to apply in the bioremediation of environments contaminated by a variety of compounds, including organic contaminants, toxic metals, and radionuclides (Lovley 1991; Nealson and Saffarini 1994; Fredrickson and Gorby 1996; Nealson and Little 1997). DIRB can degrade hazardous chlorinated organic compounds (Petrovskis et al. 1994; Kazumi et al. 1995), aromatic compounds (Lovley et

al. 1989; Lovley and Lonergan 1990), and nitrates (Heijman et al. 1995; Klausen et al. 1995). In addition, *Shewanella oneidensis* MR-1 was found to effectively reduce chromium from the toxic and mobile form Cr(VI) to the less toxic and less mobile form Cr(III) (Viamajala, 2002). Similarly, laboratory studies showed that DIRB species *Geobacter metallireducens* and *Shewanella putrfaciens* reduced uranium from its relatively mobile oxidized state U(VI) to the immobile state U(IV), which readily precipitated as the insoluble mineral uraninite (Lovley et al. 1991a; Gorby and Lovley 1992). This process was also demonstrated at uranium waste sites (Lovley and Philips 1992; Anderson et al. 2003).

Nealson and Little (1997) proposed three advantages of applying DIRB in bioremediation: (1) Fe(III) (oxy)(hydr)oxides are solids, so their diffusion from contaminated sites will be limited; (2) the enzymatic specificity necessary for DIR diminishes the possibility of competition from other bacteria; and (3) the cycling of iron as described in section 1.3.2 may facilitate DIR

1.6.2 Negative Effects of Dissimilatory Iron Reduction

Even though DIRB have the potential for bioremediation, DIR can lead to problems such as corrosion and release of adsorbed pollutants. Semple and Westlake (1987) indicated that the DIRB species, *Alteromonas putrfaciens*, which was isolated from oil field fluids, could contribute to the corrosion of metal in oil fields. In addition, Fe(III) (oxy)(hydr)oxides are known for their ability to adsorb ions. After DIR, bounded pollutants, such as Cd, Cr, Ni, Pb, Zn, and As, may be mobilized and released to surrounding environment (Francis and Dodge 1990; Cummings et al. 1999).

1.7 Mechanisms of Dissimilatory Iron Reduction

To successfully apply DIRB in environmental remediation, it is critical to understand the mechanism of dissimilatory iron reduction. Previous research on bacterial respiration on soluble electron acceptors is not applicable because DIRB react with solid mineral surfaces. Thus, one key concern is what pathways DIRB have evolved to respire on Fe(III) (oxy)(hydr)oxides. Furthermore, since DIR is a mineral surface reaction, it is important to find out whether it is surface limited or transport limited. In a surface limited reaction, the reaction on the mineral surface is limiting the rate, whereas in a transport limited reaction, the transport of reactants for surface reaction is limiting the rate.

So far, understanding to the mechanism of DIR is incomplete. Section 1.7.1 explains the pathway of bacteria respiring on soluble electron acceptors and why this pathway does not apply to DIR. Section 1.7.2 introduces some novel strategies that DIRB may have evolved to respire on Fe(III) (oxy)(hydr)oxides.

1.7.1 Mechanism of Bacteria Respiring on Soluble Electron Acceptors

Bacteria respire on soluble electron acceptors through an inner membrane (IM)-localized electron transport system (DiChristina et al. 2005). This system mainly contains proteins which not only mediate electron transfer from donors to acceptors, but also conserve energy released during electron transport to generate ATP (Adenosine Triphosphate). The electron transport system of a common bacterium, *Escherichia coli*, using $NADH_2$ as the electron donor and oxygen as the electron acceptor, illustrates how bacteria respire on soluble electron acceptors (Figure 5). This system starts from dehydrogenase complexes, which include electron donor-specific reductases and membrane-associated proteins such as flavoproteins (Fp) and iron-sulfur proteins (FeS). Fp translocate protons across IM to the periplasm, and FeS proteins transfer electrons to

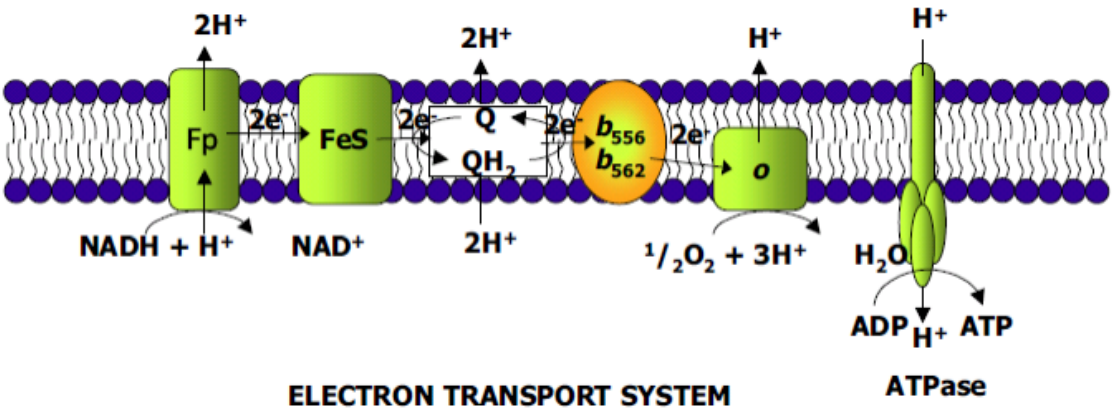

Figure 5: Inner membrane (IM)-localized electron transport system of *E. coli* using $NADH_2$ as the electron donor and O_2 as the electron acceptor (DiChristina et al. 2005). Fp is flavorproteins; FeS is iron-sulfter protein; Q is quinone pool; b_{556}, b_{562}, and *o* are different cytochromes in terminal reductase complexes.

the next component - the quinone pool. In the quinone pool,the reduction-oxidation cycling of quinones pumps protons across IM to the periplasm and translocates electrons to terminal reductase complexes. Terminal reductase complexes are composed of cytochromes such as b_{556}, b_{562}, and *o*. Cytochrome *o* catalyzes both translocation of a proton across IM to periplasm and terminal reduction of O_2 to H_2O. During this electron transport process, protons that are pumped to periplasm generate the proton motive force (PMF) which drives ATP synthesis as protons are translocated back into cytoplasm. The IM-localized electron transport system is common in gram-negative bacteria that respire on soluble electron acceptors (DiChristina et al. 2005).

DIRB cannot utilize the above pathway to respire on Fe(III) (oxy)(hydr)oxides because Fe(III) in these crystalline or amorphous solids is presumably unable to contact the IM-localized electron transport system. DIRB need to either extend their electron transport system to the outer membrane or evolve some method(s) to dissolve Fe(III) (oxy)(hydr)oxides.

1.7.2 Mechanisms of DIRB Respiring on Solid Fe(III) (Oxy)(hydr)oxides

DIRB are postulated to have evolved several novel respiratory strategies not found in other bacteria respiring on soluble electron acceptors (Gralnick and Newman 2007). Sections 1.7.2.1 to 1.7.2.4 illustrate four proposed pathways that DIRB have evolved to respire on Fe(III) (oxy)(hydr)oxides. Section 1.7.2.5 explains the potential for multiple pathways acting simultaneously.

1.7.2.1 Direct Contact Pathway

Several researchers have proposed that DIRB evolved outer membrane-localized iron reductases which link the IM-localized electron transport system to reduce Fe(III) (oxy)(hydr)oxides; this is referred to as direct contact mechanism (Beliaev and Saffarini 1998; Myers and Myers 1992, 2003; Shi et al. 2007). For some DIRB species, direct contact with Fe(III) (oxy)(hydr)oxides is required for DIR. For example, when *Pseudomonas sp.* 200 and goethite were separated by a dialysis membrane, no iron reduction was observed, which indicated cell-mineral contact was essential for DIR (Arnold et al. 1988). Similar to *Pseudomonas sp.* 200, *Geobacter metallireducens* could not reduce Fe(III) (oxy)(hydr)oxides when separated by semipermeable materials or microporous alginate beads (Nevin and Lovley 2000). Furthermore, this study used several experimental approaches to indicate that *G. metallireducens* did not release electron shuttling compounds or significantly solubilize Fe(III) during DIR, further indicating that this microorganism directly reduced Fe(III) (oxy)(hydr)oxides (Nevin and Lovley 2000).

One area of research on the direct contact mechanism focuses on elucidating the enzymology of the electron transport system of DIRB, which includes dehydrogenase

complexes, menaquinone pool, and terminal reductase complexes that extend to the outer membrane of bacterial cells. Different species of DIRB may have different proteins conducting the same function. For the genus *Shewanella*, the key proteins in the electron transport system include four c-type cytochromes: CymA, MtrA, MtrC, and OmcA. CymA is located in the menaquinone pool within the inner membrane, and transfers electrons across the inner membrane to the periplasm where MtrA is located (Myers and Myers 1997; Myers and Myers 2000). MtrA further transfers electrons to the OM proteins involved in reduction of Fe(III) (oxy)(hydr)oxides. The OM proteins have not been definitely identified; however, MtrC and OmcA are postulated to be major components of solid Fe(III) reductases (Shi et al. 2007).

1.7.2.2 Nanowires Pathway

Besides the direct contact pathway, it has been suggested that DIRB can produce pilus-like, electrically conductive appendages, referred to as nanowires, to transfer electrons extracellularly from cell surface to the surface of Fe(III) (oxy)(hydr)oxides (Reguera et al. 2005; Gorby et al. 2006). The nanowires were observed in *Geobacter sulfurrenducens* and *Shewanella oneidensis* MR-1. In the case of *G. sulfurrenducens*, Childers et al. (2002) observed a special type of pilus on *G. sulfurrenducens*, which aided this bacterium to establish contact with Fe(III) (oxy)(hydr)oxides. Based on this study, Reguera et al. (2005) created a mutant of *G. sulfurrenducens* deficient in this pilus and found the mutant could not reduce Fe(III) (oxy)(hydr)oxides but could still attach. Furthermore, Reguera et al. discovered that the pilus were highly conductive; therefore, they suggested that the pilus of *G. sulfurrenducens* serves as direct electron conduits between the cells and Fe(III) (oxy)(hydr)oxides, and referred to it as “biological

nanowires". *S. oneidensis* MR-1 was also found to produce pilus-like, electrically conductive appendages in direct response to electron-acceptor limitation (Gorby et al. 2006). In addition, mutants deficient in genes for MtrC and OmcA, and those defective in the type II secretion system produced poorly conductive nanowires, and were unable to respire on Fe(III) (oxy)(hydr)oxides. This study further supported that the nanowires pathway may serve as a strategy for efficient electron transfer.

1.7.2.3 Electron Shuttling Pathway

In addition to respiring on Fe(III) (oxy)(hydr)oxides directly, DIRB may also use indirect pathways, such as this two-step electron shuttling pathway. First, DIRB enzymatically reduce soluble electron shuttling compounds; second, the reduced electron shuttling compounds chemically reduce Fe(III) (oxy)(hydr)oxides, producing Fe(II) and the original electron shuttling compounds (Figure 6) (Lovley et al. 1996; Newman and Kolter 2000; Royer et al. 2002; Turick et al. 2002; Hernandez et al. 2004; Kappler et al. 2004; Marsili et al. 2008; von Canstein et al. 2008). In Figure 6, AQDS (2,6-anthraquinone disulfonate) is reduced to AH_2DS (9,10-anthrahydroquinone-2,6-disulfonate). In this way, AQDS transports electrons between DIRB and Fe(III) (oxy)(hydr)oxides, and acts as an election shuttle. Electron shuttles can be either exogenous (not produced by organisms) such as humic substances (Lovley et al. 1996; Royer et al. 2002; Kappler et al. 2004), or endogenous (produced by organisms) [antibiotics (Hernandez et al. 2004), melanin (Turick et al. 2002), flavins (Marsili et al. 2008; von Canstein et al. 2008), and quinones (Newman and Kolter 2000)].

Lovley et al. (1996) were the first to show humic acids could serve as either electron acceptors or electron shuttles for DIRB. Previously, humic acids were thought to

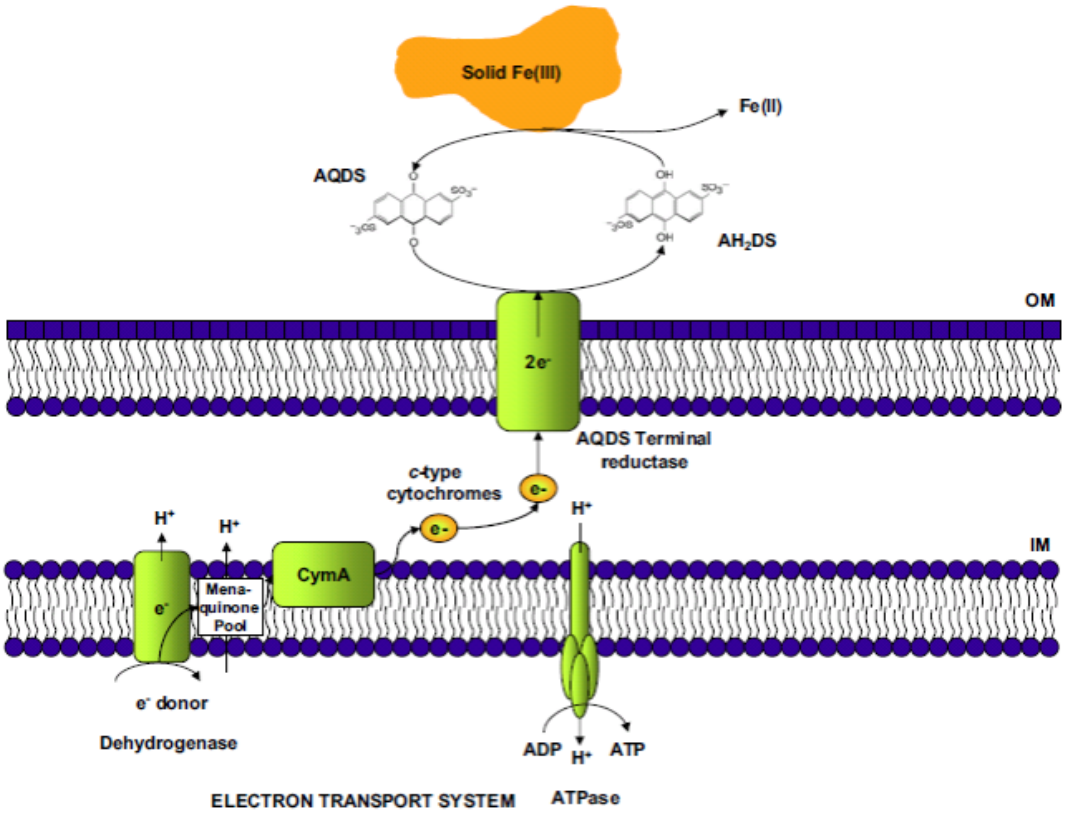

Figure 6: Electron shuttling mechanism using AQDS as electron shuttle (DiChristina et al. 2005).

stimulate DIR through chelating Fe(III); however, this research showed that humic acids served as electron shuttles to transfer electrons between DIRB and Fe(III). The quinone/hydroquinone redox couple of humic acids was suggested to be involved in this electron shuttling mechanism. In addition to this study, Kappler et al. (2004) found that humic acids served as electron shuttles for DIR in the field, and proposed this was an important pathway of electron flow in suboxic natural environment. Besides humic acids, other humic substances such as fulvic acids can also enhance DIR via means of electron shuttling (Royer et al. 2002).

Besides using exogenous electron shuttles, some DIRB species have been shown

to produce endogenous electron shuttles to facilitate DIR. For example, *Shewanella putrfaciens* strain MR-1 (now *Shewanella oneidensis* MR-1) released a quinone-related redox-active small molecule that may mediate the electron transfer between bacterial cells and Fe(III) (oxy)(hydr)oxides (Newman and Kolter 2000). In addition, *Shewanella algae* BrY secreted melanin under aerobic growth, which could function as an electron shuttle in DIR (Turick et al. 2002). Similarly, *Pseudomonas chlororaphis* PCL1391 can produce phenazine-1-carboxamide, a redox-active antibiotic, to promote DIR through electron shuttling mechanism (Hernandez et al. 2004). Finally, flavins, secreted by a range of *Shewanella* species under both aerobic and anaerobic growth, were identified as electron shuttles (von Canstein et al. 2008). Consistent with this research, another study detected cell-secreted redox-active flavins within *Shewanella* biofilms, which were involved in electron transfer from biofilms to electrodes (Marsili et al. 2008).

1.7.2.4 Organic Ligand Pathway

Another indirect pathway that may be utilized by DIRB is the organic ligand pathway, a two-step Fe(III) solubilization-reduction pathway. Fe(III) (oxy)(hydr)oxides are first dissolved via exogenous or endogenous organic ligands chelating and subsequently reduced by periplasmic Fe(III) reductases (Lovley et al. 1994, Lovley and Woodward 1996; Taillefert et al. 2007, Jones et al. 2010).

Organic ligands in sediments and soils have been shown to function as Fe(III) chelators, which ultimately affect the geochemical cycling of iron (Luther et al. 1992; Liang et al. 1993). In 1994, when studying the degradation of aromatic hydrocarbons in aquifers, Lovley et al. (1994) found that the respiration of DIRB on aromatic hydrocarbons and Fe(III) (oxy)(hydr)oxides could be stimulated to a comparable rate as

aerobic respiration by adding a synthetic Fe(III) chelator. This organic ligand, nitrilotriacetic acid (NTA) dramatically increased the bioavailability of Fe(III), thus allowing DIR to become a potential alternative to traditional aerobic respiration (i.e., oxygen addition) for the bioremediation of petroleum-contaminated aquifers. A subsequent research further studied the mechanism by which NTA stimulated DIR, and indicated that NTA solubilization of Fe(III) (oxy)(hydr)oxides was an important mechanism (Lovley and Woodward 1996). This research also demonstrated that NTA stimulated the dissimilatory reduction of a variety of Fe(III) (oxy)(hydr)oxides, including highly crystalline goethite and hematite.

Besides the exogenous organic ligands discussed above, voltammetric studies suggested that two *Shewanella* species, *Shewanella putrefaciens* 200 and *Shewanella oneidensis* MR-1, produce endogenous organic ligands in dissimilatory iron reduction. In the case of *S. putrefaciens* 200, organic complexes of Fe(III) during DIR were detected and were found to be produced at rates that correlated with the reactivity of the Fe(III) phase and bacterial cell density (Taillefert et al. 2007). These results suggested that *S. putrefaciens* 200 produces endogenous organic ligands to increase the bioavailability of Fe(III) (oxy)(hydr)oxides. In the case *S. oneidensis* MR-1, a recent study using the same technique also suggested the formation of soluble organic-Fe(III) complexes during DIR. Furthermore, four mutants with impaired ability to produce soluble organic-Fe(III) complexes during DIR compared to wild-type were generated and it was found the production rates of soluble organic-Fe(III) complexes were proportional to the rates of DIR by wild-type and four mutants. All these results indicated that the production of soluble organic-Fe(III) complexes may be a significant step in DIR by *S. oneidensis* MR-

1. The endogenous organic ligands in both cases were not characterized; however, studies suggest siderophores which are used to chelate Fe(III) during assimilatory iron reduction are not involved in DIR by *S. oneidensis* MR-1 (Fennessey et al. 2010). Mutants defective in siderophore biosynthesis system and Fe(III)-siderophore reductases retained the ability to solubilize and respire Fe(III) (oxy)(hydr)oxides at wild-type rates, therefore indicating the endogenous organic ligands produced by *S. oneidensis* MR-1 were not synthesized via the siderophore biosynthesis system and the Fe(III)-siderophore reductase is not essential for DIR.

1.7.2.5 Multiple Pathways

Even though the above four pathways are quite different, they are not exclusive with each other. Some mechanisms may occur simultaneously. For example, Nevin and Lovley (2002a) suggested that *Geothrix fermentans* released both electron shuttles and Fe(III) solubilizing compounds during DIR by designing experiments of incorporating Fe(III) oxides into microporous alginate beads which prevented direct contact between *G. fermentans* and Fe(III) oxides. The researchers identified a quinone-type molecule to serve as an electron shuttle which enabled *G. fermentans* to indirectly reduce Fe(III) within the beads. Meanwhile, they detected 250 μM dissolved Fe(III) in the filtrates which suggested that *G. fermentans* released compounds capable of chelating and solubilizing Fe(III). Nevin and Lovley (2002b) tested the same experiments with *Shewanella alga* strain BrY and achieved similar results. Recently, Peretyazhko et al. (2010) suggested that both electron shuttling mechanism and organic ligand mechanism can occur simultaneously in laboratory and natural environments. This study investigated DIR of *Shewanella oneidensis* MR-1 on 6-line ferrihydrite which was located within

porous silica (intragrain ferrihydrite) to prevent direct contact with bacterial cells. The observed indirect reduction of 6-line ferrihydrite and a detection of 200-300 μM dissolved Fe(III) led to an assumption that both electron shuttling mechanism and organic ligand mechanism may be active to varying extents in the intragrain ferrihydrite reduction and it was unable to conclusively distinguish which mechanism was more important.

1.8 Kinetics of Dissimilatory Iron Reduction

Scientists found that the kinetics of DIRB respiring on aqueous Fe(III) generally follow the Monod rate expression (derived in Appendix B) (Liu et al. 2001a); however, this model is not applicable to the kinetics of DIRB respiring on solid Fe(III) (oxy)(hydr)oxides (Liu et al. 2001b). This difference may be caused by the difficulty to define the bioavailable Fe(III) concentration in Fe(III) (oxy)(hydr)oxides, since it is affected by aggregation of Fe(III) (oxy)(hydr)oxides, and adsorption and precipitation of Fe(II) on Fe(III) (oxy)(hydr)oxides. Furthermore, the difference may imply that DIRB respiring on Fe(III) (oxy)(hydr)oxides is a more complex process than DIRB respiring on aqueous Fe(III), so that a more comprehensive kinetics model based on knowledge of the respiration mechanism(s) is needed. The mechanism(s) of DIR is likely to affect the kinetics. For example, when direct contact is required for DIR, cell adhesion on mineral surfaces may affect the rate of DIR; when biofilm forms during DIR, the kinetics may be different from the situation when no biofilm forms. Therefore, a variety of factors may need to be considered when studying the kinetics of DIR. So far, it has been found that the kinetics of DIR may be influenced by the following factors: surface site concentration of Fe(III) (oxy)(hydr)oxides; mineral solubility that correlates positively with surface area; concentration of electron donors; bacterial cell density; sorption and/or

precipitation of Fe(II) on the residual Fe(III) (oxy)(hydr)oxides and/or cell surfaces; thermodynamic limitations; and existence of exogenous electron shuttles or organic ligands which has been discussed above (Roden and Zachara 1996; Urrutia et al. 1998; Liu et al. 2001b; Roden 2003; Bonneville et al. 2004; Roden 2004; Royer et al. 2004; Roden 2006; Hyacinthe et al. 2008).

Roden and his colleagues published a series of papers where they studied factors controlling DIR and developed a model to fit this process. In 1996, Roden and Zacchara (1996) measured the initial rate of DIR over a range of synthetic Fe(III) (oxy)(hydr)oxides and found a linear correlation between the rates and the surface area of these oxides. In addition, they found the adsorption and precipitation of biogenic Fe(II) limited the extent of DIR (Roden and Zacchara 1996). Based on these observations and considering the potential aggregation of Fe(III) (oxy)(hydr)oxides, which could affect the surface area, the authors suggested that the surface site concentration of Fe(III) (oxy)(hydr)oxides was the most significant factor controlling DIR. In 2003, Roden (2003) published a similar kinetics study on DIR with a wider range of Fe(III) (oxy)(hydr)oxides and compared the kinetics between DIR and abiotic Fe(III) reduction. The author observed a linear correlation between the initial rates of DIR and the surface area of 12 types of Fe(III) (oxy)(hydr)oxides under a series of bulk cell densities, which further supported the importance of surface site concentration as a controlling factor of DIR. This research also suggested that rates of DIR reached an asymptote at bulk cell density in excess of 5×10^8 cells/mL, as shown in Figure 7. Furthermore, from the comparison between DIR and abiotic Fe(III) reduction Roden concluded that mineral crystal thermodynamic properties did not exert a significant impact on DIR as it did on abiotic

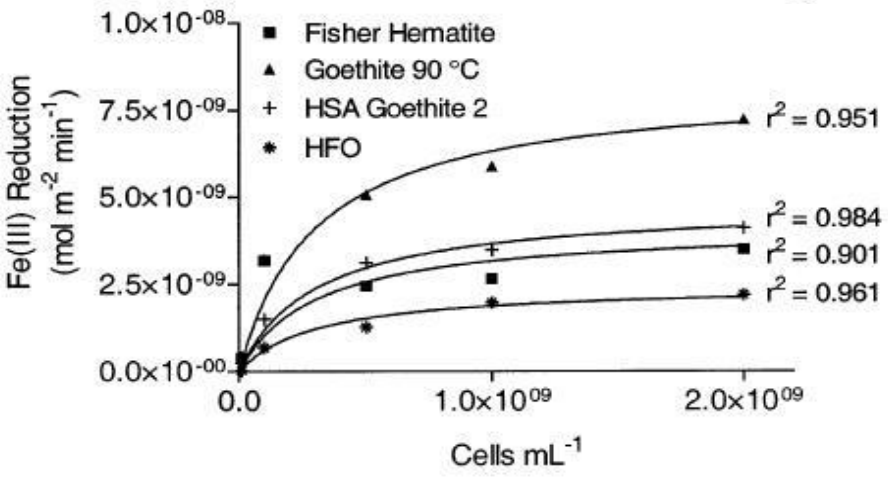

Figure 7: The relationship between surface area normalized DIR rates and DIRB bulk cell densities for differnt Fe(III) (oxy)(hydr)oxides. Experimental data are shown as dots and the nonlinear least-squares regression fitting results using the equation of a rectangular hyperbola are shown as solid lines.

Fe(III) reduction. In 2006, Roden (2006) published a kinetics model for DIR which incorporated first-order kinetics with respect to surface site concentration of Fe(III) (oxy)(hydr)oxides and a Michaelis–Menten model (Appendix B) with respect to bulk cell density. He suggested that this model provided an adequate macroscopic description of controls on the initial rate of DIR (Roden 2006). Besides conducting lab experiments to study the factors controlling the kinetics of DIR, Roden and colleagues also measured the rates of DIR in wetland sediments, and found that the rates were first order with respect to amorphous Fe(III) oxide concentrations (Roden and Wetzel 2002).

Liu et al. (2001b) studied the kinetics of DIRB respiring on goethite and found the rate was first order with respect to the surface site concentration of goethite and had Monod-type kinetic behavior with respect to the concentration of electron donor, lactate. Biogenetic Fe(II) sorption to goethite and siderite precipitation were also studied since

these processes affected the surface site concentration of goethite. Finally, a kinetics model was developed that could successfully describe DIR rates by incorporating Monod kinetics with respect to lactate concentration, first-order kinetics with respect to the surface site concentration of goethite, the rates of Fe(II) sorption on goethite and siderite precipitation, and a Gibbs free energy availability factor.

Another relatively simple model was developed by Bonneville et al. (2004). The authors were interested in the solubility of Fe(III) (oxy)(hydr)oxides as a controlling factor of DIR, and found that the maximum rate of DIR correlated positively with the solubility of Fe(III) oxyhydroxides. They further fitted the rate of DIR directly to the Michaelis-Menten rate expression and obtained a good fit with their experimental data. This model only requires bulk cell density and the initial concentration of Fe(III) (oxy)(hydr)oxides, and therefore is much easier to apply than the models described above. However, the universality of these models still needs to be tested.

Among all the factors that have been suggested to affect DIR kinetics, biogenic Fe(II) was under intensive study. Biogenic Fe(II) could interfere with DIR by physically blocking Fe(III) (oxy)(hydr)oxides surface sites and/or DIRB cell surfaces or by limiting the mass transfer (Roden and Zacchara 1996; Urrutia et al. 1998; Liu et al. 2001b; Royer et al. 2004; Roden 2004; Hyacinthe et al. 2008). Urrutia et al. (1998) comprehensively studied the effect of biogenic Fe(II) on the rate of DIR and indicated that Fe(II) sorption to Fe(III) (oxy)(hydr)oxides and cell surfaces, together with Fe(II) precipitation with medium components, all decreased the rate of DIR; whereas Fe(II) complexation by medium components may increase the rate. In addition, the saturation of sorption sites on Fe(III) (oxy)(hydr)oxides surfaces by Fe(II) was not observed to limit the extent of DIRB

to reduce Fe(III). Royer et al. (2004) also found that DIR was self-inhibited by the production of Fe(II); however, the authors suggested that the reduction rates were controlled by mass transfer of Fe(II). In other words, as soluble Fe(II) accumulated, DIR was slowed due to a decreased thermodynamic driving force. Another recent study by Hyacinthe et al. (2008) observed that adsorbed Fe(II) did not limit the electron transfer from cell surfaces to Fe(III) mineral surfaces, and the authors hypothesized that adsorption of Fe(II) inhibited the initial DIR rates only when the surface sites of Fe(III) (oxy)(hydr)oxides or bacterial cells were (nearly) all saturated with Fe(II).

1.9 Targets of This Study

In the present research, to better understand the mechanism(s) and kinetics of DIR, the interaction between *Shewanella oneidensis* MR-1 and Fe(III) (oxy)(hydr)oxides was studied in two projects. In project I, the dissolution morphology of Fe(III) (oxy)(hydr)oxides exposed to *S. oneidensis* MR-1 was studied and compared to that exposed to a chemical reductant and Δ*gspD* mutant in the presence of an electron shuttle. The purpose of project I is to determine the reaction pathway(s) and regime(s) (surface limited or transport limited) of dissimilatory iron reduction. In project II, the adhesion behavior of *S. oneidensis* MR-1 on Fe(III) (oxy)(hydr)oxides was examined across a broad range of bulk cell densities to detect whether the spatial distribution of adhered cells would change with the bulk cell density. In addition, the relationship between the surface cell density and the bulk cell density was studied in order to further infer factors controlling rates of DIR.

CHAPTER 2

RESEARCH TECHNIQUES

This chapter focuses on introducing the major techniques used in this research to study the interaction between *Shewanella oneidensis* MR-1 and Fe(III) (oxy)(hydr)oxide mineral surfaces. Firstly, atomic force microscopy (AFM) was used to observe the dissolution morphology of Fe(III) (oxy)(hydr)oxides in different exposure experiments. Secondly, confocal microscopy was used to observe the adhesion of *S. oneidensis* MR-1 on Fe(III) (oxy)(hydr)oxides. Detailed reports on the research background, experimental methods and results are presented in Chapter 3 and Chapter 4 for dissolution morphology and bacterial adhesion, respectively. Here, the theories behind the major techniques is introduced.

2.1 Atomic Force Microscopy

The atomic force microscope is a type of high-resolution scanning probe microscope invented by Binnig, Quate and Gerber in 1986, and which enables imaging and measuring at the nanoscale. The working mechanism of the classic contact mode AFM is shown in Figure 8. The tip which sits at the end of the flexible cantilever scans the sample surface as the imaging progresses. The radius of the tip is on the order of tens of nanometers (20-60 nm), and the length of the cantilever is on the microscale. The x, y, and z position of the cantilever is controlled by an electric piezo ceramic which can adjust nanoscale changes of the cantilever based on the voltage exerted on the ceramic. When the tip approaches the sample surface, atomic forces between the tip and the

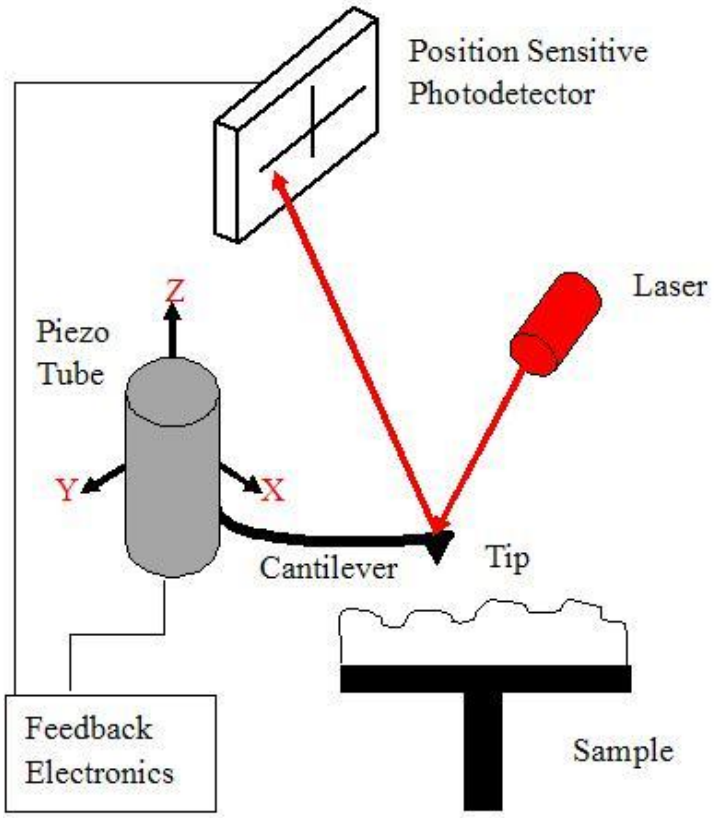

Figure 8: Block diagram of AFM.

sample lead to a deflection of the cantilever. The deflection is measured by reflecting a laser off the back of the cantilever and assessing the position of the reflected laser spot on an array of photodiode detectors. When the forces between the tip and the sample surface change, the deflection of the cantilever changes, followed by the position change of the laser spot. This information is monitored by a digital controller with a feedback loop, which is designed to adjust the electric piezo ceramic to maintain a constant deflection of the cantilever. As a result, the x, y, and z position movement of the electric piezo ceramic reflects the surface topography of the sample. AFM was named after the atomic forces between the sample surface and the tip scanning the surface.

Other models of AFM were developed besides the contact mode AFM, such as

the Acoustic Alternating Current (AAC) AFM, which is similar to the contact mode except that the cantilever is oscillated near its resonant frequency. The tip on the cantilever approaches the sample surface until the tip begins to "tap" the surface, which decreases the oscillation amplitude of the cantilever. The amplitude is monitored by laser reflection, based on which the digital controller adjusts the position of the cantilever to maintain a constant oscillation amplitude. The advantage of the AAC AFM is that the lateral forces exerted on the sample surface by the tip is less than those using contact mode, so the AAC AFM can be used to image softer materials such as bacteria without damaging them (Micic et al. 2003). AAC AFM was adopted in this research and was carried out using a PicoPlus® atomic force microscope (Agilent Technologies, formerly Molecular Imaging, Tempe, Arizona).

2.2 Confocal Microscopy

Confocal microscopy is an optical imaging technique designed especially to improve the resolution and contrast of images. The principle of confocal microscopy was patented by Marvin Minsky in 1957, aiming to overcome some of the limitations of conventional fluorescence microscopy. When using the conventional microscope, the fluorescence on the whole specimen is excited, and this large amount of excitation light is detected by the microscope's photodector at the same time. The interference of the light from the whole specimen results in a decreased resolution of images. Furthermore, the final image may become worse by the excitation from the background. Marvin Minsky adopted the idea of "optical sectioning" and utilized pinholes in the optical path to solve the problems. "Optical sectioning" means treating the specimen as a combination of different focal planes, and imaging a point on one focal plane at a time. As only one point

in the specimen is illuminated at a time, the imaging of the entire specimen requires scanning over a regular raster. This imaging approach decreases the interference of excitation light to a large extent, and therefore sharpens the image. In order to further increase the resolution, a pinhole is added before the light finally reaches the detector to eliminate out-of-focus light from specimen and background. Since only the light excited from a focal plane of the specimen can shoot through the pinhole and be detected, the resolution of the resulting image is much better than that of conventional microscopes. Furthermore, the imaging of different focal planes on the depth direction enables the reconstruction of three-dimensional structures from the obtained images.

Confocal microscopy includes several types, and a commonly used type is called confocal laser scanning microscopy (CLSM), which uses laser(s) as light source. Even though the idea of confocal microscopy was patented in 1957, it took another thirty years and the development of lasers for CLSM to become a standard technique toward the end of the 1980s. CLSM can use several lasers together as light source; however, for simplicity, the detailed principle of CLSM using one laser is described in Figure 9. A laser beam (colored blue) passes through an illumination pinhole, gets reflected by a dichroic mirror, and then becomes focused by an objective lens into a dot on a focal plane of a specimen. The excitation light (colored green) from the illuminated spot is then re-collected by the objective lens to the detector. Before reaching the detector, the excitation light passes through a confocal pinhole, which blocks the out-of-focus light, as shown by the red line in the figure. The photo signal is transferred to electric signal by the detector and recorded as one pixel. The final image is a result of the laser scanning over the plane of interest, pixel-by-pixel. A three-dimensional picture of the specimen can be generated

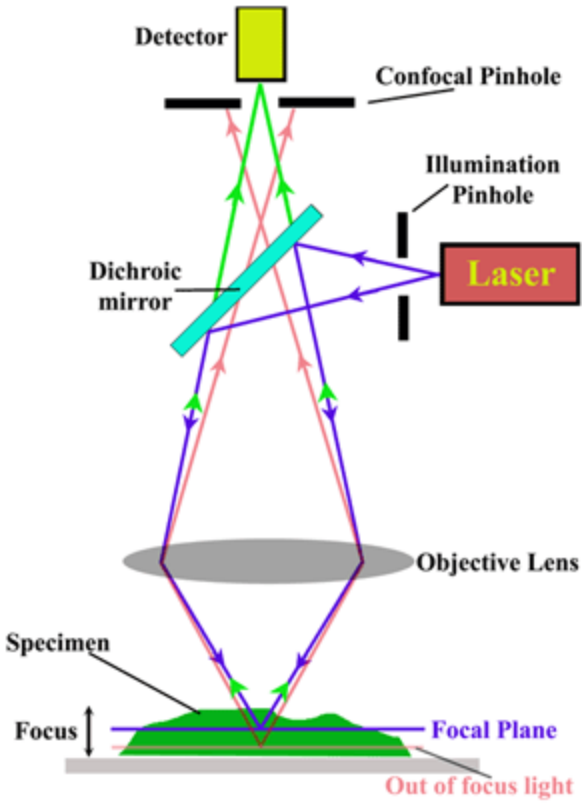

Figure 9: Principle of CLSM. (See http://www.jic.ac.uk/microscopy/more/T5_8.htm)

by assembling a stack of two-dimensional images from successive focal planes. CLSM was adopted in this research and was carried out using a Zeiss LSM 510 confocal laser scanning micrscope (Carl Zeiss, Jena, Germany).

Dye(s) is/are used to stain samples to generate excitation light when spotted by laser, and a variety of dyes have been discovered for different purposes and samples. A common dye to stain bacterial cells is called acridine orange which is cell-permeable, and interacts with DNA and RNA by intercalation and electrostatic attractions respectively. Acridine orange stains cells red and thus can show the cell distribution on mineral surfaces. Furthermore, some dyes are able to separate live cells from dead cells, such as the LIVE/DEAD BacLight Bacterial Viability Kit (from Invitrogen). The kit employs two

nucleic acid stains which differ in their ability to penetrate healthy bacterial cells. One stain penetrates all cells whereas the other stain only penetrates damaged cells, and thus the dye stains live cells green and dead cells red. Both acridine orange and LIVE/DEAD BacLight Bacterial Viability Kit were utilized in this research for observation of bacterial adhesion and distribution on mineral surfaces.

CHAPTER 3

DISSOLUTION MORPHOLOGY OF FE(III) (OXY)(HYDR)OXIDES EXPOSED TO DISSIMILATORY IRON REDUCING BACTERIUM *SHEWANELLA ONEIDENSIS* MR-1

3.1 Abstract

Atomic force microscopy was used to compare the dissolution morphology of Fe(III) (oxy)(hydr)oxides exposed to a dissimilatory iron reducing bacterium *Shewanella oneidensis* MR-1 and a Type II protein secretion mutant impaired to reduce Fe(III) minerals without an exogenous electron shuttle. Dissolution morphology of Fe(III) (oxy)(hydr)oxides exposed to the wild-type organism was heterogeneous and correlated with the morphology of bacterial microcolonies observed by confocal microscopy. In contrast, dissolution morphology of Fe(III) (oxy)(hydr)oxides exposed to wild-type or mutant strains with the electron shuttling compound 9,10-anthraquinone-2,6-disulfonate was homogeneous. In addition, dissolution morphology of Fe(III) (oxy)(hydr)oxides exposed to a chemical reductant is also homogeneous. These results suggest that dissimilatory iron reduction may be in part transport limited, and the addition of exogenous electron shuttling compounds relieves this limitation.

3.2 Introduction

Dissimilatory iron reducing bacteria (DIRB) are common in terrestrial soils, freshwater and marine sediments, and near-surface groundwater environments due to the

variety of species and the abundance of Fe(III) (oxy)(hydr)oxides in these environments (Fredrickson and Gorby 1996; Nealson and Little 1997). Dissimilatory iron reduction (DIR) is important to a number of natural processes such as the biogeochemical cycling of iron, carbon, and other elements and the weathering of Fe(III)-bearing clays and minerals (Fredrickson and Gorby 1996; Kostka et al. 2002; Koretsky et al. 2003; DiChristina et al. 2005; Taillefert et al. 2007). DIRB may also play an important role in bioremediation of metal- or radionuclide-contaminated sites (Lovley 1991; Nealson and Saffarini 1994; Fredrickson and Gorby 1996; Wade and DiChristina 2000; Payne and DiChristina 2006).

The parameters that control the kinetics of DIRB respiration and the bioavailability of Fe(III) (oxy)(hydr)oxides are poorly understood. Kinetic models applied to DIRB activity are often designed for homogeneous phase reactions (i.e., soluble terminal electron acceptors) and may not reflect the mechanistic processes that limit the extent and rate of respiration on mineral surfaces. It has been found that DIR rates correlate with mineral solubility (Bonneville et al. 2004) and surface area (Roden and Zachara 1996; Zachara et al. 1998; Roden 2003); yet at high bulk cell densities the dependence of the DIR rate on surface area is much weaker than in the presence of excess chemical reductant (Roden 2003). Similarly, a non-linear dependence of the DIR rate on the bulk cell density has been reported (Roden 2003). These findings suggest that processes important to model the kinetics of DIR have not been fully studied.

Bacterial adhesion to Fe(III) (oxy)(hydr)oxides may affect DIR kinetics: Bonneville et al. (2006) predicted that high ratios of Fe(III) (oxy)(hydr)oxide colloids to bacterial cell densities can limit the rate due to a limited adsorption capacity of the

colloid onto bacterial cells. The extent of adhesion onto Fe(III) (oxy)(hydr)oxides by DIRB cells have been examined in previous studies. Neal et al. (2003) found that under flowing solution (320 μm/s), accumulation of cells onto hematite surfaces continues for nearly 100 hours and adhered cell densities saturate at approximately one cell per 1500 μm^2 of mineral surface area. Cell adhesion to magnetite is much faster (20-30 hours for saturation) but with a lower maximum adhesion density (1 cell / 2500 - 3000 μm^2). For both magnetite and hematite, the adhesion densities are much smaller than a closest packing arrangement of bacterial cells, which would be on the order of one cell per few square micrometers. The DIR rate correspondingly saturates at a ratio of bulk cell density to surface area of approximately one cell per 100 μm^2 (data from Roden 2003), which is also a much lower cell density than expected for closest packed cells adhered to a mineral surface. Reasons for the low adhesion densities are unclear.

The molecular mechanism by which the DIRB reduce Fe(III) (oxy)(hydr)oxides is currently under intense investigation. Four pathways have been postulated, including (1) a direct contact pathway in which DIRB reduce Fe(III) (oxy)(hydr)oxides via outer membrane (OM)-localized ferric iron reductases (Beliaev and Saffarini 1998; DiChristina et al. 2002; Myers and Myers 2003; DiChristina et al. 2005; Shi et al. 2008). (2) A two-step electron shuttling pathway in which DIRB enzymatically reduce dissolved electron shuttling compounds, followed by a chemical oxidation-reduction reaction between the reduced electron shuttling compounds and Fe(III) (oxy)(hydr)oxides (Newman and Kolter 2000; Turick et al. 2002; Kappler et al. 2004; Jiang and Kappler 2008). The electron shuttles are termed either exogenous (not intrinsically produced by the organisms), or endogenous (produced by the organisms). (3) A two-step ferric iron

solubilization-reduction pathway in which solid Fe(III) (oxy)(hydr)oxides are first dissolved via chelation by an organic ligand and subsequently reduced by periplasmic ferric iron reductases (Arnold et al. 1988; Lovley and Woodward 1996; Pitts et al. 2003; Taillefert et al. 2007). (4) A pathway in which electroactive appendages (termed nanowires) transfer electrons from the cell surface to the surface of Fe(III) (oxy)(hydr)oxides under electron acceptor-limiting conditions (Reguera et al. 2005; Gorby et al. 2006).

In previous studies, Fe(III)-reduction deficient mutant strains of *Shewanella putrefaciens* were found to contain a mutation in a gene (*gspE*) encoding the traffic ATPase of the type II protein secretion system that transports exo-proteins to the exterior of the outer membrane of gram-negative cells (Pugsley 1993; DiChristina et al. 2002). Similar results have been reported for *S. oneidensis gspD* gene that encodes the outer membrane porin of the type II secretion system (Shi et al. 2008). The lack of a properly functioning type II protein secretion system renders the organism incapable of reducing Fe(III) (oxy)(hydr)oxides at wild-type rates and indicates that the terminal ferric iron reductases, and/or other integral components of the electron transport chain, are localized to the outer membrane of the cell (DiChristina et al. 2005). The Fe(III) reduction activity of the type II protein secretion mutants is rescued by addition of exogenous electron shuttling compounds such as 9,10-anthraquinone-2,6-disulfonate (AQDS). AQDS reduction by both the wild-type and type II secretion mutants results in the production of 9,10-anthrahydroquinone-2,6-disulfonate (AH_2DS) which catalyzes the abiotic reduction of Fe(III).

The dissolution morphology of Fe(III) (oxy)(hydr)oxides exposed to DIRB

may be used as an indicator of bacterial activity. Grantham et al. (1996, 1997) found wide-spread mineral loss under anaerobic conditions for Fe(III) (oxy)(hydr)oxides exposed to *S. putrefaciens* strain 200. *S. putrefaciens* CN32 was found to reduce crystalline hematite platelets at surface locations that do not correlate with observed points of cell adhesion (Rosso et al. 2003a). This morphology can be explained by models suggesting that the diffusion rate of electrons in bulk hematite causes injected electrons to migrate quickly to high energy sites prior to dissolution (Rosso et al. 2003b; Kerisit and Rosso 2006, 2007).

In the present study, the experimental setup of Grantham et al. (1996, 1997) was improved by using a completely anoxic imaging process. This technique was used to examine the dissolution morphology of amorphous Fe(III) (oxy)(hydr)oxides in the presence of a wild-type and Fe(III)- reduction deficient mutant of *S. oneidensis* strain MR-1. These microbially catalyzed dissolution morphologies are compared to those resulting from exposure to AQDS and the abiotic, purely chemical reduction by AH_2DS. Finally, confocal microscopy was performed on Fe(III) (oxy)(hydr)oxides exposed to the wild-type organism to determine if the site of bacterial adhesion correlates to the dissolution morphology.

3.3 Materials and Methods

3.3.1 Preparation of Fe(III) (Oxy)(hydr)oxides

Fe(III) (oxy)(hydr)oxides were grown on glass slides forming a layer of homogeneous particle coatings, following the procedure described in Grantham et al. (1997). The glass slides were cleaned with 30% H_2O_2 for 3 hours and then etched in 5 M

NaOH overnight. The slides were then sonicated in ≥ 18.2 MΩ-cm, < 15 ppb total organic carbon, filtered, deionized water (DIW) 5 times for 15 minutes each to wash any residues on the surface of glass slides. The prepared glass slides were placed flat in a 5 mL 0.1 M $FeSO_4$ solution. The $FeSO_4$ was gradually oxidized by dropwise addition of 30% H_2O_2 until the reaction ceased. The solution was stored overnight to ensure abundant growth of particles on the glass slides. Afterwards, the coated glass slides were removed from solution, dried, and heated in an oven at 90 °C for one hour. The coated glass slides were then sonicated in DIW 5 times for 15 minutes each with water replacement in the interval. The slides were dried overnight and subsequently stored in a dust-free environment at room temperature. The coatings tended to be uniform and dense, with an average particle diameter of approximate 0.5 μm measured with atomic force microscopy (see below). X-ray diffraction analysis of bulk samples prepared the same way showed two weak peaks at 35 °and 62 °2Θ (data not shown), only marginally consistent with 2-line ferrihydrite (Jambor and Dutrizac 1998; Murad and Rojik 2004). Since the existing weak peaks do not match 2-line ferrihydrite precisely and due to the largely amorphous nature of the particles, here they will continue to be referred to ambiguously as Fe(III) (oxy)(hydr)oxides. Some variation in particle morphology and density was noted from slide to slide, thus each slide was characterized prior to exposure.

3.3.2 Preparation of AQDS and AH_2DS

AQDS was used as received (Sigma-Aldrich) and dissolved in water at room temperature. AH_2DS was prepared by bubbling ultra high purity H_2 (Airgas) through a AQDS solution containing palladium covered ceramic pellets that catalyzed reduction (Coates et al. 2001). The pellets were rinsed in DIW several times prior to use. Vigorous

bubbling was maintained for at least 15 minutes per 200 mL of solution; reduction was confirmed by noting a color change from yellow to orange and spectrophotometric analysis of the absorbance peak at 386 nm (Jaisi et al. 2007).

3.3.3 Bacterial Culture Conditions

S. oneidensis MR-1 and the *S. oneidensis* targeted in-frame deletion mutant (Δ*gspD*) were routinely cultured at 30 ℃ in Luria Broth media with vigorous aeration. After 12 hours of growth, cells were harvested by centrifugation and were washed twice with a defined salt medium (Myers and Nealson 1988) supplemented with 20 mM lactate at pH 7.5. Cells were subsequently resuspended in anoxicsalt mediumto a final density of 10^8 cells/mL as determined by optical density using a Shimadzu UV-1601 spectrophotometer at 600 nm. To minimize oxygen contamination, all cultures and exposure experiments were incubated in a model 1025/1029 Forma Anaerobic System (Thermo Electron). The anaerobic gas consisted of a high purity mixture of 10% hydrogen, 5% CO_2 and the balance nitrogen (Airgas). Oxygen and hydrogen levels were continuously monitored via a Coy Model 10 gas analyzer.

3.3.4 Atomic Force Microscopy (AFM)

All samples were examined using a PicoPlus® atomic force microscope (AFM) (Agilent Technologies, formerly Molecular Imaging, Tempe, Arizona) in the acoustic alternating current mode. All experiments were performed in the same fluid cell that was used to image thereby allowing direct, *in situ*, and repeatable imaging of the samples without exposure to oxygen. The fluid cell volume was 650 μL and the approximate cross-sectional area was 0.79 cm^2. The method of Grantham et al. (1996, 1997) was improved upon by maintaining an anaerobic environment throughout the entire imaging

process, thereby avoiding any artifacts caused by inadvertent ferrous iron chemical oxidation or inhibition of DIR by oxygen. The entire microscope head and environmental chamber were placed into the anaerobic chamber prior to imaging, the previously exposed sample was loaded onto the microscope head which was then sealed by the environmental chamber, and the now sealed microscope head was removed from the anaerobic chamber. After imaging, the sample was returned to the anaerobic chamber for further exposure until the experiment terminated. This routine ensures that the disturbance to the sample by imaging is minimal outside the AFM scan area.

A multi-purpose large scanner was used with a maximum imaging area of up to 85 × 85 μm. Non-contact high frequency silicon tips were used (PPP-NCH, Agilent Technologies). All the samples were examined at room temperature with a scan rate of 0.5 Hz for biotic experiments to minimize cell disruption and tip damage and 1 Hz for abiotic exposure experiments. Raw data were processed by flattening using a linear line-by-line fit in the horizontal (fast scan) direction. Unless otherwise noted, root-mean-square (RMS) roughness was calculated on the entire image after flattening. The error on the average measurements is the standard deviation over all replicates.

3.3.5 Exposure Experiments

Exposure experiments using Fe(III) (oxy)(hydr)oxides coated glass slides were conducted at 30 ℃ in the dark and each was repeated at least three times to confirm reproducibility. Six different types of experiment were performed: (1) An abiotic control in which Fe(III) (oxy)(hydr)oxides were exposed only to thesalt mediumto determine if the coatings dissolve in growth media and remain adhered during imaging, (2) A wild-type exposure in which Fe(III) (oxy)(hydr)oxides were exposed to wild-type *S.*

oneidensis MR-1 in salt medium, (3) A biotic control in which Fe(III) (oxy)(hydr)oxides were exposed to the Δ*gspD* mutant insalt mediumto verify that Δ*gspD* mutant is not able to reduce Fe(III) (oxy)(hydr)oxides at the same rate as the wild-type nor detach the particles, (4) An abiotic reduction in which Fe(III) (oxy)(hydr)oxides were exposed to 1 mM AH_2DS in water, (5) An exposure in which Fe(III) (oxy)(hydr)oxides were exposed to Δ*gspD* mutants in the presence of 0.5 mM AQDS in salt medium, and (6) A positive control in which the wild-type strain was inoculated in the presence of 0.5 mM AQDS andsalt medium.

3.3.6 Dissolved Iron

The concentrations of total dissolved iron were measured using the ferrozine (FZ) methodology (Stookey 1970) in the same type of experiments as described above. Hydroxylamine hydrochloride was used as a reductant as some re-oxidation of iron was observed. All solutions were filtered through 0.2 μm filter to prevent interference by bacterial cells and secondary mineral precipitation (only aqueous iron was measured, not any present as secondary minerals, Zachara et al. 1998). For the control and experiments containing cells, standard curves were measured insalt mediumamended with iron stock solution. For abiotic measurements containing AH_2DS, the standard curve was created by diluting the iron stock solution. Abiotic solutions containing AH_2DS were titrated to pH 7 using sodium hydroxide prior to the absorbance measurement.

3.3.7 Confocal Microscopy

A fluid cell was implemented for *in situ* confocal imaging that used the same exposure conditions and set-up as in the AFM experiments. This was accomplished by fixing the same fluid cell used in the previous AFM imaging processes onto a standard

microscopy slide (75 × 25 mm) that was uniformly coated with Fe(III) (oxy)(hydr)oxides as described above. The slide was exposed to 650 μL of bacterial suspension containing 10^8 cells/ml wild-type *S. oneidensis* MR-1, in a 0.79 cm^2 cross-sectional area (again, as above). After 24 hours, the suspension was stained with 0.01% acridine orange (Acros) suspension and prepared for imaging. Most of the suspension was carefully removed leaving behind a drop of stained bacterial suspension in the middle of the coated slide. A small volume of solution was necessary because the final assembly needed to be thin enough to accommodate the working distance of the confocal objective, 2.5-3.3 mm. A cover slip (22 × 22 mm) was used to cover the drop of suspension, and the periphery of the cover slip was sealed with clear nail polish and allowed to dry for 30 minutes. All preparations were performed in the anaerobic chamber to limit oxygen contamination. Samples were imaged using a Zeiss LSM 510 confocal microscopy with a 20× air objective and excited used a 543 nm Helium-Neon laser.

3.4 Results

Neither dissolution features nor changes in particle size of the Fe(III) (oxy)(hydr)oxide coatings were observed in the abiotic control experiment where coated slides were exposed solely tosalt mediumfor 2 days (Figure 10). The horizontal streaks in Figure 10a (taken in air) show that some particles are removed by the AFM tip and/or exposure to thesalt mediumbut most remain adhered. Prior to imaging, the average RMS roughness of all the coated slides used in these experiments is 98 ± 14 nm. After being exposed to growth media for 2 days, the average roughness does not change significantly at 96 ± 20 nm. Dissolved iron was not detected in any of the replicates.

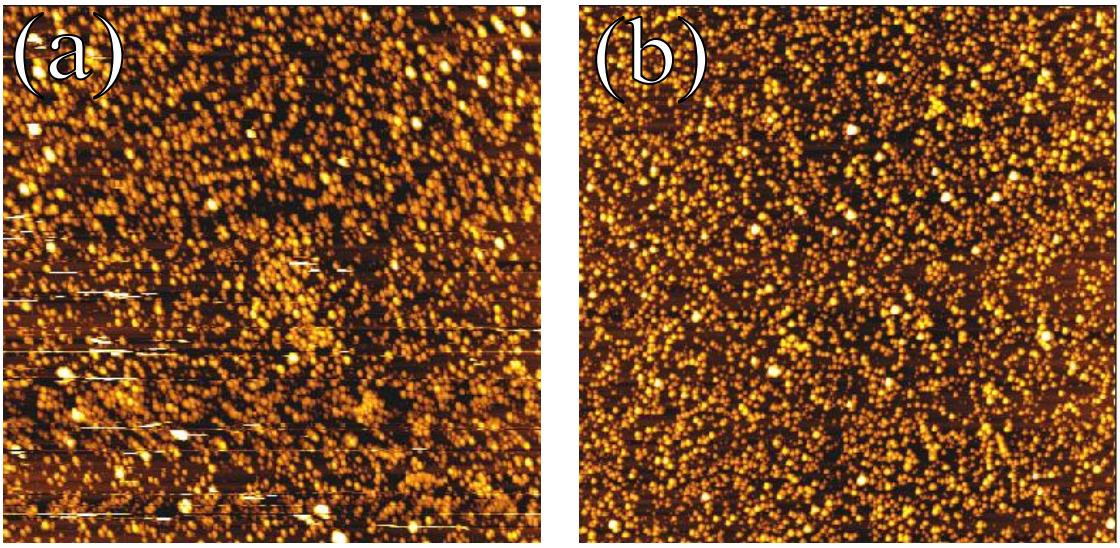

Figure 10: Abiotic control. AFM images showing absence of dissolution features after a 1-day anaerobic exposure. (a) 68 μm image of the original Fe(III) (oxy)(hydr)oxide coated surface. RMS roughness is 114 nm. (b) 68 μm image taken after 2 days of anaerobic exposure in growth media and no obvious dissolution was found. RMS roughness is 105 nm. Z-scale is 428 nm for both (a) and (b).

Fe(III) (oxy)(hydr)oxides exposed to wild-type *S. oneidensis* MR-1 displayed dissolution features that were much larger than the size of individual bacterial cells after 1 day (Figure 11). Measurements of the length of the longest axis of these features ranged from 6 μm to 86 μm with an average of 31 ± 21 μm. Within the dissolved areas, the slides were completely devoid of particles leaving only the glass surface underneath (the dark portions of Figure 11). In areas outside the dissolution features, the Fe(III) (oxy)(hydr)oxide particles remained in approximately the same density and size as those in the unexposed slides. Supporting this qualitative observation, the average RMS roughness for slides exposed to the wild type organism was found to be 105 ± 20 nm, consistent within error to that of the abiotic control slides and the roughness of slides prior to exposure to the wild-type cells. This morphology will be referred to as heterogeneous dissolution morphology since in some portions of the slides the particles

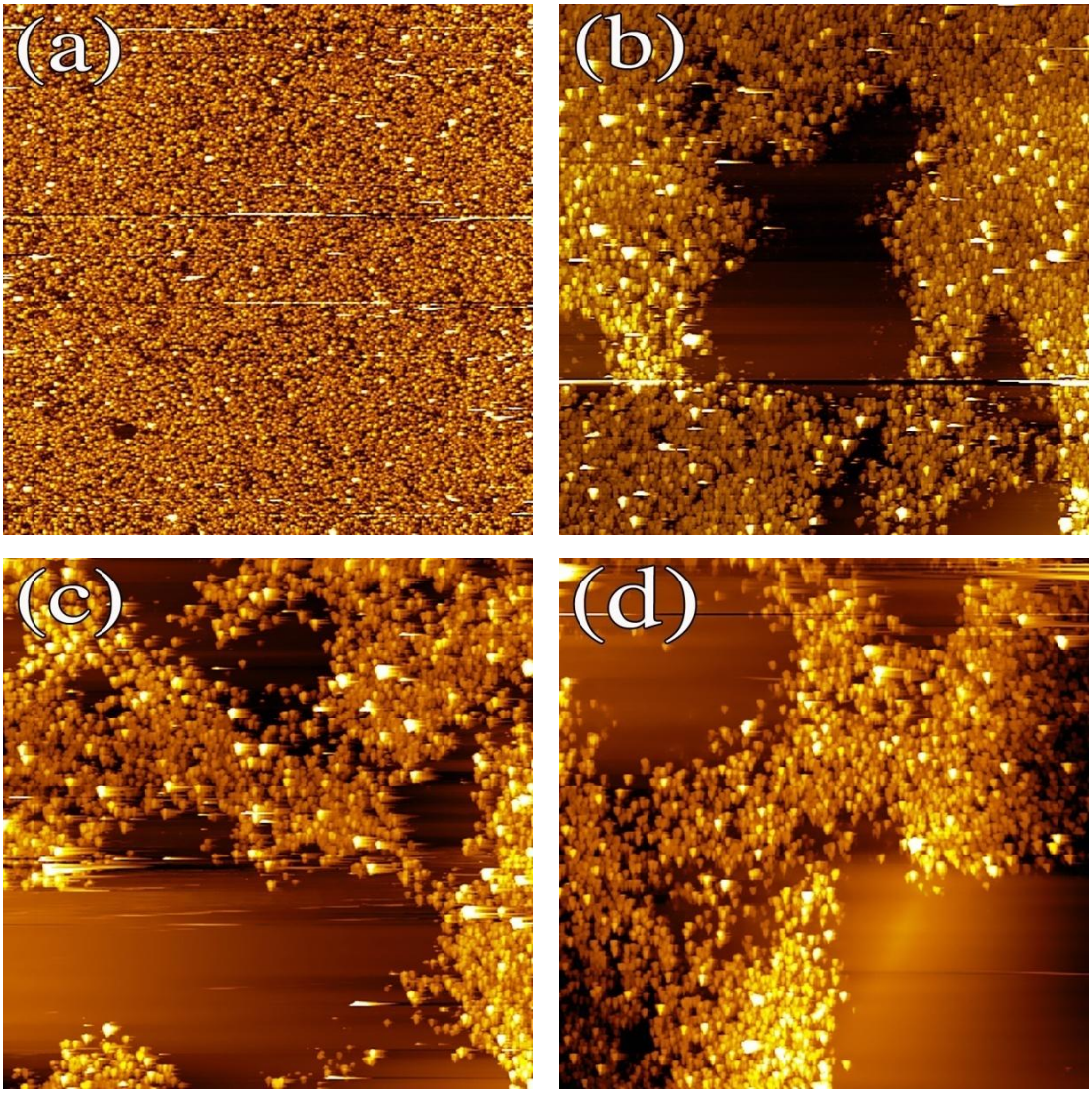

Figure 11: Wild-type *S. oneidensis* MR-1. 85 μm AFM images of Fe(III) (oxy)(hydr)oxide coated slides. (a) Fe(III) (oxy)(hydr)oxide coated slide prior to incubation, RMS roughness is 86 nm. (b-d) Slide after 1-day of anaerobic exposure to *S. oneidensis* MR-1. Some portions of the coating are dissolved completely, exposing the glass slide underneath, while other portions are not dissolved, i.e., a heterogeneous dissolution morphology. RMS roughness for (a) 87 nm, (b) 100 nm, and (c) 88 nm. Z-scale is 392 nm for all images.

were dissolved completely but the remaining particles are approximately the same size as unexposed. This morphology is the same as that found in previous work on slides exposed to *S. putrefaciens* strain 200 (Grantham et al. 1996, 1997). The average total

dissolved iron in this experiment was 220 ± 17 μM after 1 day, consistent with previous measurements of reduction rates of hydrous Fe(III) oxides by *S. putrefaciens* CN32 (Roden, 2003). After 3 days, the imaging conditions degraded due to obfuscation by an as of yet unidentified soft material (data not shown). All subsequent experiments containing bacterial cells showed similar obfuscation after 3 days exposure.

Fe(III) (oxy)(hydr)oxides exposed to the Δ*gspD* mutant displayed little obvious dissolution within 1 day (Figure 12). The average RMS roughness of the coatings exposed in this manner was 84 ± 4 nm. This finding indicates that the bacterial cells themselves do not substantially detach the particles from the slide. The average total dissolved iron after 1 day was 120 ± 35 μM, ~45% of the wild-type strain. The dissolved iron concentration is lower than that of the wild-type strain and consistent with the observed decrease in RMS roughness relative to the abiotic control. Fe(III) reduction rates of approximately 20-40% of the wild-type strain have been previously observed using the Δ*gspE* mutant of *S. putrefaciens* strain 200 (DiChristina et al. 2002) and the Δ*gspD* mutant of *S. oneidensis* MR-1.

In contrast to the wild type MR-1 exposure, Fe(III) (oxy)(hydr)oxides exposed to an excess of a chemical reductant (1 mM AH_2DS) resulted in uniform dissolution of all of the particles, i.e., a homogeneous dissolution morphology (Figure 13). The average RMS roughness of the slides was measured at 28 ± 4 nm, a substantial decrease relative to the abiotic control slides or those exposed to the wild-type organism. The concentration of total dissolved iron was measured at 370 μM, 170% of the wild-type concentration without AQDS. After 1 day of exposure, nearly all particles had dissolved (data not shown).

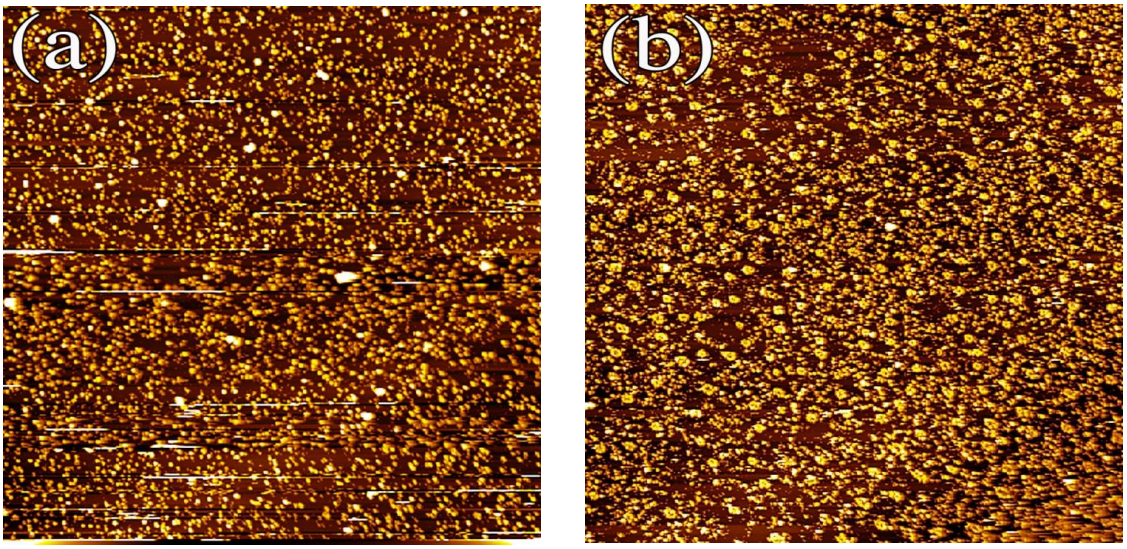

Figure 12: Δ*gspD* mutant. 85 μm AFM images showing absence of dissolution features after 1-day anaerobic exposure. (a) Fe(III) (oxy)(hydr)oxide coated surface prior to incubation. RMS roughness is 104 nm (if horizontal streaks are removed, RMS roughness is 97 nm). (b) The same slide after 1-day anaerobic exposure to ΔgspD mutants, substantial dissolution is not observed. RMS roughness is 80 nm. Z-scale is 370 nm for (a) and (b).

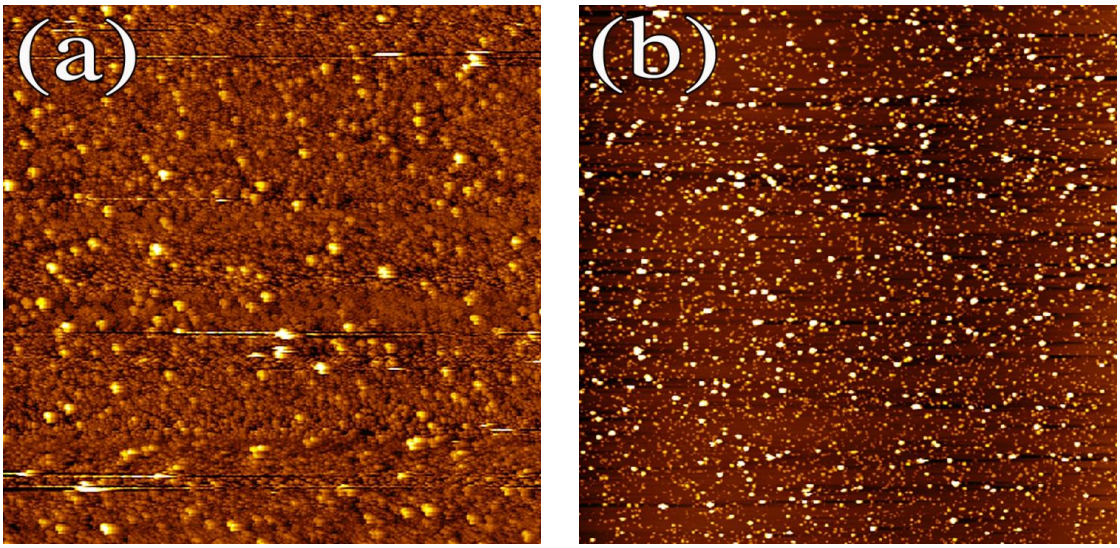

Figure 13: Chemical Reductant, AH_2DS. 85 μm AFM images of Fe(III) (oxy)(hydr)oxide coated slides. The concentration of AH_2DS is 1 mM. (a) Fe(III) (oxy)(hydr)oxide coated slide prior to incubation, RMS roughness is 80 nm. (b) Image shows simultaneous dissolution of the entire Fe(III) (oxy)(hydr)oxide particles after 9 h of anaerobic exposure. RMS roughness is 26 nm. Z-scale is 404 nm for (a) and 78 nm for (b).

Fe(III) (oxy)(hydr)oxides exposed to 0.5 mM AQDS and the Δ*gspD* mutant also resulted in homogeneous dissolution morphology after 9 hours (Figure 14). The average RMS roughness of the coatings was 8 ± 1 nm, a substantial decrease relative to other exposures. The average total dissolved iron after 9 hours was 240 ± 31 μM, similar to the wild-type levels after 1 day exposure. This indicates that the addition of AQDS substantially increases the Fe(III) reduction rate by the mutant. A similar dissolution morphology was observed on slides that were exposed to wild type organisms and 0.5 mM AQDS, but was difficult to discern since the entire coating was dissolved within 2 hours (data not shown). The total dissolved iron after 9 hours for the wild-type with AQDS was 260 ± 34 μM, which was comparable to that of the Δ*gspD* mutant and AQDS.

In situ confocal microscopy of Fe(III) (oxy)(hydr)oxides exposed to the wild-type strain (Figure 15) revealed that the cells form microcolonies on the mineral surfaces. The large fluorescent features in Figure 15 are composed of numerous bacterial cells as well as abundant adhered single or small clusters of cells. Some interference is observed in Figure 15a due to fluorescence of Fe(III) (oxy)(hydr)oxide particles. Sizes of colonies ranged from 6 - 70 μm with an average of 36 ± 19 μm, consistent with the size of dissolution features observed in Figure 11.

3.5 Discussion

3.5.1 Origin of the Dissolution Morphology Produced by a Chemical Reductant

Dissolution promoted by small soluble chemical reductants (such as quinones) is a surface limited process where the rate of reactions on the surface is controlling the overall rate. This is opposed to a transport limited reaction, in which case the transport of

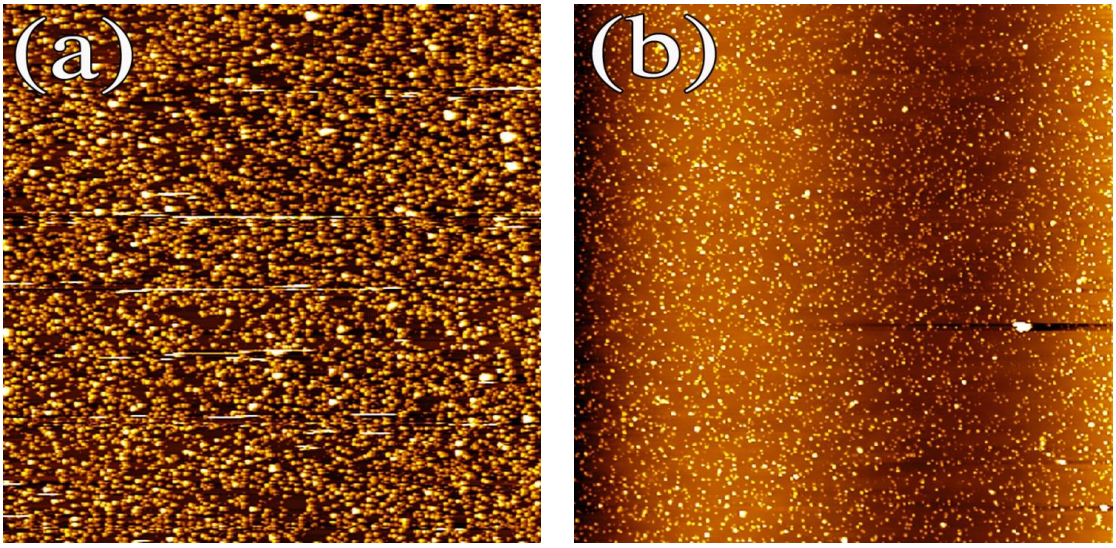

Figure 14: Δ*gspD* mutant supplemented with 0.5 mM AQDS. 85 μm AFM images. (a) Original slide, RMS roughness is 106 nm. (b) After 9 hours aerobic exposure, image shows substantial homogeneous dissolution. RMS roughness is 10 nm. Z-scale is 388 nm for (a) and 37 nm for (b).

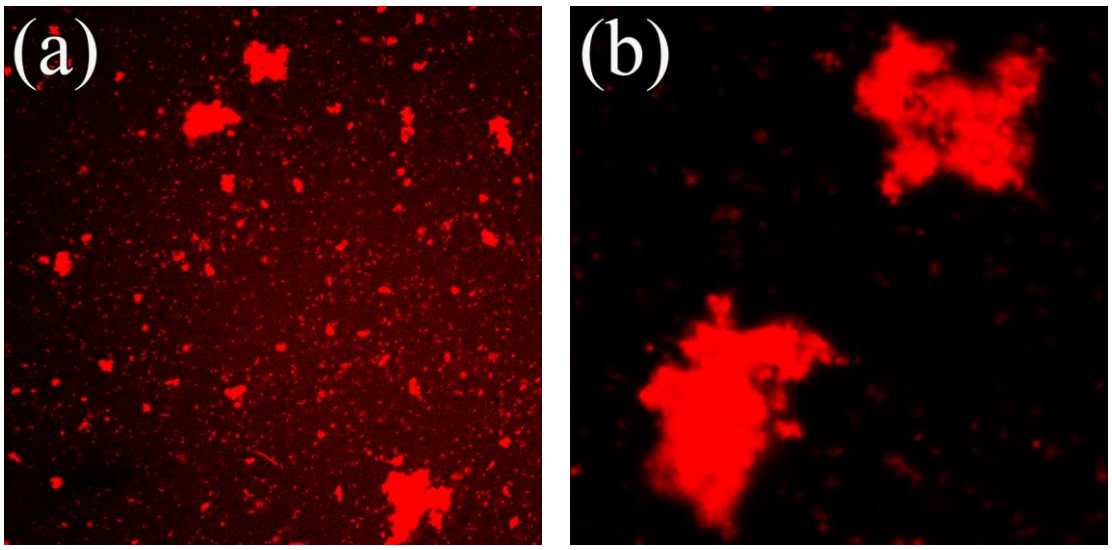

Figure 15: Confocal microscopy wild-type *S. oneidensis* MR-1. After 1 day of anaerobic exposure to Fe(III) (oxy)(hydr)oxides, microcolonies of organisms were observed that have roughly the same size and shape as the dissolution morphologies observed by AFM in Figure 11. (a) Image size is 461 μm. (b) Image size is 103 μm.

molecules is limited and affects the overall rate (Zinder et al. 1986). Surface limited reductive dissolution by small soluble reductants is probably not limited by the rate of electron transfer from the reductant to Fe(III) (oxy)(hydr)oxide surfaces (Stack et al. 2004a; Stack et al. 2004b), nor by the extent of adsorption of Fe(II) (Hyacinthe et al. 2008), but by other surface processes, possibly detachment of reduced iron (Suter et al. 1991) or adsorption/desorption of the reductant. To demonstrate that diffusion is relatively fast in this system, the displacement of an AH_2DS molecule is estimated. The mean square displacement of diffusion, χ, indicates the average distance a given molecule travels during the experiment:

$$\chi = (2Dt)^{1/2} \quad (1)$$

where *t* is the time (1 day) and *D* is the diffusion coefficient, estimated by the Stokes-Einstein Relation:

$$D = kT/6\pi\eta r \quad (2)$$

where *k* is the Boltzmann constant, *T* is temperature, η is the viscosity of the medium (for water: 10^{-3} kg $m^{-1}s^{-1}$), and *r* is the radius (for AH_2DS and AQDS $\approx$ 7.4 Å). Based on equations (1) and (2), *D* for AQDS is 3×10^{-6} cm^2/s and χ for a 1-day exposure is 7.2 mm, more than two orders of magnitude larger than the scale at which dissolution is observed. Thus AH_2DS, AQDS and dissolved iron ($D = 10^{-5}$ cm^2/s) diffuse much more rapidly than dissolution occurs, even in an unmixed system such as this, and all particles in this system are exposed to similar concentrations of reactant.

Among Fe(III) (oxy)(hydr)oxides, only the highly crystalline, oxide-phases hematite and magnetite have sufficiently small band gaps to give appreciable conductivity (Xu and Schoonen 2000), indicating that the amorphous material used here

is likely to be a poor conductor. Additionally, the particles in this study are physically separated so electrons are not likely to migrate between particles. These observations suggest that the fast electron migration ($D = 1.6 \times 10^{-3}$ cm^2/s, Rosso et al. 2003b) that was postulated to produce the dissolution morphology on hematite platelets (Rosso et al. 2003a) should not be a factor in this system. Therefore, we conclude that all particles dissolve uniformly over the course of the experiment, producing the homogeneous dissolution morphology.

3.5.2 Origin of Wild-type Dissolution Morphology and Reaction Regimes of DIR

If the bulk cell density was low enough to limit the dissolution rate, this seem to be the most obvious possibility as to cause the heterogeneous dissolution morphology of Fe(III) (oxy)(hydr)oxides exposed to wild type cells (Figure 11); however, this is unlikely because the ratio of cells to slide surface area used in these experiments is ~1 cell/μm^2. This ratio is much higher than the ratio necessary to maximize bacterial respiration rate (Roden 2003; Neal et al. 2003 see above). A more likely possibility is that the dissolution morphology results from a transport limited process, specifically the movement of bacterial cells across the mineral surface. If equations (1) and (2) are used to calculate the mean square displacement of diffusion for a 1 μm radius bacterial cell, the predicted displacement is ~200 μm over one day (or 0.7 μm over one second). This displacement is much smaller than that of a small, soluble chemical reductant and is approaching the size of the observed dissolution features. *S. oneidensis*, however, possesses a single polar flagellum (Myers and Nealson, 1988) that will increase its apparent rate of diffusion in solution. The swimming velocity of *S. oneidensis* has not been reported, but Johansen et al. (2002) observed that other *Shewanella* species (*S. pealeana* and *S. frigidimarina*)

swim at 20-27 μm/s. These swimming velocities are approximately 3-4 fold faster than diffusion of a bacterially sized-sphere and far faster than what could control the creation of the dissolution features observed in Figure 11. Furthermore, *S. oneidensis* may be conducting a directed movement in solution (Bencharit and Ward 2005) which will further increase any apparent rate of diffusion.

Once near the surface or adhered to it however, the bacteria will no longer be able to swim as effectively, if at all (Lauga et al. 2006; Lower et al. 2000). Thus adhesion of the bacterial cells to the mineral surface and/or surface diffusion of the cells could control the rate of dissolution. In stirred batch reactors, adhesion of *Shewanella algae* BrY to Fe(III) (oxy)(hydr)oxides is on the order of minutes (Caccavo et al. 1997) but somewhat lower rates and extents of adhesion to hematite were observed (Caccavo and Das 2002). Strength or rates of adhesion have yet to be determined in this system, which is unmixed (Neal et al. 2003 used flowing solution). An indirect inference about adhesion strength can be made however: although direct adhesion of live cells was not observed *in situ* using the AFM in the present study, cells were observed on mineral surfaces *ex situ*, i.e. once the solution was decanted (Figure 16). This indicates that the lateral force of the AFM tip while scanning is sufficient to detach the cells *in situ*, but once the solution is decanted the cells are no longer moved by the tip, presumably because they are less buoyant in air. Regardless, forces governing adhesion and colony structure *in situ* do not seem to be especially large.

Also necessary to be considered is that some *Shewanella* species are known to form microcolonies on glass surfaces while respiring aerobically (Thormann et al. 2004). Figure 15 shows that microcolony formation also occurs for cells respiring anaerobically

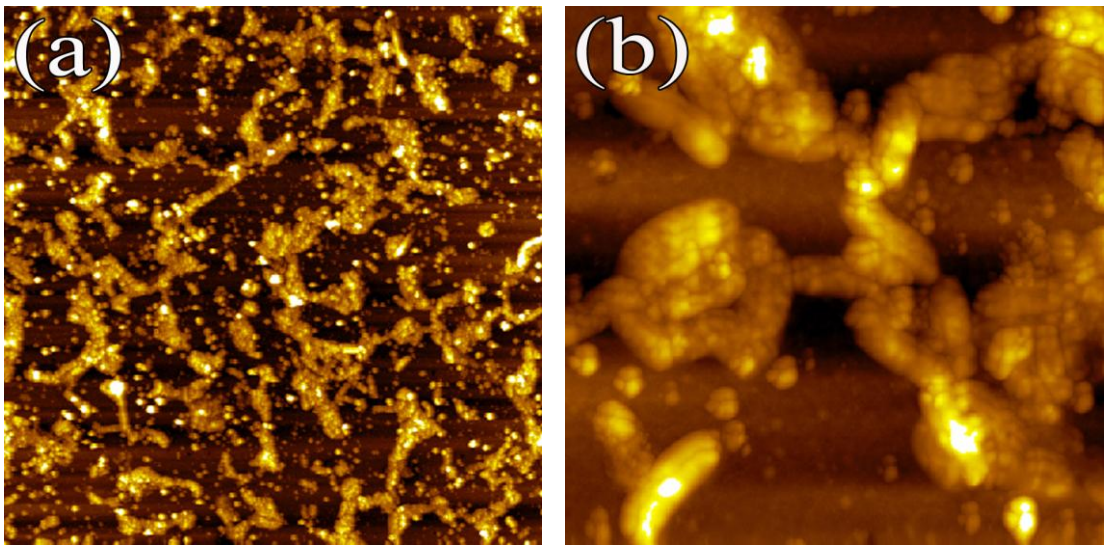

Figure 16: Wild-type *S. oneidensis* MR-1, *ex situ*. AFM images of adhered bacterial cells on Fe(III) (oxy)(hydr)oxides immediately after the overlying growth media was decanted. (a) Image size is 85 μm. Z-scale is 377 nm. (b) Image size is 15 μm. Z-scale is 377 nm.

on Fe(III) (oxy)(hydr)oxide surfaces. The cells in *Shewanella* colonies presumably move on the mineral surface using Type IV pili, which is categorized as a twitching or social gliding type of movement (Harshey 2003). The dissolution features observed in Figure 11 may indicate the locations of the colonies observed in Figure 15 as they are commensurate in size. As discussed above, the dissolution features are much smaller than what could be produced by diffusion of a small molecule yet much larger than single bacterial cells. If the dissolution features of Fe(III) (oxy)(hydr)oxides exposed to the wild-type strain correspond to the sites of initial microcolony formation, this would indicate that the rate of dissolution is limited by the rates of new microcolony formation and growth. The rate of movement of *S. oneidensis* cells or expansion of colonies is not known on any Fe(III) (oxy)(hydr)oxides, but a reported colony expansion velocity of *Shewanella* colonies on agar is in the range of 0.06 - 0.3 μm/s (Harshey, 2003). This

estimate is of sufficient magnitude to account for the size of observed dissolution features and the complete coverage of the surface with soft material after three days. Regardless of which step(s) in the bacterial adhesion, colony formation, growth or respiration process is limiting, the initial dissolution rate is likely to be limited in part by movement of *S. oneidensis* cells. Presumably, once the cells are adhered, the rate of respiration is then limited by the rate of reductive dissolution. This explanation is consistent with the observed correlation of rate with mineral solubility (Bonneville et al. 2004) and the lack of a linear correlation between DIR rate and the bulk cell density (Roden, 2003).

The dissolution morphology observed in the presence of AQDS and either the wild-type *S. oneidensis* or the Δ*gspD* mutant strains (Figure 14) resemble the dissolution morphology of the abiotic chemical reductant, AH_2DS (Figure 13). Microbial AQDS reduction appears to relieve the potential bacterial cell transport limitation because the AQDS diffuses more rapidly than the movement of *S. oneidensis* cells on the surface or microcolonies expanding, thus increasing the bioavailability of Fe(III) (oxy)(hydr)oxides. This may explain the previously noted difference of the dependence on mineral surface area/identity between DIRB respiration and chemical reduction (Roden 2003). Additionally, this finding is consistent with previous studies indicating that the presence of AQDS or other electron shuttles increase the extent and rate of DIR (Jiang and Kappler 2008; Zachara et al. 1998).

3.5.3 Implications for Respiration Pathways of DIRB

Previously, *Shewanella oneidensis* MR-1 has been shown to be able to utilize all of the pathways that have been postulated for DIRB (see details in section1.7.2): (1) *S. oneidensis* MR-1 has evolved outer membrane-localized iron reductases, presumably

MtrC and OmcA to conduct direct contract pathway; (2) *S. oneidensis* MR-1 was also found to produce pilus-like, electrically conductive appendages in direct response to electron-acceptor limitation; (3) *S. oneidensis* MR-1 was found to release a quinone-related redox-active small molecule that may mediate the electron transfer between bacterial cells and Fe(III) (oxy)(hydr)oxides; (4) *S. oneidensis* MR-1 was found to produce organic ligands to form soluble organic-Fe(III) complexes and the this process was suggested to be a important intermediate step in DIR; (5) when *S. oneidensis* MR-1 was forced to use indirect pathways when exposed to Fe(III) (oxy)(hydr)oxides coated porous beads, electron shuttling pathway and organic ligand pathway may be used simultaneously. In this research, the heterogeneous dissolution morphology of Fe(III) (oxy)(hydr)oxides exposed to wild-type and its correlation with microcolony suggest two possibilities: (1) *S. oneidensis* MR-1 cells use either direct contact or nanowires pathway to respire on the Fe(III) particles beneath the adhered cells; since adhered cells form microcolonies on Fe(III) (oxy)(hydr)oxides, the resulting dissolution features would be correlated with the location and shape of microcolonies, and Fe(III) (oxy)(hydr)oxide coatings where no cells were adhered would remain the same after exposure; (2) *S. oneidensis* MR-1 produce electron shuttles and/or organic ligands to respire on Fe(III) (oxy)(hydr)oxides; however, these intermediates are trapped within microcolonies, otherwise homogenous dissolution morphology would be observed. *S. oneidensis* MR-1 cells trap the intermediates in microcolonies possibly for the purpose to reach a maximum efficiency of utilizing intermediates since their production causes energy. In addition, the observation of extracellular polycarbonate substrates (EPS) in this research supported this possibility since EPS can be used as the media to trap intermediates.

3.6 Conclusions

The dissolution morphology of Fe(III) (oxy)(hydr)oxides under various conditions was investigated. Fe(III) (oxy)(hydr)oxides exposed to the wild-type *S. oneidensis* MR-1 display a heterogeneous dissolution morphology that is correlated with microcolonies formed on the mineral surfaces. Fe(III) (oxy)(hydr)oxides exposed to a chemical reductant, AH_2DS, and the Δ*gspD* mutant or wild type *S. oneidensis* cells supplemented with AQDS display homogeneous dissolution morphologies. The difference in dissolution morphologies suggests that dissimilatory iron reduction is in part controlled by microcolony formation and possibly transport of bacterial cells on the mineral surfaces. The homogeneous dissolution of Fe(III) (oxy)(hydr)oxides exposed to the Δ*gspD* mutant and the wild type strain supplemented with AQDS indicates that electron shuttles increases the bioavailability of Fe(III) (oxy)(hydr)oxides by relieving the transport limitation of bacterial cells.

CHAPTER 4

ADHESION OF *SHEWANELLA ONEIDENSIS* MR-1 TO FE(III) (OXY)(HYDR)OXIDES: MICROCOLONY FORMATION AND ADHESION ISOTHERM

4.1 Abstract

The adhesion of dissimilatory iron reducing bacteria (DIRB) to Fe(III) (oxy)(hydr)oxides may play an important role in their respiration on ferric iron-containing minerals, but few quantitative surface cell density measurements have been made thus far. We used confocal microscopy to examine the adhesion of a common DIRB species, *Shewanella oneidensis* MR-1, onto Fe(III) (oxy)(hydr)oxides across a broad range of bulk (i.e., solution phase) cell densities from 10^5 cells/mL to 2×10^9 cells/mL. At bulk cell densities less than 1×10^7 cells/mL, cells adhered to the mineral surfaces formed an evenly distributed, homogeneous layer, while at the bulk cell densities higher than 2×10^8 cells/mL the adhered cells formed distinct microcolonies. Due to this complex adhesion behavior, simple Langmuir or Freundlich adsorption isotherms do not capture the relationship between the surface cell density and the bulk cell density over the entire range of bulk cell densities. Thus a new, two-step isotherm was developed that incorporated both isolated adhered cells at low cell densities as well as microcolonies at higher cell densities.

4.2 Introduction

Dissimilatory iron reducing bacteria (DIRB) are of interest partly because of their capacity to change the oxidation state, and hence the solubility and transport, of some metals such as iron and manganese (Lloyd 2003), chromium (Viamajala et al. 2002), uranium (Lovley et al. 1991a; Gorby and Lovley 1992; Wade and DiChristina 2000), technetium (Lloyd et al. 2000; Fredrickson et al. 2004; Payne and DiChristina 2006), and plutonium (Rusin et al. 1994). DIRB reduce these elements either by directly respiring on the metal as a terminal electron acceptor or indirectly by respiring on an alternate terminal electron acceptor (e.g., iron) that then acts as a chemical reductant for other species (Rusin et al. 1994; Fredrickson et al. 2004; DiChristina et al. 2005; Fredrickson et al. 2009). Of further interest is the capacity of DIRB to degrade hazardous chlorinated organic compounds (Petrovskis et al. 1994; Kazumi et al. 1995), aromatic compounds (Lovley et al. 1989; Lovley and Lonergan, 1990), and nitrates (Heijman et al. 1995; Klausen et al. 1995).

Adhesion of DIRB likely plays a role in facilitating their respiration on Fe(III) (oxy)(hydr)oxides (reviewed in Zhang et al. 2009). We previously showed evidence for this assertion by examining the dissolution morphology of Fe(III) (oxy)(hydr)oxides exposed to wild-type *Shewanella oneidensis* MR-1: we found that the dissolution morphology is heterogeneous and the size and shape of the dissolution features are consistent with the size and shape of microcolonies of bacterial cells observed on the mineral surfaces (Zhang et al. 2009). Further evidence for this is suggested by Bonneville et al. (2006) who predicted that DIRB respiration rate would be limited at high ratios of Fe(III) (oxy)(hydr)oxide colloids to DIRB cells due to a limited adsorption capacity of the colloids onto bacterial cells. However, thus far, quantitative measurements of the

adhesion density of DIRB cells are relatively few. In one study, surface cell densities of *S. oneidensis* MR-1 on hematite and magnetite surfaces under flow-through conditions were observed as a function of time using epifluorescence microscopy (Neal et al. 2003). Flow cytometry on bulk solutions has also been used to measure the number of *Shewanella alga* BrY cells before and after introduction of a crystalline Fe(III) oxide suspension, with the difference being interpreted as the number of adhered cells (Appenzeller et al. 2002). The relationship between the bulk, or solution-phase, cell density and the surface cell density was fitted with a Langmuir adsorption isotherm under bulk cell densities ranging from 10^6 to 10^8 cells/mL (Das and Caccavo 2001).

In this research, we used confocal microscopy and a cell viability dye to examine and quantify DIRB adhesion. Our *in situ* technique allows us to directly observe the spatial distribution of adhered *S. oneidensis* cells on Fe(III) (oxy)(hydr)oxides while ensuring cell viability. The relationship between the bulk cell density and the surface cell density was modeled across a wide range of bulk cell densities from 10^5 to 2×10^9 cells/mL. The advantage of our method is that surface cell densities are measured directly and thus spatial information about cell adhesion behavior (i.e., aggregation) is then incorporated into an adsorption isotherm that reflects the physical processes occurring at the mineral-water interface.

4.3 Experimental Section

4.3.1 Preparation of Fe(III) (Oxy)(hydr)oxides

Preparation and characterization of the Fe(III) (oxy)(hydr)oxide coatings on glass slides were the same as the method described in our recent article (Zhang et al. 2009).

Briefly, standard microscopy slides (75 × 25 mm) were cleaned by 30% H_2O_2 and etched by 5 M NaOH, then coated with Fe(III) (oxy)(hydr)oxide particles by slowly oxidizing 1 M $FeSO_4$ solution with 30% H_2O_2. The coated slides were heated to 90 ^oC in order to fix the particles to the slides and then cleaned by sonication. The resultant Fe(III) (oxy)(hydr)oxide coatings are strongly attached, uniform and dense, with an average particle diameter of approximately 0.5 μm (Zhang et al. 2009).

4.3.2 *Shewanella oneidensis* MR-1 Culture

S. oneidensis MR-1 cells were routinely cultured at 30 ^oC in Luria Broth (Luria and Burrous 1957). The cells were allowed to grow for 12 hours and were then harvested by centrifugation. The harvested cells were washed twice with a minimal salt medium (3.0 mM K_2HPO_4, 14 mM Na_2SO_4, 19 mM NH_4Cl, 1.0 mM $MgSO_4$, 0.1 mM $FeCl_2$, 0.5 mM $CaCl_2$, and 0.1% yeast extract) supplemented with 20 mM lactate at pH 7.5. Cells were subsequently resuspended in anaerobic medium to a final density of 2 x 10^9 cells/mL as determined by optical density measurements using a Shimadzu UV-1601 spectrophotometer at 600 nm (DiChristina 1989). To obtain a series of lower cell densities, the prepared cells were diluted with the salt media and actual densities after dilution were verified by spectrophotometry as above. To minimize oxygen contamination, all cultures and slides were kept in a model 1025/1029 Forma Anaerobic System (Thermo Electron), which contains a high purity anaerobic gas mixture of 10% hydrogen, 5% CO_2, and 85% N_2 (Airgas) and an active catalyst system to scrub incidental oxygen.

4.3.3 Slide Exposure

Fe(III) (oxy)(hydr)oxides were exposed to *S. oneidensis* MR-1 cells with fourteen different bulk cell densities ranging from 10^5 to 2×10^9 cells/mL. A 650-μL aliquot of the solution containing a known amount of bulk suspended bacterial cells was injected into a polycarbonate fluid cell affixed to an Fe(III) (oxy)(hydr)oxides coated glass slide. The approximate exposed slide area in this fluid cell was 0.79 cm^2. The surfaces between the fluid cell and the coated slide were sealed by an O-ring so that no solution leaked out of the fluid cell during exposure. The exposure was incubated for 24 hours in the anaerobic chamber at a constant temperature of 30 $^{\circ}$C. Fluid cells were covered to minimize evaporation. Each suite of fourteen different bulk cell density exposures was replicated three times on different slides for each exposure and each cell density giving a total of forty-two separate exposure experiments. Although each cell density was diluted by a fixed amount, actual bulk cell densities varied slightly. Additionally, some samples were not incubated, but prepared for imaging immediately in order to test whether the cells were alive and if they formed microcolonies in solution prior to exposure to Fe(III) (oxy)(hydr)oxides. To do this, 80 μL solution with suspended bacteria at bulk cell density of 2×10^9 cells/mL was injected onto a cleaned glass slide.

4.3.4 Confocal Microscopy and Image Analysis

After 24 hours exposure of Fe(III) (oxy)(hydr)oxides to *S. oneidensis* MR-1, the bacterial cells were stained with a dual staining, fluorescent dye (LIVE/DEAD® *Bac*Light™ Bacterial Viability Kit, Invitrogen). We have interpreted green-stained cells as alive and red-stained cells as dead using this kit. Viability dye was added to each fluid cell in the ratio of 3 μL dye to 1 mL solution. In order to allow for sufficient staining, cells were exposed to the dye for 15 minutes. Afterwards, most of the solution was

removed from the fluid cell by pipette, followed by removal of the clips and fluid cell from the coated slide, leaving a drop of stained solution in the middle of the coated slide. This process was conducted slowly and gently in order to minimize the disturbance to the adhered cells. The remaining solution was covered with a cover slip (22 × 22 mm), and the cover slip edges were carefully sealed by a thin layer of clear nail polish (nitrocellulose) that was allowed to dry for 30 minutes in order to maintain the anaerobic environment for the bacterial cells during imaging. Finally, slides were removed from the anaerobic chamber and imaged with the confocal microscope. Control experiments were conducted in the exact same way as described above, but clean, uncoated slides were used instead of the Fe(III) (oxy)(hydr)oxides coated slides.

Confocal microscopy was carried out using a Zeiss LSM 510 confocal laser scanning microscope (Carl Zeiss, Jena, Germany). Samples were imaged with a 63× objective and excited using a 543 nm Helium-Neon laser and a 488 nm Argon laser. For each replicate of each bulk cell density, five 146.25 × 146.25 μm images were taken from different areas of the sample surface. Cells adhered on the Fe(III) (oxy)(hydr)oxide surfaces and cells suspended in the solution were distinguished by using a relatively slow scan rate (2 Hz) and averaging up to 4 scans. Specifically, the adhered cells did not change position or orientation during each scan, whereas the floating or swimming cells drifted over the course of collecting a single image. The total number of adhered cells (both isolated and in colonies, alive and dead) was counted manually with the help of Image-J software (Image processing and analysis in Java, available at http://rsb.info.nih.gov/ij), and the data was further analyzed using the statistical software package R (The R project for statistical computing, available at http://www.r-project.org).

The number of cells on each image was counted and converted to a surface cell density in adhered cells per m^2 of Fe(III) (oxy)(hydr)oxide surface area.

4.4 Results and Discussion

4.4.1 Cell Adhesion Imaging and Microcolony Formation

The confocal microscopy images of Fe(III) (oxy)(hydr)oxides exposed to wild-type *S. oneidensis* MR-1 cells showed changes in the number of adhered cells as a function of the bulk cell density (Figure 17). At low bulk cell densities, the adhered cells were dispersed, forming what appeared to be a single layer (Figure 17a). In contrast, at high bulk cell densities aggregates of viable cells were observed, referred to here as microcolonies. In order to verify that aggregation behavior indeed changed as a function of the bulk cell density and was not simply a function of dilution, we tested the degree of uniformity in the spatial distribution of adhered cells using a two-dimensional Pearson's chi-squared aggregation test (Winkler and Hays 1975) (method discussed in Appendix A). This analysis indicated that, at a 95% confidence level, adhered cells were uniformly distributed at all bulk cell densities less than 1.1×10^7 cells/mL. When the bulk cell densities were larger than 1.8×10^8 cells/mL, cells were non-uniformly distributed at this confidence level for all images taken. The spatial distribution of adhered cells in the range between 1.1×10^7 and 1.8×10^8 cells/mL were aggregated in some images and uniformly distributed in others; thus we took this range as the uncertainty in the onset of microcolony formation. More than just aggregation, the number of organisms comprising a microcolony changed with the bulk cell density: microcolonies were found to be

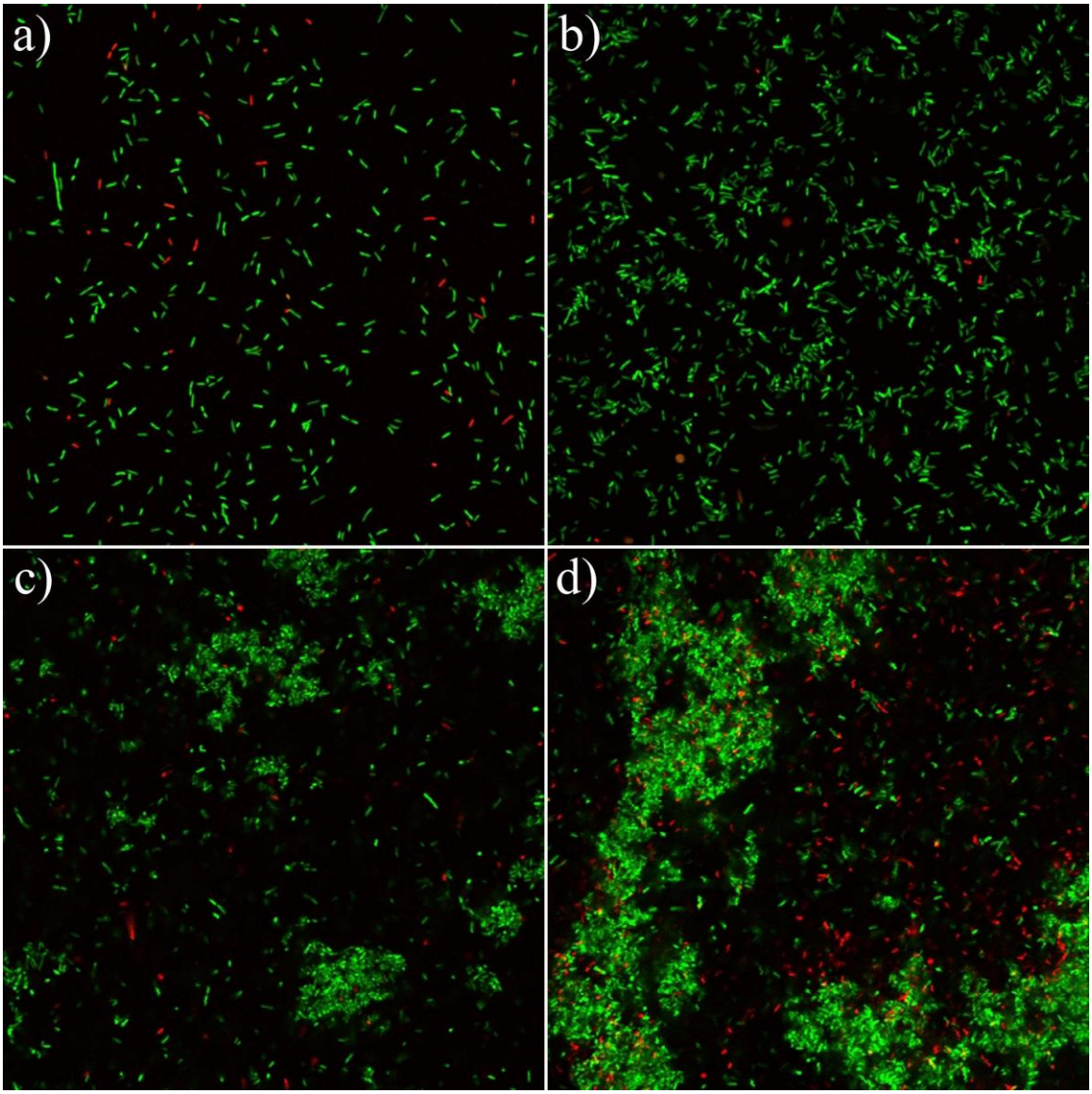

Figure 17: Selected confocal microscopy images of the spatial distribution of *S. oneidensis* MR-1 adhered to Fe(III) (oxy)(hydr)oxides after 1 day exposure. Cell densities are as follows: a) 7.30×10^7 cells/mL; b) 1.12×10^8 cells/mL; c) 8.38×10^8 cells/mL; d) 1.95×10^9 cells/mL. Microcolonies of organisms were observed at high bulk cell densities (c and d). Live cells were stained green, dead cells were stained red.

composed of less than one hundred cells at bulk cell densities in the range 1-5 $\times 10^8$ cells/mL, but microcolony size increased to thousands of cells at ~10^9 cells/mL bulk cell density. Finally, dead cells comprised less than 10% of the total number of adhered cells for all bulk cell densities, and dead cells were always distributed uniformly on the mineral surfaces without aggregation.

In contrast with the adhesion assays on Fe(III) (oxy)(hydr)oxides, adhered cells did not form microcolonies under any bulk cell densities on the coating-free control slides (Figure 18). When the bulk cell density was low (less than ~10^8 cells/mL), the spatial distribution of adhered cells on the control slides was similar to those on Fe(III) (oxy)(hydr)oxides; however, when the bulk cell density was high (larger than ~10^8 cells/mL), the adhered cells still covered the entire surface evenly. The Pearson's chi-squared aggregation test showed no aggregation at any bulk cell density at a 95% confidence level. Similarly, the exposure experiments after no incubation time exhibited a uniform distribution of cells and showed no microcolony formation. Furthermore, only a few cells were found adhered on the glass slides, in contrast with the images taken after 24 hours of exposure in both the DIR experiments and the control experiments at a bulk cell density of 2 $\times 10^9$ cells/mL (see Appendix A for figure). This result demonstrated that the cell aggregates shown in Figure 17 did not form in solution.

4.4.2 Quantitative Adhesion Measurements and Isotherm

Surface cell density as a function of bulk cell density for three replicate experiments is shown in Figure 19. At low bulk cell densities the number of adhered cells was small, but the surface cell density increased rapidly when the bulk cell density was in the range of 10^7-10^8 bulk cells/mL. Further increases in the bulk cell density above ~10^8

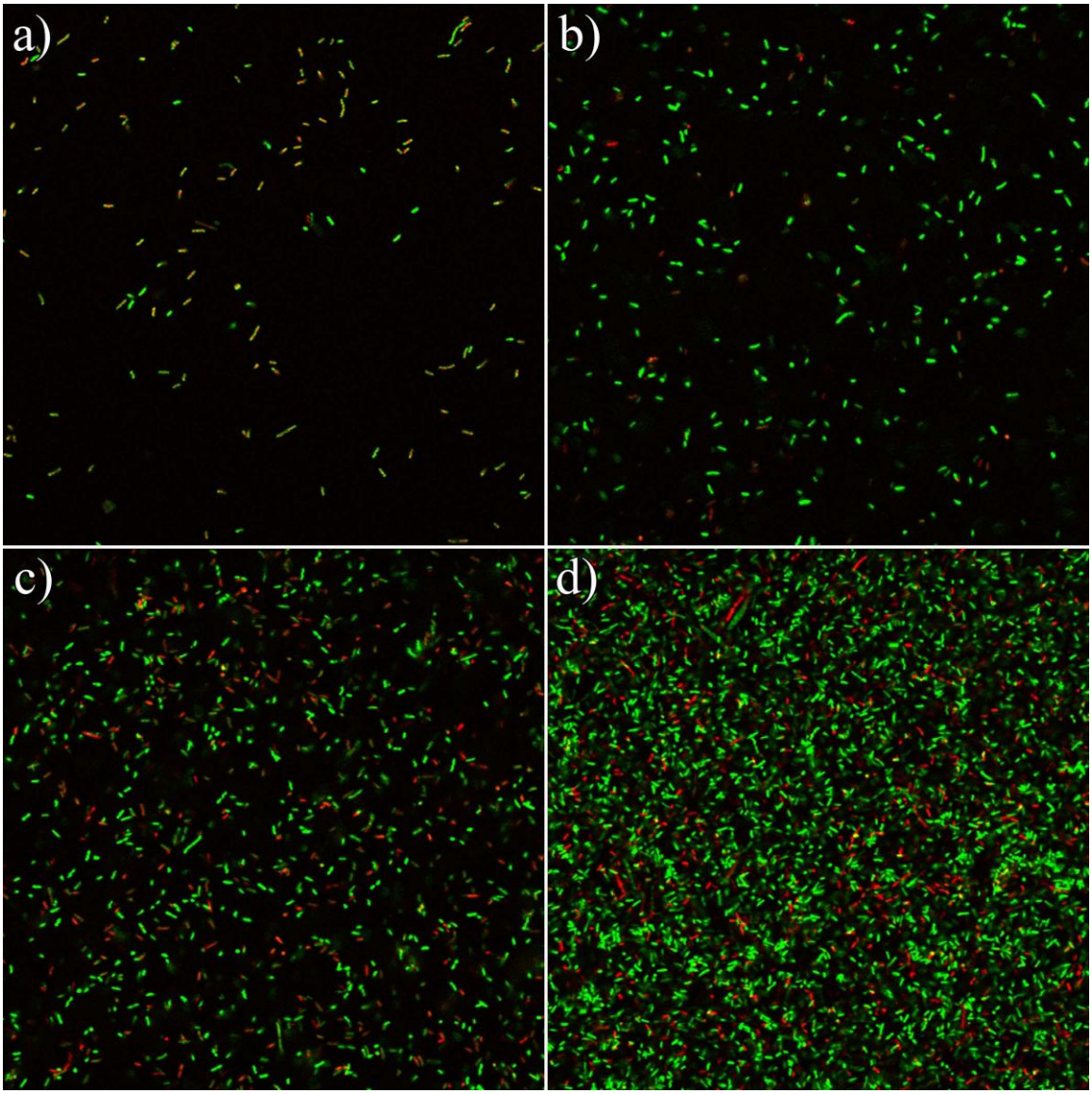

Figure 18: Selected confocal microscopy images of the spatial distribution of *S. oneidensis* MR-1 adhesion on uncoated glass slides after 1 day exposure with no additional electron acceptor. Cell densities are as follows: a) 1.27×10^7 cells/mL; b) 2.79×10^8 cells/mL; c) 5.58×10^8 cells/mL; d) 1.40×10^9 cells/mL. No microcolonies of organisms were observed. Live cells were stained green, dead cells were stained red.

cells/mL showed only small or no increases in the surface cell density. A studentized t-test applied to the adhesion data at high bulk cell densities confirmed this observation: at cell densities equal to or higher than 8.4×10^8 cells/mL, the slope of the data in figure 19a was zero at a 99% confidence level. The average surface cell density at the plateau was 0.077 ± 0.026 cells/μm^2, or one cell every 13 μm^2 of mineral surface area. Given that the bacterial cell cross-sectional area is on the order of 1-2 μm^2 (we measured an average of 1.29 μm^2), this plateau surface cell density is below what would be expected for closest-packed bacterial cells. However, this plateau surface cell density is much higher than previous measurements of surface cell densities, or ratios of bulk cells to mineral surface area where a maximum iron reduction rate is observed, which range from approximately one cell every 100-1500 μm^2 (Zhang et al. 2009). Surface cell densities for the control slides followed a similar pattern (data not shown), and reached a plateau surface cell density at the bulk cell density of 8.4×10^8 cells/mL at a 99% confidence interval. However, the plateau surface cell density was 0.13 ± 0.057 cells/μm^2, which was higher than that on Fe(III) (oxy)(hydr)oxides (confirmed by a studentized t-test).

One potential issue with the sampling method is that a microcolony is three dimensional in structure and that since our method only considered a two dimensional cross-section, this may lead to an underestimation of the adhered cell density. We considered this possibility during the imaging process, but in practice we did not observe microcolonies that were deeper than what could be captured within a single focal distance, i.e. a single image. An exposure time longer than the 24 hours used here, or an alternate electron acceptor may lead to the more pronounced biofilms observed previously for *Shewanella oneidensis* respiring on oxygen (Thormann et al. 2004). Additionally, a

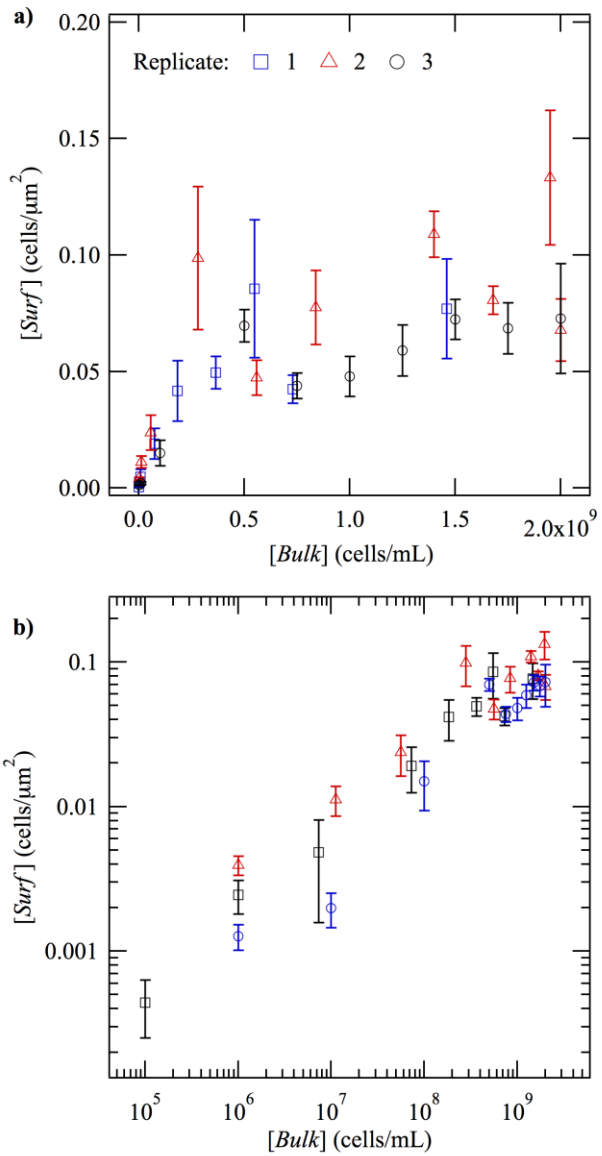

Figure 19: Measured surface cell densities. Each color represents the suite of exposures diluted from a given stock solution of bacterial cells in growth media and each data point represents the number of adhered cells in a single image. Data points are the mean surface cell density for a single exposed slide, error bars are ±1 standard deviation for observed cell densities within that slide. a) Surface cell density ([*Surf*]) as a function of bulk cell density ([*Bulk*]). The surface cell density reaches a plateau value of 0.077 cells/μm^2 at bulk cell densities of 8.4 × 10^8 cells/mL or higher. b) Log-log plot of a), emphasizing that the surface cell density at low bulk cell densities is non-zero. A change in surface cell density increase as a function of bulk cell density can be clearly seen at bulk cell densities greater than ~10^8 cells/mL.

systematic underestimation of surface cell densities here is unlikely since our measured surface cell densities are greater than previous estimates (Zhang et al. 2009).

Given the plateau in the surface cell density at high bulk densities, we first fit our results to the standard Langmuir and Freundlich adsorption isotherms. The primary difference between the two isotherms is that the Langmuir isotherm approaches a maximum capacity for adhesion as the bulk cell density increases whereas the Freundlich isotherm dictates slowing adhesion as a function of increased bulk cell densities. In the Langmuir model, the relationship between the bulk cell density and the surface cell density iss treated as:

$$[Bulk] + [Site] \overset{K_L}{\Leftrightarrow} [Surf] \quad (1)$$

where [*Bulk*] is the bulk cell density, [*Surf*] is the surface cell density (including isolated cells and cells in microcolonies), [*Site*] is the concentration of adhesion points on mineral surfaces for bacterial cells, and K_L is the affinity constant of a bacterial cell for the surface. Using [*Site*] is a contrivance since there are presumably no unique, fixed points for cellular adhesion on the mineral surfaces themselves at this scale, but it is valid because the plateau in the data suggests a limited adsorption capacity for cells whose magnitude could be defined as a number of empty sites. The well-known linearization of the isotherm is:

$$1/[Surf] = 1/(K_L[Surf_{max}][Bulk]) + 1/[Surf_{max}] \quad (2)$$

where [$Surf_{max}$] is the maximum surface cell density. If this model adequately describes the experimental data, then a plot of 1/[*Surf*] versus 1/[*Bulk*] will yield a straight line from which the model parameters K_L and [$Surf_{max}$] can be calculated from the slope and intercept. The following parameters were derived from the all inclusive fit in Figures 4a

and b: $[Surf_{max}] = 1.45 \times 10^{-2}$ cells/μm^2, $[K_L] = 2.59 \times 10^{-7}$ mL/cell (Table 2). A non-linear goodness of fit statistic applied to this data was $\chi^2 = 26.99$ (definition is shown in Appendix A). The model fit shown in Figure 20c (red line) immediately shows a problem with the fit: the isotherm models the data well at low bulk cell densities but becomes totally inappropriate at high bulk cell densities. This is an artifact introduced by the fitting routine; the best-fit shown in the linearization (Figure 20a, red line) is biased by the lowest cell density data at 10×10^{-6} mL/cell (right side of Figure 20a). If the data is fit only to bulk cell densities larger than 10^8 cells/mL, the resulting fit was much better (Figure 20, blue line) with $[Surf_{max}] = 7.19 \times 10^{-2}$ cells/μm^2, $[K_L] = 8.30 \times 10^{-9}$ mL/cell, and $\chi^2 = 1.49$. This new fit, however, fails to model well surface cell densities at low bulk cell densities (Figure 20a). The failure of the Langmuir isotherm to obtain a good fit over the entire range of bulk cell densities is likely due to the aggregation behavior of the adhered cells discussed above.

An alternate commonly used adsorption isotherm is the Freundlich model, wherein the relationship between the bulk cell density and the surface cell density is as follows:

$$n[Bulk] \overset{K_F}{\Leftrightarrow} [Surf] \tag{3}$$

where [*Surf*] and [*Bulk*] stand for surface cell density and bulk cell density as mentioned above, and K_F and n are constants. The Freundlich isotherm is linearized as:

$$\log[Surf] = \log K_F + n \log[Bulk] \tag{4}$$

The best-fit linearized adsorption isotherm is shown in Figure 21a. The following model parameters were derived: $K_F = 1.31 \times 10^{-6}$, $n = 0.52$ (Table 2), and the non-linear goodness of fit statistic was $\chi^2 = 1.70$. The Freundlich model more adequately fits the

Table 2: Isotherm model comparison: Parameters and χ^2.

Langmuir, entire data set	$[Surf_{max}] = 1.45 \times 10^{-2}$ cells/μm^2 $K_L = 2.59 \times 10^{-7}$ mL/cells $\chi^2 = 26.99$
Langmuir, high cell densities only	$[Surf_{max}] = 7.19 \times 10^{-2}$ cells/μm^2 $K_L = 8.30 \times 10^{-9}$ mL/cells $\chi^2 = 1.49$
Freundlich	$K_F = 1.36 \times 10^{-6}$ $n = 0.52$ $\chi^2 = 1.70$
Two-step	$[Surf_{max}] = 3.35 \times 10^{-3}$ cells/μm^2 $K_a = 1.26 \times 10^{-6}$ mL/cells $K_c = 1.74 \times 10^{295}$ $n = 119.77$ $\chi^2 = 1.29$

entire range of the data which makes it more attractive than the Langmuir adsorption isotherm, even though the goodness-of-fit statistic is slightly higher (=poorer fit) (Figure 21b). The Freundlich model underestimates the surface cell density when the bulk cell density is between 1×10^8 cells/mL and 5×10^8 cells/mL (Figure 21b), and overestimates (on average) the number of adhered cells at high bulk cell densities. More serious is that the isotherm does not predict a plateau in the number of adhered cells at high bulk cell densities which is discussed above, but the functional form of the isotherm is such that the surface cell density always increases with the increased bulk cell density. Thus the Freundlich isotherm, while roughly fitting the entire data set, does not capture an essential aspect of the adhesion behavior of these organisms.

Considering that neither the simple Langmuir adsorption isotherm nor the Freundlich adsorption isotherm is completely satisfactory, we developed and applied a

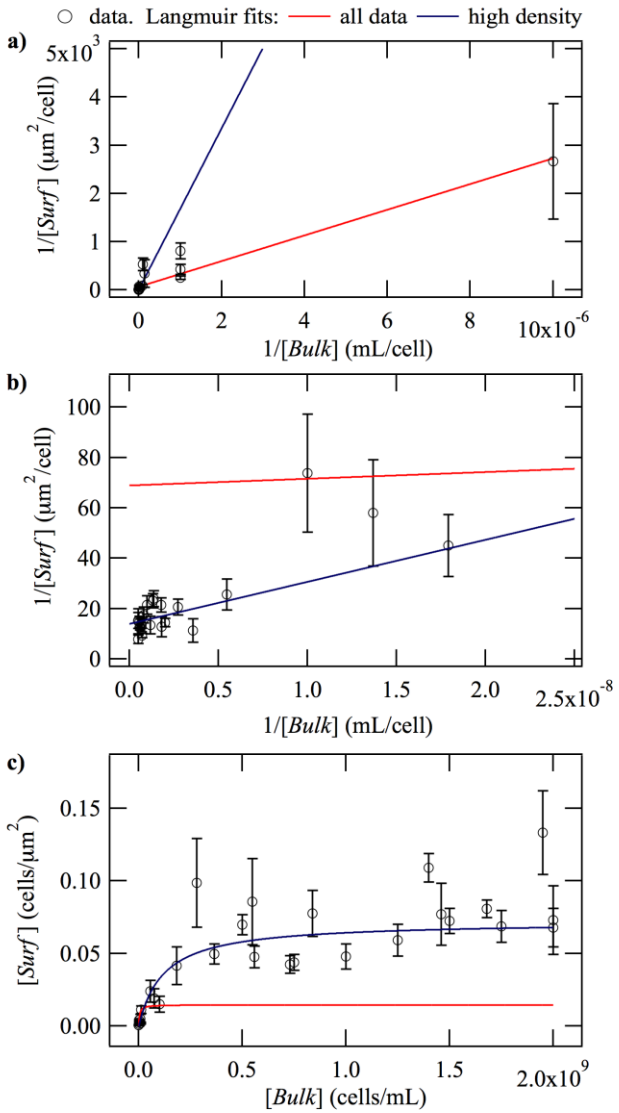

Figure 20: Langmuir adsorption isotherm linearization and fits. Data points are the mean surface cell density for a single exposed slide, error bars are ±1 standard deviation for observed cell densities within that slide. The red lines represent the fit to the entire data set, the blue lines are a fit excluding bulk cell densities below 10^8 cells/mL. a) Linearization plot, reciprocal cell density as a function of reciprocal bulk cell density. The high density only fit (blue line) does not model the low density data on the right side of the plot well. b) Same linearization plot, but only showing the high bulk cell densities. The fit for the entire data set (red line) does not describe the high bulk cell densities well. c) Surface cell density as a function of bulk cell density and the resultant fits.

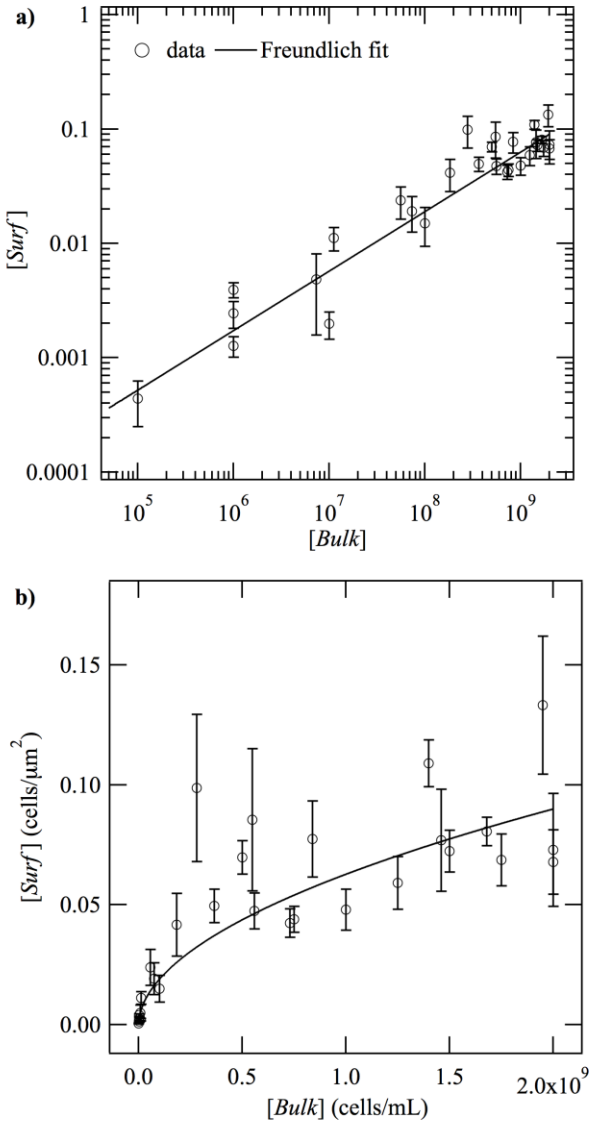

Figure 21: Freundlich adsorption isotherm and fit. Data points are the mean surface cell density for a single exposed slide, error bars are ± 1 standard deviation for observed cell densities within that slide. a) Linearization plot, the log of surface cell density as a function of the log of bulk cell density. b) The surface cell density as a function of the bulk cell density and the resultant fit. The Freundlich fit underestimates the surface cell density between bulk cell densities between 1×10^8 and 5×10^8 cells/mL and shows no plateau at high bulk cell densities.

new model. The conceptual framework for the model is as follows: (1) cells adhere independently from solution to the mineral surfaces forming a single layer that follows the Langmuir adsorption isotherm, and (2) adhered cells aggregate to form microcolonies whose concentration increases as the number of isolated adhered cells increases. These processes are described by the following reactions:

$$[Bulk] + [Site] \overset{K_a}{\Leftrightarrow} [Surf_{isol}] \quad (5)$$

$$n[Surf_{isol}] \overset{K_c}{\Leftrightarrow} [Surf_{col}] \quad (6)$$

where [*Bulk*] still stands for the bulk cell density, [*Site*] is the density of surface empty sites, [$Surf_{isol}$] is surface density of isolated, unaggregated cells, and K_a is the equilibrium constant for adhesion. In equation 6, [$Surf_{Col}$] is the surface density of cells contained in microcolonies, K_c is the equilibrium constant for microcolony formation, and n is a constant. The central hypothesis of the microcolony formation step is that microcolonies form from previously adhered cells, not from cells in solution. This is justified by the lack of microcolony formation, yet greater plateau surface cell density, in the control experiments (Figure 18) than the DIR experiments (Figure 17). That is, the aggregation of cells does not appear to be increasing the total surface cell density and equation 6 is written in such a way as to try and capture this phenomenon.

An alternate hypothesis is that microcolony formation is driven by replication of cells adhered to the surface. If microcolony formation were dominantly driven by cell replication on this time-scale (1 day), one might expect small microcolonies at low bulk cell densities. As noted above, the size of microcolonies does increase with cell density (compare Figures 1c and 1d), but no statistically significant aggregation is observed at low bulk cell densities (Figures 1a and 1b). Regardless of mechanism, since our data is

only for a single point in time (for time = 0, see Appendix A), the kinetics of cell replication are not considered in this model.

One complication of using this isotherm is that additional fit parameters are introduced from the simple Langmuir or Freundlich isotherms, and thus multiple solutions are possible. However, as established above, cellular aggregation is negligible at bulk cell densities less than 1.1×10^{7} cells/mL and thus the fit parameters for equation 5 can be determined independently using a Langmuir isotherm linearization on data solely from low bulk cell densities:

$$1/[Surf_{isol}] = 1/(K_a[Surf_{max}][Bulk]) + 1/[Surf_{max}] \quad (7)$$

The resulting $[Surf_{max}]$ and K_a were 3.35×10^{-3} cells/μm^2 and 1.26×10^{-6} mL/cell, respectively (Table 2). Similarly, under conditions where cellular aggregation is ubiquitous (bulk cell densities larger than 1.83×10^{8} cells/mL), a linearized form of the Freundlich adsorption isotherm was used to model equation 6, as follows:

$$\log[Surf_{col}] = n \log[Surf_{isol}] + \log K_c \quad (8)$$

where $[Surf_{isol}]$ was calculated based on the Langmuir adsorption isotherm shown in equation 7. The resulting K_c and n were 1.74×10^{295} and 119.77, respectively (Table 2). A log-log plot and fit of the complete isotherm are shown in Figure 22; the isotherm captures characteristics of the data set remarkably well. The non-linear goodness-of-fit statistic in this case was $\chi^2 = 1.29$, which is not the best fit it is possible to obtain with this isotherm, but the best fit that is reasonably unique. Finally, an important parameter derived from the model is the critical density for microcolony formation, which we will interpret as the bulk cell density where 50% of the adhered cells are present as microcolonies: 3.03×10^{7} cells/mL. As expected, this number falls within the range of

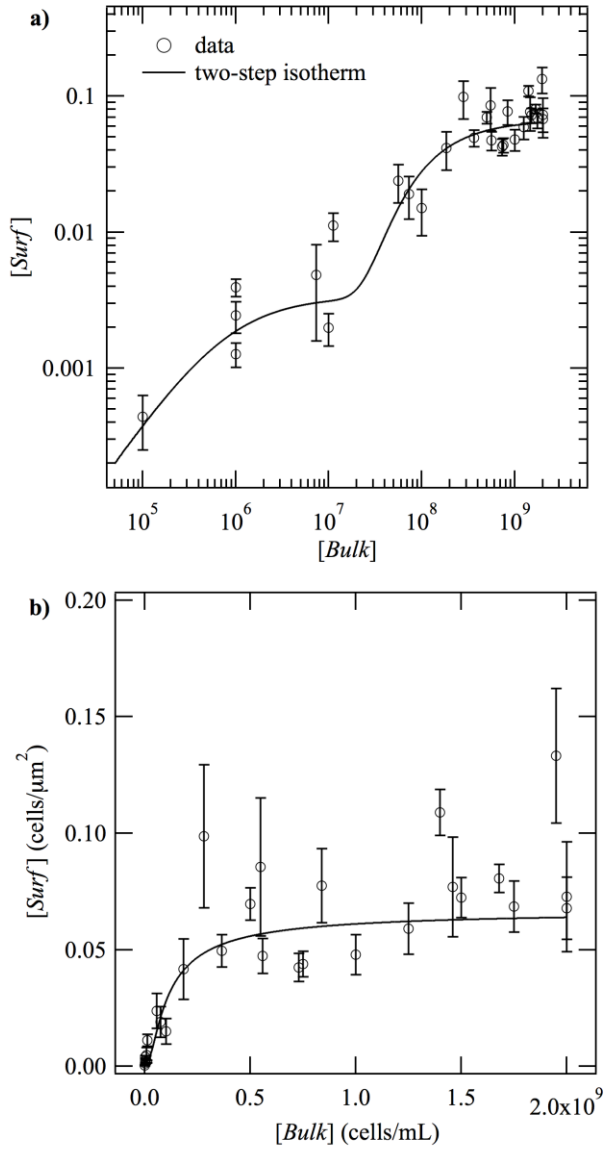

Figure 22: Two-step adsorption isotherm. Data points are the mean surface cell density for a single exposed slide, error bars are ± 1 standard deviation for observed cell densities within that slide. a) A log-log plot of the surface cell density as a function of bulk cell density. The new adsorption isotherm captures the plateau in the surface cell density at high bulk cell densities and shows the transition between isolated adhered cells and microcolony formation at 3.03×10^7 cells/mL. b) The surface cell density as a function of the bulk cell density.

1.12×10^7 to 1.83×10^8 cells/mL where the uniformity of the spatial distribution of adhered cells is mixed at a 95% confidence level. Ultimately, we regard the two-step model as capturing the essence of cell adhesion on Fe(III) (oxy)(hydr)oxides as a function of bulk cell densities despite the larger number of fit parameters and substantial experimental uncertainty.

4.4.3 Implications for Respiration Kinetics of DIRB

We already showed a correlation between microcolony size and character and the dissolution morphology of Fe(III) (oxy)(hydr)oxides in Chapter 3. Here we have shown that microcolony formation does not occur at all bulk cell densities, but requires a critical bulk cell density before cells begin to aggregate. These studies together suggest that bulk cell densities may affect DIR rate in a non-linear way. This hypothesis is supported by the study of Roden (Roden 2003), who shows that the initial DIR rates of *Shewanella putrefaciens* CN32 as a function of bulk cell densities up to 2×10^9 cells/mL is hyperbolic. The initial DIR rate is found to saturate at a bulk cell density of 5×10^8 cells/mL (Roden 2003), which is similar to the bulk cell density at which surface cell density saturates, 8.4 x 10^8 cells/mL (especially considering Roden, 2003 only tested five different bulk cell densities). The similarity between these two values suggests that the surface cell density may control in part the initial DIR rate. Further development on a DIR rate model to reflect the surface cell density is recommended.

CHAPTER 5

CONCLUSIONS

This research visually and quantitatively studied the interaction between *Shewanella oneidensis* MR-1 and Fe(III) (oxy)(hydr)oxides in dissimilatory iron reduction. Section 5.1 and 5.2 conclude the findings of this research, and section 5.3 and 5.4 conclude the implication of these findings to the mechanism(s) and kinetics of DIR. Section 5.5 suggests further study to explore DIR.

5.1 Dissolution Morphology of Fe(III) (Oxy)(hydr)oxides

The dissolution morphology of Fe(III) (oxy)(hydr)oxides is heterogeneous when exposed to the wild-type *S. oneidensis* MR-1, and homogeneous when exposed to a chemical reductant. The wild-type cells generate dissolution patches on the mineral surfaces which range from 6 to 86 μm in the length of the longest axis, and the Fe(III) (oxy)(hydr)oxides within the patches are completely dissolved whereas no obvious dissolution is observed outside the patches; the shape and size of dissolution patches are consistent with the microcolonies formed on the mineral surfaces. In contrast, the chemical reductant dissolves Fe(III) (oxy)(hydr)oxides uniformly, with all the Fe(III) (oxy)(hydr)oxide particles dissolving at the same pace. When an exogenous electron shuttle is added, both the wild-type and mutant of *S. oneidensis* MR-1 generate homogeneous dissolution morphology of Fe(III) (oxy)(hydr)oxides.

5.2 Adhesion of *Shewanella oneidensis* MR-1

The *S. oneidensis* MR-1 cells adhered to the surfaces of Fe(III) (oxy)(hydr)oxides form an evenly distributed monolayer at low bulk cell densities and aggregate to form microcolonies at high bulk cell densities. A two-dimensional Pearson's chi-squared aggregation test suggests that adhered cells are evenly distributed at bulk cell densities less than 1×10^7 cells/mL, whereas they form microcolonies at bulk cell densities higher than 2×10^8 cells/mL. When *S. oneidensis* MR-1 cells are exposed to glass surfaces without Fe(III) minerals, no microcolonies are observed under any bulk cell densities.

The relationship between the surface cell density and the bulk cell density is modeled. Langmuir isotherm cannot model the relationship at the entire range of the bulk cell densities. Freundlich isotherm underestimates the surface cell density when the bulk cell density is between 1-5 $\times 10^8$ cells/mL, overestimates the surface cell density at high bulk cell densities, and more seriously, cannot predict a plateau. Thus a new two-step adsorption isotherm is developed by assuming: cells in solution independently adhere to the mineral surfaces to form isolated surface cells, which follows the Langmuir isotherm; then the isolated surface cells aggregate to form microcolonies, which follows the Freundlich isotherm. Both the fitting plot and the non-linear goodness-of-fit test suggest that the new model is able to capture the complex adhesion behavior of *S. oneidensis* MR-1 on Fe(III) (oxy)(hydr)oxides.

5.3 Implications for the Mechanisms of Dissimilatory Iron Reduction

The comparison of the dissolution morphology of Fe(III) (oxy)(hydr)oxides exposed to *S. oneidensis* MR-1 and a chemical reductant suggests that the transport of bacterial cells is limited during DIR. The limitation is not from the transport of cells in solution; instead, it is from the transport of cells on the mineral surfaces and/or the rate of

microcolony formation. Furthermore, the addition of an exogenous electron shuttle relieves this limitation, by allowing the cells to use an indirect electron shuttling pathway.

The heterogeneous dissolution morphology of Fe(III) (oxy)(hydr)oxides exposed to wild-type *S. oneidensis* MR-1 may suggest two possible pathways: (1) *S. oneidensis* MR-1 cells use either direct contact or nanowires pathway to respire on the Fe(III) particles beneath the adhered cells; (2) *S. oneidensis* MR-1 produce electron shuttles and/or organic ligands to respire on Fe(III) (oxy)(hydr)oxides; however, these intermediates are trapped within microcolonies to reach a maximum efficiency of utilizing these intermediates.

5.4 Implications for the Kinetics of Dissimilatory Iron Reduction

The observation of different cell adhesion patterns at low and high bulk cell densities suggests that surface cell density may in part control the rates of dissimilatory iron reduction. Therefore, a kinetics model based on the surface cell density may be more accurate to describe and predict DIR rates. Furthermore, by indicating the significance of surface cell density, this research suggests that when applying DIRB in bioremediation, to increase the efficiency, it is more important to increase the surface cell density than the bulk cell density.

5.5 Further Study

5.5.1 Further Study for Mechanisms of Dissimilatory Iron Reduction

This research can better elucidate the mechanisms of dissimilatory iron reduction with addition of extra experiments. Currently, the dissolution morphology of Fe(III) (oxy)(hydr)oxides exposed to wild-type at high bulk cell density was observed and is

found to correlate with microcolony which only forms at high bulk cell densities; since the adhered cells are uniformly distributed on the mineral surfaces at low bulk cell densities, it is interesting to observe the dissolution morphology of Fe(III) (oxy)(hydr)oxides at a low bulk cell density. Besides observing dissolution morphology, it is important to measure the amount of soluble organic-Fe(III) complexes and potential electron shuttles such as flavins and quinine-type compounds at both high and low bulk cell densities. The detection of these intermediates may support the hypothesis that wild-type cells form microcolonies to trap the intermediates to reach a maximum efficiency of utilizing the intermediates. For the wild-type exposure experiment at high bulk cell density, it will be more interesting to compare the upper layer of the bacterial solution where no microcolony will be found to a well mixed bacterial solution where intermediates are forced to mix in the solution. If significant difference on the amount of intermediates is detected, this result can further support the idea that intermediates are trapped in microcolonies. In addition, since the adhered cells are found isolated on the mineral surfaces at low bulk cell density, it is a good idea to observe whether nanowires form. Finally, when Fe(III) (oxy)(hydr)oxides were exposed to Δ*gspD* mutant with the electron shuttle AQDS, 0.5 mM AQDS was used which is much higher than the amount of total dissolved iron measured after exposure (240 ± 31 μM); this led to a situation that Δ*gspD* mutant uses AQDS as the electron acceptor instead of Fe(III) (oxy)(hydr)oxides. Therefore, it is necessary to decrease the concentration of AQDS. Since it is not clear which concentration of AQDS is low enough to enable the electron shuttling pathway, a decreased series of AQDS concentrations can be tested to detect whether the dissolution morphology of Fe(III) (oxy)(hydr)oxides changes with AQDS concentrations.

Further improvement can be achieved by testing other mutants and Fe(III) (oxy)(hydr)oxides. For example, the dissolution morphology of Fe(III) (oxy)(hydr)oxides exposed to a Fe(III) adhesion-deficient mutant SO3800 is worth studying with atomic force microscope (Burns et al. 2010). Since the mutant SO3800 is severely impaired in its ability to adhere to Fe(III) (oxy)(hydr)oxides, yet retained wild-type Fe(III) respiratory ability, it may utilize indirect pathways; therefore, it is interesting to measure the amount of soluble organic-Fe(III) complexes and potential electron shuttles. For Fe(III) (oxy)(hydr)oxides, the one used in this research is possibly 2-line ferrihydrite which is rather amorphous. Since the characteristics of Fe(III) (oxy)(hydr)oxides has long been suggested to affect dissimilatory iron reduction, it is interesting to test the whole suite of experiments on more crystalline Fe(III) minerals such as hematite and goethite to detect whether there will be changes for reaction pathway, regimes, and kinetics.

5.5.2 Further Study for Kinetics of Dissimilatory Iron Reduction

To further improve our understanding of how surface cell density control kinetics of dissimilatory iron reduction, one field of research that can be explored is the relationship between the DIR rate and the surface cell density. In Chapter 4, we have shown the similarity between the curve of DIR rates as a function of the bulk cell density and the curve of the surface cell density as a function of the bulk cell density. Additionally, the bulk cell density where DIR rates were observed to saturate is similar to that where we observed the surface cell density to saturate. Therefore, we hypothesize that the initial rate of DIR is correlated with the surface cell density, and most likely, is in a linear relationship. If the linear relationship is confirmed, it not only indicates a direct control of the surface cell density to DIR rates, but also facilitates us to build kinetics

model to describe and predict DIR rates, since the relationship between the bulk cell density and the surface cell density has been modeled in this research.

APPENDIX A

SUPPLEMENTARY INFORMATION

A.1 Pearson's Chi-Squared Statistic

Each image was subdivided into uniform grids whose size was determined such that the number of cells in each grid-cell was greater than five in order to ensure statistically significant sampling. Since the number of adhered cells changes as a function of bulk cell density, the number of subdivisions necessary also changes: for bulk cell densities less than 1.83×10^8 cells/mL, each image was subdivided into 4×4 grid cells, and for higher cell densities 8×8 grid cells were used. The test statistic for each image was calculated as follows:

$$x = \sum_{i=1}^{n} \sum_{j=1}^{n} \frac{(O_{ij} - E_{ij})^2}{E_{ij}} \tag{A1}$$

$$E_{ij} = \frac{N}{n} \tag{A2}$$

where O_{ij} is the number of observed bacterial cells in each grid cell, E_{ij} is the number of bacterial cells which would be expected in each grid cell if the bacterial cells were distributed uniformly, x is the test statistic for the chi-squared distribution ($\chi^2_{(n-1)}$), N is the total number of adhered cells in an image, and n is the number of grid cells. If the test statistic is higher than the critical value for the chi-squared distribution at the desired level of significance, the bacterial cells are aggregated (i.e., a rejection of the null hypothesis). Strictly speaking, the opposite result does not necessarily prove that the cells

are uniformly distributed (i.e., a failure to reject the null hypothesis does not prove the null hypothesis), but in practice there is little gained by making the distinction so we will assume that the cells are uniformly distributed.

A.2 Non-linear Goodness of Fit Statistic

A non-linear goodness of fit statistic was calculated by the following equation:

$$\chi^2 = \sum_{i=1}^{n} \frac{(O_i - P_i)^2}{P_i} \tag{A3}$$

Where O_i is the observed surface cell density, P_i is the predicted surface cell density, and n is the total number of observed surface cell densities.

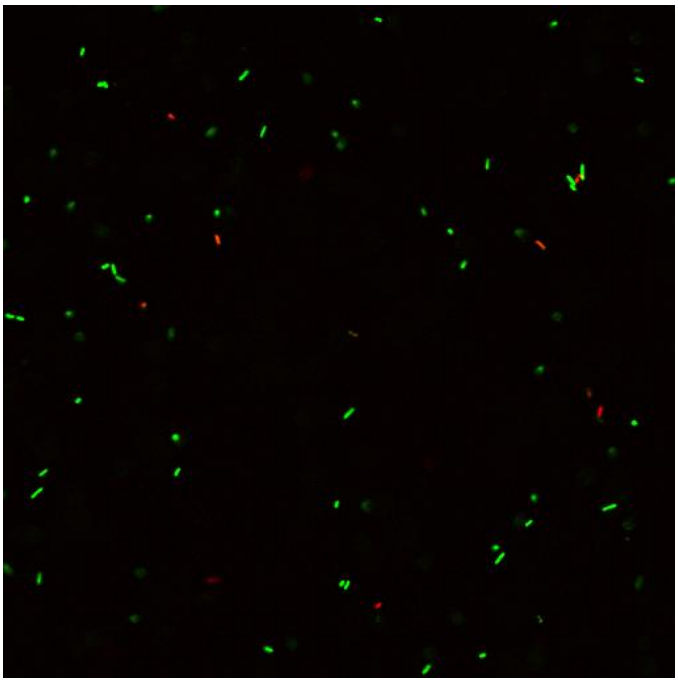

Figure A1: Selected confocal microscopy image of the spatial distribution of *S. oneidensis* MR-1 adhered to Fe(III) (oxy)(hydr)oxides after 0 hours exposure. Bulk cell density is 2.0×10^9 cells/mL. Live cells were stained green, dead cells were stained red. Very few attached cells are observed, in contrast to the 24 hour exposure.

APPENDIX B

MONOD KINETICS AND MICHAELIS-MENTEN KINETICS

B.1 Monod Kinetics

The abundance of substrate affects microbial growth, and under the condition of limited substrate the Monod equation was developed to model the kinetics of microbial growth. The Monod equation is empirical and the relationship between growth rate and substrate is described as follows:

$$\mu = \frac{\mu_{max}[S]}{K_S + [S]} \tag{B1}$$

where μ is the specific growth rate at the substrate concentration [S], μ_{max} is the maximum growth rate which can be reached under sufficient substrate, and K_S is the half saturation constant (Pert 1994). When $[S] << K_S$, $\mu = \mu_{max}[S]/K_S$, which means μ is linear with [S]. When $[S] = K_S$, $\mu = 0.5\mu_{max}$, and this is why K_S is named the half saturation constant. When $[S] >> K_S$, $\mu \approx \mu_{max}$, and the growth rate reaches the maximum. Equation (B1) can be linearized to the following equation:

$$\frac{1}{\mu} = \frac{K_S}{\mu_{max}} \times \frac{1}{[S]} + \frac{1}{\mu_{max}} \tag{B2}$$

In this way, K_S and μ_{max} can be determined based on experimental data.

B.2 Michaelis-Menten Kinetics

The Michaelis-Menten equation is commonly used to model the kinetics of enzyme-catalyzed substrate reactions, and describes the relationship between initial reaction rate and substrate concentration, as follows:

$$v_0 = \frac{v_{\max}[S]}{K_M + [S]} \tag{B3}$$

where v_0 is the initial reaction rate at the substrate concentration [S], v_{max} is the maximum initial reaction rate, and K_M is the half saturation constant (Roberts 1977). When $[S] << K_M$, $v_0 = v_{max}[S]/K_M$, which means v_0 is linear with [S]. When $[S] = K_M$, $v_0 = 0.5 v_{max}$, and this is why K_M is named the half saturation constant. When $[S] >> K_M$, $v_0 \approx v_{max,}$ and the initial reaction rate reaches the maximum. Equation (B3) can also be linearized in the same way as Monod equation to determine K_M and μ_{max}.

Unlike the Monod equation, the Michaelis-Menten equation has mechanistic basis, and the derivation rests on two key assumptions: (1) the total enzyme concentration does not change over time; (2) the concentration of intermediate complex stays the same over time. The derivation of the Michaelis-Menten equation is based on the following reaction:

$$E + S \underset{k_{-1}}{\overset{k_1}{\rightleftarrows}} ES \xrightarrow{k_2} E + P \tag{B4}$$

where E is the enzyme, S is the substrate, ES is the intermediate complex, P is the product, and k_1, k_{-1} and k_2 are the rate constants. In this reaction, the second step is irreversible, and the product does not bind to the enzyme. Based on reaction (B4), we can derive the following rate expressions:

$$\frac{d[ES]}{dt} = k_1[E][S] - [ES](k_{-1} + k_2) \equiv 0 \tag{B5}$$

$$\frac{d[P]}{dt} = k_2[ES] \tag{B6}$$

The conclusion that the rate of ES is equal to zero is based on the second assumption that ES does not change over time. In addition, the first assumption can lead to the following conclusion:

$$[E]_0 = [E] + [ES] \equiv const. \tag{B7}$$

where $[E]_0$ is the total enzyme concentration. Combining equation (B5), (B6), and (B7), we can derive the following equation about [ES]:

$$[ES] = \frac{[S][E]_0}{K_M + S} \tag{B8}$$

where K_M is calculated as follows:

$$K_M = \frac{k_{-1} + k_2}{k_1} \tag{B9}$$

So the Michaelis-Menten equation can be derived:

$$v_0 = \frac{d[P]}{dt} = k_2[ES] = v_{\max} \frac{[S]}{K_M + [S]} \tag{B10}$$

where $v_{\max} = k_2[E]_0$.

The similarity between the michaelis-menten equation and the monod equation is not a coincidence. The monod equation may be derived on the hypothesis that the substrate uptake enzyme is the bottleneck in the metabolism.

APPENDIX C

PROTEOBACTERIA SUBDIVISIONS AND PHYLOGENETIC TREE

C.1 Definition and Evolution of Subdivisions of *Proteobacteria*

Proteobacteria has six subdivisions (alpha, beta, gamma, delta, epsilon and zeta) to date. These subdivisions are rather diversified, and cannot be distinguished by characteristics such as photosynthetic or nonphotosynthetic, and aerobic or anaerobic. Instead, these subdivisions are defined and distinguished on the basis of 16S rRNA sequence similarities (Stackebrandt et al. 1988). Take subdivisions alpha, beta, gamma, and delta as an example, it has been suggested that two helices in 16S rRNA, positions 184 to 193 and 198 to 219, help to divide the four subdivisions (Woese 1987). The structure of these helices in species from these four subdivisions is shown in Figure C1. The first helix, positions 184 to 193, contains 3 base pairs in alpha, beta, and gamma subdivisions, but 10 base pairs in delta subdivision; therefore, delta subdivision can be identified. Similarly, the second helix, positions 198 to 219, contains approximately 8 base pairs in beta, gamma, and delta subdivisions, but 2 base pairs in alpha subdivision; therefore, alpha subdivision can be identified. More comprehensive 16S rRNA sequence comparison defines the belonging of each species.

The subdivisions of *Proteobacteria* have been suggested to have evolved in the following sequence: epsilon and delta → alpha → beta → gamma (Gupta 2000); however, a certain species in epsilon subdivision can evolve later than a certain species in gamma subdivision even though epsilon subdivision evolved earlier.

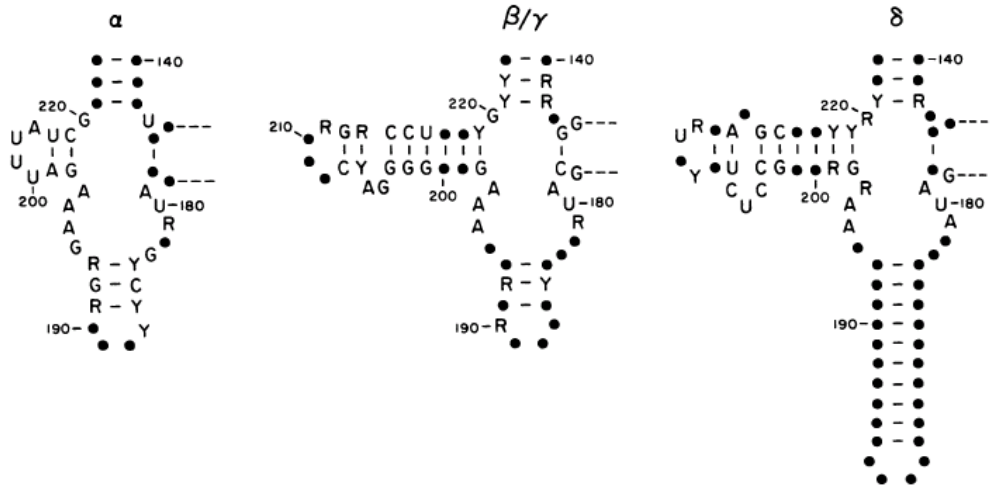

Figure C1: Structural detail of 16S rRNA between positions 180 and 220 for alpha, beta, gamma and delta subdivisions of *Proteobacteria*. Composition of a position is given when highly conserved within a subdivision; otherwise it is shown as a dot. Base pairs with connecting lines were also indicated (Woese 1987).

C.2 Brief Introduction of Phylogenetic Tree

A phylogenetic tree is a tree-shaped diagram showing the evolutionary relationships among various biological species (Maddison and Schulz 2007). Figure C2 is a simple example to explain the major components of a phylogenetic tree and how to interpret a phylogenetic tree. As listed in Figure C2, "root" is the stem that connects the phylogenetic tree to the ancestor of the whole tree; "branch" describes an evolutionary lineage from the root; "taxon" (plural taxa) means a group of organisms and "terminal taxon" means a group at the tip of a tree branch, like leaves; "node" is a branching point which represents the common ancestor of the lineages descending from this branching point. This figure represents the basic structure of a rooted phylogenetic tree. Another type of phylogenetic tree is unrooted, with an outgroup replacing the root. Outgroup means a taxon that has a relative further evolutionary relationship than the species in the

group, and is included to provide information about how closely these ingroup species are related. Figure 4 in Chapter 1 is an example of unrooted phylogenetic tree.

A phylogenetic tree not only indicates the evolutionary relationships among different species, but also represents the quantitative evolutionary distance among species by the length of branches. The length of the branch can either represents evolutionary time, or extent of character or genetic change among species. For example, the length of branches in Figure 4 corresponds to the difference of 16S rRNA sequence.

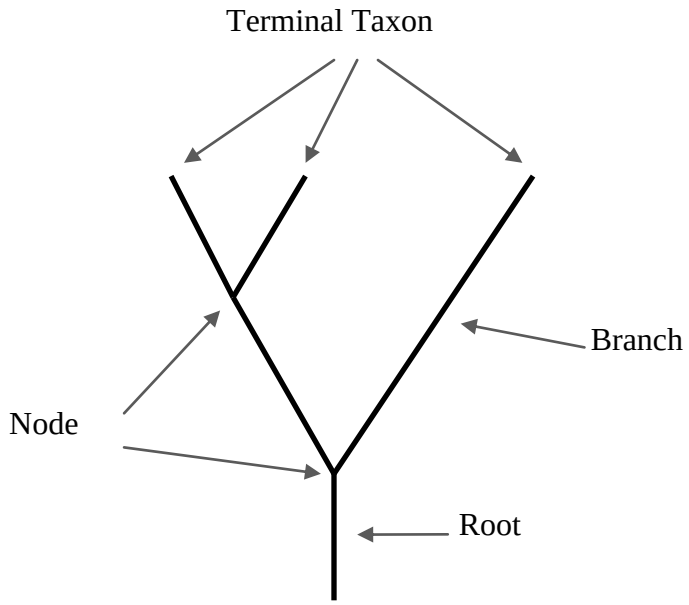

Figure C2: A simple example of a phylogenetic tree showing the major components.

REFERENCES

Aller, R. C.; Mackin, J. E.; Cox, R. T. Jr. Diagenesis of Fe and S in Amazon inner shelf muds: Apparent dominance of Fe reduction and implications for the genesis of ironstones. *Cont. Shelf. Res.* **1986**, *6*, 263-289.

Anderson, R. T.; Vrionis, H. A.; Ortiz-Bernad, I.; Resch, C. T.; Long, P. E.; Dayvault, R.; Karp, K.; Marutzky, S.; Metzler, D. R.; Peacock, A.; White, D. C.; Lowe, M.; Lovley, D. R. Stimulating the in situ activity of Geobacter species to remove uranium from the groundwater of a uranium-contaminated aquifer. *Appl. Environ. Microbiol.* **2003**, *69(10)*, 5884-5891.

Appenzeller, B. M. R.; Duval, Y. B.; Thomas, F.; Block, J. Influence of phosphate on bacterial adhesion onto iron oxyhydroxide in drinking water. *Environ. Sci. Tech.* **2002**, *36*, 646-652.

Arnold, R. G.; DiChristina, T. J.; Hoffman, M. R. Reductive dissolution of Fe(III) oxides by *Pseudomonas* sp. 200. *Biotechnol. Bioeng.* **1988**, *21*, 1081-1096.

Balashova, W.; Zavarzin, G. A. Anaerobic reduction of ferric iron by hydrogen bacteria. *Microbiol.* **1979**, *49(5)*, 635-639.

Beliaev, A. S.; Saffarini, D. A. *Shewanella putrefaciens mtrB* encodes an outer membrane protein required for Fe(III) and Mn(IV) reduction. *J. Bacteriol.* **1998**, *180(23)*, 6292-6297.

Bencharit, S.; Ward, M. J. Chemotactic responses to metals and anaerobic electron acceptors in *Shewanella oneidensis* MR-1. *J. Bacteriol.* **2005**, *187(14)*, 5049-5053.

Bonneville, S.; Van Cappellen, P.; Behrends, T. Microbial reduction of iron(III) oxyhydroxides: Effects of mineral solubility and availability. *Chem. Geol.* **2004**, *212(3-4)*, 255-268.

Bonneville, S.; Behrends, T.; Van Cappellen, P.; Hyacinthe, C.; Roling, W. F. M. Reduction of Fe(III) colloids by *Shewanella putrefaciens*: A kinetic model. *Geochim. Cosmochim. Acta.* **2006**, *70(23)*, 5842-5854.

Burns, J. L.; Ginn, B. R.; Bates, D. J.; Dublin, S. N.; Taylor, J. V.; Apkarian, R. P.; Amaro-garcia, S.; Neal, A. L.; DiChristina, T. J. Outer membrane-associated serine protease involved in adhesion of *Shewanella oneidensis* to Fe(III) oxides. *Environ. Sci. Technol.* **2010**, *44*, 68-73.

Caccavo, F.; Das, A. Adhesion of dissimilatory Fe(III)-reducing bacteria to Fe(III) minerals. *Geomicrobiol. J.* **2002**, *19(2)*, 161-177.

Caccavo, F.; Blakemore, R. P.; Lovley, D. R. A hydrogen-oxidizing, Fe(III)-reducing microorganism from the great bay estuary, New Hampshire. *Appl. Environ. Microbiol.* **1992**, *58(10)*, 3211-3216.

Caccavo, F.; Longergan, D. J.; Lovley, D. R.; Davis, M.; Stolz, J. F.; McInerney, M. J. *Geobacter sulfurreducens* sp. Nov., a hydrogen- and acetate- oxidizing dissimilatory metal-reducing microorganism. *Appl. Environ. Microbiol.* **1994**, *60(10)*, 3752-3759.

Caccavo, F.; Schamberger, P. C.; Keiding, K.; Nielsen, P. H. Role of hydrophobicity in adhesion of the dissimilatory Fe(III)-reducing bacterium *Shewanella alga* to amorphous Fe(III) oxide. *Appl. Environ. Microbiol.* **1997**, *63(10)*, 3837-3843.

Canfield, D. E.; Thamdrup, B.; Hansen, J. W. The anaerobic degradation of organic matter in Danish coastal sediments: Iron reduction, manganese reduction, and sulfate reduction. *Geochim. Cosmochim. Acta.* **1993**, *57*, 3867-3883.

von Canstein, H.; Ogawa, J.; Shimizu, S.; Lloyd, J. R. Secretion of flavins by *Shewanella* species and their role in extracellular electron transfer. *Environ. Microbiol.* **2008**, *74(3)*, 615-623.

Childers, S. E.; Ciufo, S. and Lovley, D. R. *Geobacter metallireducens* accesses insoluble Fe(III) oxide by chemotaxis. *Nature* **2002**, *416*, 767-769.

Coates, J. D.; Ellis, D. J.; Gaw, C. V.; Lovley, D. R. *Geothrix fermentans* gen. nov. sp. nov., an acetate-oxidizing Fe(III) reducer capable of growth via fermentation. *Int. J. Syst. Bacteriol.* **1999**, *49*, 1615-1622.

Coates, J. D.; Chakraborty, R.; O'Connor, S. M.; Schmidt, C.; Thieme, J. The geochemical effects of microbial humic substances reduction. *Acta. Hydroch. Hydrob.* **2001**, *28(7)*, 420-427.

Cummings, D. E.; Caccavo, F.; Fendorf, S.; Rosenzweig, R. F. Arsenic mobilization by dissimilaroty Fe(III)-reducing bacterium *Shewanella alga* BrY. *Environ. Sci. Technol.* **1999**, *33*, 723-729.

Das, A.; Caccavo, F. Jr. Addition of dissimilatory Fe(III)-reducing bacterium *Shewanella alga* BrY to crystalline Fe oxides. *Curr. Microbiol.* **2001**, *42*, 151-154.

DiChristina, T. J. Dissimilative Fe(III) reduction by *Alteromonas putrefaciens* strain 200. Ph.D. Dissertation, California Institute of Technology, Pasadena, CA, 1989.

DiChristina, T. J.; Moore, C. M.; Haller, C. A. Dissimilatory Fe(III) and Mn(IV) reduction by *Shewanella putrefaciens* requires *ferE*, a homolog of the *pulE* (*gspE*) type II protein secretion gene. *J. Bacteriol.* **2002**, *184(1)*, 142-151.

DiChristina, T. J.; Fredrickson, J. K.; Zachara, J. M. Enzymology of electron transport: Energy generation with geochemical consequences. *Rev. Mineral. Geochem.* **2005**, *59*, 27-52.

Fennessey, C. M.; Jones, M. E.; Taillefert, M.; DiChristina, T. J. Siderophores are not involved in Fe(III) solubilization during anaerobic Fe(III) respiration by *Shewanella oneidensis* MR-1. *Appl. Environ. Microbiol.* **2010**, *76(8)*, 2425-2432.

Francis, A. J.; Dodge, C. J. Anaerobic microbial remobilization of toxic metals corpecipitated with iron-oxide. *Environ. Sci. Technol.* **1990**, *24(3)*, 373-378.

Fredrickson, J. K.; Gorby, Y. A. Environmental processes mediated by iron-reducing bacteria. *Curr. Opin. Biotechnol.* **1996**, *7(3)*, 287-294.

Fredrickson, J. K.; Zachara, J. M.; Kennedy, D. W.; Kukkadapu, R. K.; McKinley, J. P.; Heald, S. M.; Liu, C.; Plymale, A. E. Reduction of TcO_4^- by sediment-associated biogenic Fe(II). *Geochim. Cosmochim. Acta*, **2004**, *68*, 3171-3178.

Fredrickson, J. K.; Zachara, J. M.; Plymale, A. E.; Heald, S. M.; McKinley, J. P.; Kennedy, D. W.; Liu, C.; Nachimuthu, P. Oxidative dissolution potential of biogenic and abiogenic TcO_2 in subsurface sediments. *Geochim. Cosmochim. Acta*, **2009**, *73*, 2299-2313.

Gorby, Y. A.; Lovley, D. R. Enzymatic uranium reduction. *Environ. Sci. Technol.* **1992**, *26*, 205-207.

Gorby, Y. A.; Yanina, S.; McLean, J. S.; Rosso, K. M.; Moyles, D.; Dohnalkova, A.; Beveridge, T. J.; Chang, I. S.; Kim, B. H.; Kim, K. S. and others. Electrically conductive bacterial nanowires produced by *Shewanella oneidensis* strain MR-1 and other microorganisms. *PNAS.* **2006**, *103(30)*, 11358-11363.

Gralnic, J. A.; Newman, D. K. Extracellular respiration. *Mol. Microbiol.* **2007**, *65(1)*, 1-11.

Grantham, M. C.; Dove, P. M. Investigation of bacterial-mineral interactions using fluid tapping mode(TM) atomic force microscopy. *Geochim. Cosmochim. Acta.* **1996**, *60(13)*, 2473-2480.

Grantham, M. C.; Dove, P. M.; DiChristina, T. J. Microbially catalyzed dissolution of iron and aluminum oxyhydroxide mineral surface coatings. *Geochim. Cosmochim. Acta.* **1997**, *61(21)*, 4467-4477.

Gupta, R. S. The phylogeny of *Proteobacteria*: Relationships to other eubacterial phyla and eukaryotes. *FEMS Microbiol. Rev*. **2000**, *24*, 367-402.

Harshey, R. M. Bacterial motility on a surface: Many ways to a common goal. *Annu. Rev. Microbiol.* **2003**, *57*, 249-273.

He, Q.; Sanford, R. A. Characterization of Fe(III) reduction by chlororespiring *Anaeromxyobacter dehalogenans*. *Appl. Environ. Microbiol.* **2003**, *69(5)*, 2712-2718.

Heijman, C. G.; Grieder, E.; Holliger, C.; Schwarzenback, R. O. Reduction of nitroaromatic-compounds coupled to microbial iron reduction in laboratory aquifer columns. *Environ. Sci. Technol.* **1995**, *29 (3)*, 775-783.

Hernandez, M. E.; Kappler, A.; Newman, D. K. Phenazines and other redox-active antibiotics promote microbial mineral reduction. *Appl. Environ. Microbiol.* **2004**, *70(2)*, 921-928.

Hyacinthe, C.; Bonneville, S.; Van Cappellen, P. Effect of sorbed Fe(II) on the reduction kinetics of 6-line ferrihydrite and amophous ferric phosphate by *Shewanella putrefaciens*. *Geomicrobiol. J.* **2008**, *25*, 181-192.

Jaisi, D. P.; Dong, H; Liu, C. Influence of biogenic Fe(II) on the extent of microbial

reduction of Fe(III) in clay minerals nontronite, illite, and chlorite. *Geochim. Cosmochim. Acta.* **2007**, *71(5)*, 1145-1158.

Jambor, J. L.; Dutrizac, J. E. Occurrence and constitution of natural and synthetic ferrihydrite, a widespread iron oxyhydroxide. *Chem. Rev.* **1998**, *98(7)*, 2549-2585.

Jiang, J.; Kappler, A. Kinetics of microbial and chemical reduction of humic substances: Implications for electron shuttling. *Environ. Sci. Technol.* **2008**, *42*, 3563-3569.

Johansen, J. E.; Pinhassi, J.; Blackburn, N.; Zweifel, U. L.; Hagstrom, A. Variability in motility characteristics among marine bacteria. *Aquat. Microb. Ecol.* **2002**, *28(3)*, 229-237.

Jones, M. E.; Fennessey, C. M.; DiChristina, T. J.; Taillefert, M. *Shewanella oneidensis* MR-1 mutants selected for their inability to produce soluble organic-Fe(III) complexes are unable to respire Fe(III) as anaerobic electron acceptor. *Environ. Microbiol.* **2010**, *12(4)*, 938-950.

Kappler, A.; Benz, M.; Schink, B.; Brune, A. Electron shuttling via humic acids in microbial iron(III) reduction in a freshwater sediment. *FEMS Microbiol. Ecol.* **2004**, *47(1)*, 85-92.

Kazumi, J.; Haggblom, M. M.; Young, L. Y. Degradation of monochlorinated and nonchlorinated aromatic compounds under iron-reducing conditions. *Appl. Environ. Microbiol.* **1995**, *61*, 4069-4073.

Kerisit, S.; Rosso, K. M. Computer simulation of electron transfer at hematite surfaces. *Geochim. Cosmochim. Acta.* **2006**, *70(8)*, 1888-1903.

Kerisit, S.; Rosso, K. M. Kinetic Monte Carlo model of charge transport in hematite (α-Fe2O3). *J. Chem. Phys.* **2007**, *127(12)*, 124706-1-124706-10.

Klausen, J.; Troeber, S. P.; Haderlein, S. B.; Schwarzenback, R. P. Reduction of substituted nitrobenzenes by Fe(II) in aqueous mineral suspensions. *Environ. Sci. Technol.* **1995**, *29*, 2396-2404.

Koretsky, C. M.; Haas, J. R.; Miller, D.; Ndenga, N. T. Seasonal variations in pore water and sediment geochemistry of littoral lake sediments (Asylum Lake, MI, USA).

Geochem. T. **2006**, *7(11)*.

Kostka, J. E.; Wu, J.; Nealson, K. H.; Stucki, J. W. The impact of structural Fe(III) reduction by bacteria on the surface chemistry of smectite clay minerals. *Geochim. Cosmochim. Acta.* **1999**, *63(22)*, 3705-3713.

Kostka, J. E.; Dalton, D. D.; Skelton, H.; Dollhopf, S.; Stucki, J. W. Growth of iron(III)-reducing bacteria on clay minerals as the sole electron acceptor and comparison of growth yields on a variety of oxidized iron forms. *Appl. Environ. Microbiol.* **2002**, *68(12)*, 6256-6262.

Lauga, E.; DiLuzio, W. R.; Whitesides, G. M.; Stone, H. A. Swimming in circles: Motion of bacteria near solid boundaries. *Biophys. J.* **2006**, *90(2)*, 400-412.

Liang, L.; McCarthy, J. F.; Jolley, L. W.; McNabb, A.; Mehlhorn, T. L. Iron dynamics: Transformation of Fe(II)/Fe(III) during injection of natural organic matter in a sandy aquifer. *Geochim. Cosmochim. Acta.* **1993**, 57, 1987-1999.

Liu, C.; Zachara, J. M.; Gorby, Y. A.; Szecsody, J. E.; Brown, C. F. Microbial reduction of Fe(III) and sorption/precipitation of Fe(II) on *Shewanella putrefaciens* stain CN32. *Environ. Sci. Technol.* **2001a**, *35*, 1385-1393.

Liu, C.; Kota, S.; Zachara, J. M.; Fredrickson, J. K.; Brinkman, C. K. Kinetic analysis of the bacterial reduction of goethite. *Environ. Sci. Technol.* **2001b**, *35*, 2482-2490.

Lloyd, J. R. Microbial reduction of metals and radionuclides. *FEMS Microbiol. Rev.* **2003**, *27*, 411-425.

Lloyd, J. R.; Sole, V. A.; Van Praagh, C. V. G.; Lovley, D. R. Direct and Fe(II)-mediated reduction of technetium by Fe(III)-reducing bacteria. *Appl. Environ. Microbiol.* **2000**, *66*, 3743-3749.

Lonergan, D. J.; Jenter, H. L.; Coates, J. D.; Phillips, E. J. P.; Schmidt, T. M.; Lovley, D. R. Phylogenetic analysis of dissimilatory Fe(III)-reducing bacteria. *J. Bacteriol.* **1996**, *178(8)*, 2402-2408.

Lovley, D. R. Dissimilatory Fe(III) and Mn(IV) reduction. *Microbiol. Rev.* **1991**, *55(2)*, 259-287.

Lovley, D. R.; Lonergan, D. J. Anaerobic oxidtion of toluene, phenol, and p-cresol by the dissimilatory iron-reducing organism, GS-15. *Appl. Environ. Microbiol*. **1990**, *56*, 1858-1864.

Lovley, D. R.; Phillips, E. J. P. Novel mode of microbial energy metabolism: Organic carbon oxidation coupled to dissimilatory reduction of iron and manganese. *Appl. Environ. Microbiol.* **1988**, *54(6)*, 1472-1480.

Lovley, D. R.; Phillips, E. J. P. Bioremediation of uranium contamination with enzymatic uranium reduction. *Environ. Sci. Technol.* **1992**, *26*, 2228-2234.

Lovley, D. R.; Woodward, J. C. Mechanisms for chelator stimulation of microbial Fe(III)-oxide reduction. *Chem. Geol.* **1996**, *132(1-4)*, 19-24.

Lovley, D. R.; Baedecker, M. J.; Lonergan, D. J.; Cozzarelli, I. M.; Phillips, E. J. P.; Siegel, D. I. Oxidation of aromatic contaminants coupled to microbial iron reduction. *Nature* **1989**, *339*, 297-299.

Lovley, D. R.; Phillips, E. J. P.; Gorby, Y. A.; Landa, E. R. Microbial reduction of uranium. *Nature* **1991a**, *350*, 413-416.

Lovley, D. R; Phillips, E. J. P.; Lonergan, D. J. Enzymatic versus nonenzymatic mechanisms for Fe(III) reduction in aquatic sediments. *Environ. Sci. Tech.* **1991b**, *25*, 1062-1067.

Lovley, D. R.; Woodward, J. C.; Chapelle, F. H. Stimulated anoxic biodegradation of aromatic hydrocarbons using Fe(III) ligands. *Nature* **1994**, *370*, 128-131.

Lovley, D. R.; Coates, J. D.; Blunt-Harris, E. L.; Phillips, E. J. P.; Woodward, J. C. Humic substances as electron acceptors for microbial respiration. *Nature* **1996**, *382*, 445-448.

Lower, S. K.; Tadanier, C. J.; Hochella, M. F. Measuring interfacial adhesion forces between bacteria and mineral surfaces with biological force microscopy. *Geochim. Cosmochim. Acta.* **2000**, *64(18)*, 3133-3139.

Luria, S. E.; Burrous, J. W. Hybridization between *Escherichia coli* and Shigella. *J. Bacteriol.* **1957**, *74*, 461-476.

Luther, G. W.; Kostka, J. E.; Church, T. M.; Sulzberger, B.; Stumm, W. Seasonal iron cycling in the salt-marsh sedimentary environment: The importance of ligand complexes with Fe(II) and Fe(III) in the dissolution of Fe(III) minerals and pyrite, respectively. *Mar. Chem.* **1992**, *40*, 81-103.

Maddison, D. R., Schulz, K. S., Eds. The Tree of Life Web Project; http://tolweb.org.

Marsili, E.; Baron, D. B.; Shikhare, I. D.; Coursolle, D.; Gralnick, J. A.; Bond, D. R. *Shewanella* secretes flavins that mediate extracellular electron transfer. *PNAS* **2008**, *105(10)*, 3968-3973.

Micic, M.; Hu, D.; Suh, Y. D.; Newton, G.; Romine, M.; Lu, P. H. Correlated atomic force microscopy and fluorescence lifetime imaging of live bacterial cells. *Colloid Surf., B* **2003**, *34*, 205-212.

Murad, E.; Rojik, P. Jarosite, schwertmannite, goethite, ferrihydrite and lepidocrocite: The legacy of coal and sulfide ore mining. 3rd Australian New Zealand Soils Conference, University of Sydney, NSW, Australia, 2004.

Myers, C. R.; Myers, J. M. Localization of cytochromes to the outer membrane of anaerobically grown *Shewanella putrefaciens* MR-1. *J. Bacteriol.* **1992**, *174(11)*, 3429-3438.

Myers, C. R.; Myers, J. M. Cloning and sequence of *cymA* a gene encoding a tetraheme cytochrome c required for reduction of iron(III), fumarate, and nitrate by *Shewanella putrefaciens* MR-1. *J. Bacteriol.* **1997**, *179*, 1143-1152.

Myers, J. M.; Myers, C. R. Role of the tetraheme cytochrome CymA in anaerobic electron transport in cells of *Shewanella putrefaciens* MR-1 with normal levels of menaquinone. *J. Bacteriol.* **2000**, *182*, 67-75.

Myers, C. R.; Myers, J. M. Cell surface exposure of the outer membrane cytochromes of *Shewanella oneidensis* MR-1. *Lett. Appl. Microbiol.* **2003**, *37(3)*, 254-258.

Myers, C. R.; Nealson, K. H. Bacterial manganese reduction and growth with manganese oxide as the sole electron-acceptor. *Science* **1988**, *240(4857)*, 1319-1321.

Neal, A. L.; Rosso, K. M.; Geesey, G. G.; Gorby, Y. A.; Little, B. J. Surface structure effects on direct reduction of iron oxides by *Shewanella oneidensis*. *Geochim.*

Cosmochim. Acta. **2003**, *67(23)*, 4489-4503.

Nealson, K. H.; Berelson, W. Layered microbial communities and the search for life in the universe. *Geomicrobiol. J.* **2003**, *20*, 451-462.

Nealson, K. H.; Little, B. Breathing manganese and iron: Solid-state respiration. *Adv. Appl. Microbiol.* **1997**, *45*, 213-239.

Nealson, K. H.; Saffarini, D. Iron and Manganese in anaerobic respiration: Environmental significance, physiology and regulation. *Annu. Rev. Microbiol.* **1994**, *48*, 311-343.

Nealson, K. H.; Stahl, D. A. Microorganisms and biogeochemical cycles: What can we learn from layered microbial communities? *Rev. Mineral.* **1997**, *35*, 5-34.

Nevin, K. P.; Lovley, D. R. Lack of production of electron-shuttling compounds or solubilization of Fe(III) during reduction of insoluble Fe(III) oxide by *Geobacter metallireducens*. *Appl. Environ. Microbiol.* **2000**, *66(5)*, 2248-2251.

Nevin, K. P.; Lovley, D. R. Mechanisms for accessing insoluble Fe(III) oxide during dissimilatory Fe(III) reduction by *Geothrix fermentans*. *Appl. Environ. Microbiol.* **2002a**, *68(5)*, 2294-2299.

Nevin, K. P.; Lovley, D. R. Mechanisms for Fe(III) oxide reduction in sedimentary environments. *Geomicrobiol. J.* **2002b**, *19*, 141-159.

Newman, D. K.; Kolter, R. A role for excreted quinones in extracellular electron transfer. *Nature* **2000**, *405(6782)*, 94-97.

Obuekwe, C. O.; Westlake, D. W. S.; Cook, F. D.; Costerton, J. W. Surface changes in mild steel coupons from the action of corrosion-causing bacteria. *Appl. Environ. Microbiol.* **1981**, *41(3)*, 766-774.

Payne, A.; DiChristina, T. J. A rapid mutant screening technique for detection of technetium [Tc(VII)] reduction-deficient mutants of *Shewanella oneidensis* MR-1. *FEMS Microbiol. Lett.* **2006**, *259*, 282-287.

Peretyazhko, T. S.; Zachara, J. M.; Kennedy, D. W.; Fredrickson, J. K.; Arey, B. W.; McKinley, J. P.; Wang, C. M.; Dohnalkova, A. C.; Xia, Y. Ferrous phosphate surface precipitates resulting from the reduction of intragrain 6-line ferrihydrite by *Shewanella oneidensis* MR-1. *Geochim. Cosmochim. Acta.* **2010**, *74*, 3751-3767.

Petrovskis, E. A.; Vogel, Te. M.; Adriaens, P. Effects of electron accepters and donors on transformation of tetrachloromethane by *Shewanella-putrefaciens* MR-1. *FEMS Microbiol. Lett.* **1994**, *121(3)*, 357-363.

Pitts, K. E.; Dobbin, P. S.; Reyes-Ramirez, F.; Thomson, A. J.; Richardson, D. J.; Seward, H. E. Characterization of the *Shewanella oneidensis* MR-1 decaheme cytochrome MtrA. *J. Biol. Chem.* **2003**, *278(30)*, 27758-27765.

Pugsley, A. P. The complete general secretory pathway in gram-negative bacteria. *Microbiol. Rev.* **1993**, *57*, 50-108.

Reeburgh, W. S. Rates of biogeochemical processes in anoxic sediments. *Ann. Rev. Earth Planet. Sci.* **1983**, *11*, 269-298.

Reguera, G.; McCarthy, K. D.; Mehta, T.; Nicoll, J. S.; Tuominen, M. T.; Lovley, D. R. Extracellular electron transfer via microbial nanowires. *Nature* **2005**, *435(7045)*, 1098-1101.

Roden, E. E. Fe(III) oxide reactivity toward biological versus chemical reduction. *Environ. Sci. Technol.* **2003**, *37(7)*, 1319-1324.

Roden, E. E. Analysis of long-term bacterial vs. chemical Fe(III) oxide reduction kinetics. *Geochim. Cosmochim. Acta.* **2004**, *68(15)*, 3205-3216.

Roden, E. E. Geochemical and microbiological controls on dissimilatory iron reduction. *C. R. Geosci.* **2006**, *338*, 456-467.

Roden, E. E.; Lovley, D. R. Dissimilatory Fe(III) reduction by the marine microorganism *Desulfuromonas acetoxidans*. *Appl. Environ. Microbiol.* **1993**, *59(3)*, 734-742.

Roden, E. E.; Wetzel, R. G. Kinetics of microbial Fe(III) oxide reduction in freshwater wetland sediments. *Limnol. Oceanogr.* **2002**, *47(1)*, 198-211.

Roden, E. E.; Zachara, J. M. Microbial reduction of crystalline iron(III) oxides: Influence of oxide surface area and potential for cell growth. *Environ. Sci. Technol.* **1996**, *30(5)*, 1618-1628.

Rosso, K. M.; Zachara, J. M.; Fredrickson, J. K.; Gorby, Y. A.; Smith, S. C. Nonlocal bacterial electron transfer to hematite surfaces. *Geochim. Cosmochim. Acta.* **2003a**, *67(5)*, 1081-1087.

Rosso, K.M.; Smith, D. M. A.; Dupuis, M. An ab initio model of electron transport in hematite (α-Fe2O3) basal planes. *J. Chem. Phys.* **2003b**, *118(14)*, 6455-6466.

Royer, R. A.; Burgos, W. D.; Fisher, A. S.; Jeon, B.; Unz, R. F.; Dempsey, B. A. Enhancement of hematite bioreduction by natural organic matter. *Environ. Sci. Technol.* **2002**, *36*, 2897-2904.

Royer, R. A.; Dempsey, B. A.; Jeon, B.; Burgos, W. D. Inhibition of biological reductive dissolution of hematite by ferrous iron. *Environ. Sci. Technol.* **2004**, *38*, 187-193.

Rusin, P. A.; Quintana, L.; Brainard, J. R.; Strietelmeier, B. A.; Tait, C. D.; Ekberg, S. A.; Palmer, P. D.; Newton, T. W.; Clark, D. L. Solubilization of plutonium hydrous oxide by iron-reducing bacteria. *Environ. Sci. Technol.* **1994**, *28*, 1686-1690.

Schwertmann, U.; Cornell, R.M. *Iron Oxides in the Laboratory: Preparation and Characterization*; Wiley-VCH: Verlag GmbH, Weinheim, Germany, 2000.

Semple, K.; Westlake, D. W. S. Characterization of iron-reducing *Alteromonas-putrefaciens* strains from oil field fluids. *Can. J. Microbiol.* **1987**, *33(5)*, 366-371.

Shi, L; Squier, T. C.; Zachara, J. M.; Fredrickson, J. K. Respiration of metal (hydr)oxides by *Shewanella* and *Geobacter*: A key role for multihaem c-type cytochromes. *Mol. Microbiol.* **2007**, *65(1)*, 12-20.

Shi, L.; Deng, S.; Marshal, M. J.; Wang, Z.; Kennedy, D. W.; Dohnalkova, A. C.; Mottaz, H. M.; Hill, E. A.; Gorby, Y. A.; Beliaev, A. S.; Richardson, D. J.; Zachara, J. M.; Fredrickson, J. K. Direct involvement of type II secretion system in extracellular translocation of *Shewanella oneidensis* outer membrane cytochromes MtrC and OmcA. *J. Bacteriol.* **2008**, *190(15)*, 5512-5516.

Stack, A. G.; Eggleston, C. M.; Engelhard, M. H. Reaction of hydroquinone with hematite I. Study of adsorption by electrochemical-scanning tunneling microscopy and X-ray photoelectron spectroscopy. *J. Colloid Interf. Sci.* **2004a**, *274(2)*, 433-441.

Stack, A. G.; Rosso, K. M.; Smith, D. M. A.; Eggleston, C. M. Reaction of hydroquinone with hematite II. Calculated electron-transfer rates and comparison to the reductive dissolution rate. *J. Colloid Interf. Sci.* **2004b**, *274(2)*, 442-450.

Stackebrandt, E.; Murray, R. G. E.; Truper, H. G. *Proteobacteria* classis nov., a name for the phylogenetic taxon that includes the "purple bacteria and their relatives". *Int. J. Syst. Bacteriol.* **1988**, *38(3)*, 321-325.

Stookey, L. L. Ferrozine - A new spectrophotometric reagent for iron. *Anal. Chem.* **1970**, *42(7)*, 779-781.

Suter, D.; Banwart, S.; Stumm, W. Dissolution of hydrous iron(III) oxides by reductive mechanisms. *Langmuir.* **1991**, *7(4)*, 809-813.

Taillefert, M.; Beckler, J. S.; Carey, E.; Burns, J. L.; Fennessey, C. M.; DiChristina, T. J. *Shewanella putrefaciens* produces an Fe(III)-solubilizing organic ligand during anaerobic respiration on insoluble Fe(III) oxides. *J. Inorg. Biochem.* **2007**, *101*, 1760-1767.

Thormann, K. M.; Saville, R. M.; Shukla, S.; Pelletier, D. A.; Spormann, A. M. Initial phases of biofilm formation in *Shewanella oneidensis* MR-1. *J. Bacteriol.* **2004**, *186(23)*, 8096-8104.

Turick, C. E.; Tisa, L. S.; Caccavo, F. Melanin production and use as a soluble electron shuttle for Fe(III) oxide reduction and as a terminal electron acceptor by *Shewanella algae* BrY. *Appl. Environ. Microbiol.* **2002**, *68(5)*, 2436-2444.

Urrutia, M. M.; Roden, E. E.; Fredrickson, J. K.; Zachara, J. M. Microbial and surface chemistry controls on reduction of synthetic Fe(III) oxide minerals by the dissimilatory iron-reducing bacterium *Shewanella alga*. *Geomicrobiol. J.* **1998**, *15(4)*, 269-291.

Venkateswaran, K.; Moser, D. P.; Dollhopf, M. E.; Lies, D. P.; Saffarini, D. A.; MacGregor, B. J.; Ringelberg, D. B.; White, D. C.; Nishijima, M.; Sano, H.; Burghardt, J.; Stackebrandt, E.; Nealson, K. H. Polyphasic taxonomy of the genus

Shewanella and description of *Shewanella oneidensis* sp. nov. *Int. J. Syst. Bacteriol.* **1999**, *49*, 705-724.

Viamajala, S.; Peyton, B. M.; Apel, W. A.; Petersen, J. M. Chromate/Nitrate interactions in *Shewanella oneidensis* MR-1: Evidence for multiple hexavalent chromium [Cr(VI)] reduction mechanisms dependent on physiological growth conditions. *Biotechnol. Bioeng*. **2002**, *78(7)*, 770-778.

Wade, R.; DiChristina, T. J. Isolation of U(VI) reduction-deficient mutants of *Shewanella putrefaciens*. *FEMS Microbiol. Lett.* **2000**, *184*, 143-148.

Winkler, R. L.; Hays, W. L. *Statistics: probability, inference, and decision*; Holt, Rinehart, and Winston: New York, 1975.

Woese, C. R. Bacterial Evolution. *Microbiol. Rev.* **1987**, *51(2)*, 221-271.

Xu, Y.; Schoonen, A. A. The absolute energy positions of conduction and valence bands of selected semiconducting materials. *Am. Mineral.* **2000**, *85*, 543-556.

Zachara, J. M.; Fredrickson, J. K.; Li, S.; Kennedy, D. W.; Smith, S. C.; Gassman, P. L. Bacterial reduction of crystalline Fe^{3+} oxides in single phase suspensions and subsurface materials. *Am. Mineral.* **1998**, *83(11-12)*, 1426-1443.

Zinder, B.; Furrer, G.; Stumm, W. The coordination chemistry of weathering .2. dissolution of Fe(III) oxides. *Geochim. Cosmochim. Acta.* **1986**, 5*0(9)*, 1861-1869.

Zhang, M.; Dale, J. R.; DiChristina, T. J.; Stack, A. G. Dissolution morphology of iron (oxy)(hydr)oxides exposed to the dissimilatory iron-reducing bacterium *Shewanella oneidensis* MR-1. *Geomicrobiol. J.* **2009**, *26*, 83-92.